RESTING-STATE VERSUS BREATH-HOLD FOR TESTING FUNCTIONAL MAGNETIC RESONANCE IMAGING INTEGRITY IN PRE-SURGICAL PLANNING

by

Nooshin Jafari Fesharaki

A Dissertation Submitted in

Partial Fulfillment of the

Requirements for the Degree of

Doctor of Philosophy

in Health Sciences

at

The University of Wisconsin-Milwaukee

August 2021

ABSTRACT

RESTING-STATE VERSUS BREATH-HOLD FOR TESTING FUNCTIONAL MAGNETIC RESONANCE IMAGING INTEGRITY IN PRE-SURGICAL PLANNING

by

Nooshin Jafari Fesharaki

The University of Wisconsin-Milwaukee, 2021
Under the Supervision of Professor Wendy Huddleston

The neuro-vascular coupling mechanism responsible for blood oxygenation level dependent (BOLD) functional magnetic resonance imaging (fMRI) signals can be focally disrupted by various pathological factors (such as brain tumors) while leaving the underlying neurons functionally intact. Such neuro-vascular uncoupling (NVU) can pose serious complications for clinical use of fMRI. Mapping of cerebrovascular reactivity (CVR), which is a measure of the dilatory function of cerebral vasculature, can be a useful approach for detecting potential NVU. The widely-accepted approach for non-invasive CVR mapping requires the patient to perform a breath-hold challenge, which may have practical disadvantages for many patient populations. Thus, a clinical need for CVR mapping with fewer (if no) practical limitations could benefit surgeon's decision-making. Resting-state fMRI has great potential to fill this need. To assess the feasibility for the use of resting-state CVR maps as an alternative to breath-hold CVR maps for identifying regions of likely NVU, we investigated their three normative characteristics at a voxel level of resolution: (1) quality of spatial labeling of the critical brain areas, (2) continuity and uniformity, and (3) validity for clinical use. In all three

phases of this study, we first thresholded the CVR maps by optimizing coverage of gray matter while minimizing false responses in white matter. When so optimized, the resting-state vs. breath-hold CVR maps had moderately better gray matter coverage and specificity but our ability to statistically specify a hole as a site of potential NVU was comparable across approaches. We also assessed the voxel-wise spatial correspondence between the two maps across a wide range of thresholds. Optimal spatial correspondence was strongly dependent on threshold settings, which if improperly set, tended to produce statistically biased maps. While the two CVR maps were not quantitatively identical at a voxel level of resolution when optimized, they did consistently have moderately good correspondence with each other. To test the validity of our approach, we retrospectively evaluated the resting-state CVR maps of a cohort of 13 patients with brain tumors and assessed how reliably these maps would reveal foci of potential NVU in pre-surgical task-fMRI activation maps. The impaired resting-state CVR maps spatially corresponded to NVU-induced impairment of task-fMRI activation patterns in four patients with suspected NVU. While NVU-related false negatives on task-based fMRI activation maps were characterized with holes in resting-state CVR maps, our results also provided evidence that tumor-induced NVU could occur with no apparent effects on vasoreactivity in one patient.

From the standpoint of clinical utility, the use of resting-state CVR maps with significantly more specific labeling of critical brain areas may provide a comparative advantage over the breath-hold CVR maps for testing the integrity of task-fMRI activation. A statistically comparable degree of sensitivity between the two CVR maps in detecting potential NVU may also offer the use of resting-state approach due to its advantages such as the ease of use and computation. In sum, our results take a step towards using the resting-state-based CVR mapping as an imaging marker in the clinical setting to identify fMRI signal dropouts caused likely by

NVU, for which the clinicians should be warned to take extra care when interpreting the fMRI brain maps, particularly in surgical scenarios.

To

my wonderful parents for all their love, patience, and support,

and Behrooz, who always encouraged me to go on every adventure, especially this one.

TABLE OF CONTENTS

LIST OF FIGURES

LIST OF TABLES

LIST OF ABBREVIATIONS

ACC	**Accuracy**
ALFF	**Amplitude of Low Frequency Fluctuations**
BOLD	**Blood Oxygenation Level Dependent**
CBF	**Cerebral Blood Flow**
CBV	**Cerebral Blood Volume**
CO_2	**Carbone Dioxide**
CVR	**Cerebrovascular Reactivity**
fMRI	**Functional Magnetic Resonance Imaging**
GM-VOI	**Gray Matter Volume of Interest**
GMW-VOI	**Gray and White Matter Volume of Interest**
FN	**False Negative**
FP	**False Positive**
GBM	**Glioblastoma Multiforme**
NVU	**Neuro-vascular Uncoupling**
ROI	**Region of Interest**
RRF	**Respiratory Response Function**
SS	**Spatial Similarity**
TE	**Echo Time**
TN	**True Negative**
TP	**True Positive**
TR	**Repetition Time**
VOI	**Volume of Interest**

ACKNOWLEDGEMENTS

First and foremost, I would like to express my deepest appreciation to my advisors, Dr. **Edgar DeYoe**, and Dr. **Wendy Huddleston** for their invaluable advice, continued support, and patience during the course of my PhD degree. Their immense knowledge and plentiful experience have encouraged me in all the time of my academic research and daily life. I am extremely grateful for their consistent guidance, insightful feedback, and constructive criticism that have always pushed me to sharpen my thinking and brought my work to a higher level. Additionally, I would like to express my sincere thanks to my thesis committee, Dr. **Adam Greenberg**, Dr. **Brooke Slavens**, and Dr. **Christine Larson** for their mentorship throughout the entire duration of this study. I also very much appreciate Dr. **David Gutterman** for acknowledging my interests in the field of Neuroimaging and for his support which was really influential in shaping my doctoral journey. Thanks should also go to my friends, lab mates, colleagues, and research team in the Center for Imaging Research at the **Medical College of Wisconsin** for a cherished time spent together in the lab. Particularly helpful to me during this time were **Doug Ward** and **Jed Mathis**, who always supported me by offering practical suggestions for dealing with methodological and technical problems. Finally, my appreciation goes out to my family and friends for their tremendous encouragement and support in all these years.

I. Introduction

Background

According to the Central Brain Tumor Registry of the United States (CBTRUS), the incidence rate for primary brain and other nervous system tumors in the United States is 23.79 cases per 100,000 people (Ostrom et al., 2020). The CBTRUS projects that in 2021 alone, 84,170 patients will be diagnosed with one of these tumors, including 25,130 cases of malignant tumors (Ostrom et al., 2020). The average five-year survival rate for people diagnosed with primary malignant brain tumors from 2001 to 2016 was only 36% (Ostrom et al., 2020). While the prognosis for such diseases is poor, particularly for the most malignant types, e.g., glioblastoma multiforme (GBM), aggressive surgery and/or radiation therapy can bring new hope to patients, both in terms of survival and quality of life (Siegel, Miller, & Jemal, 2019; A. S. Zhang et al., 2017). Given that there is an association between increased survival time and the extent to which a tumor is removed (Sanai, Polley, McDermott, Parsa, & Berger, 2011), the desired goal of these treatments is to either resect or destroy as much of the brain tumor as possible. However, there may not always be a clear-cut distinction between grossly abnormal brain tissue and the surrounding healthy tissue, meaning that such aggressive therapies may inadvertently injure nearby healthy brain tissue thereby leading to post-treatment deficits such as loss of sensory processing, loss of linguistic ability, or paralysis. Treating brain tumors becomes a trade-off where curative therapies come at the risk of compromising a patient's neurological function.

Fortunately, the use of task-based blood oxygenation level-dependent (BOLD) functional magnetic resonance imaging (fMRI) for presurgical brain mapping allows for a safer, more

effective surgery by identifying eloquent brain tissue, critical functional brain areas that surround a site of operable pathology, which might be at risk for surgical-induced damage (Baig, Klein, & Mechtler, 2016; Barone, Lawrie, & Hart, 2014; Hart, Rao, & Nuwer, 2007; Jenkinson et al., 2018; Pillai, 2010). In this technique, successive functional images are acquired when the subject is exposed to sensory stimuli or performs a task during the MRI (Silva, See, Essayed, Golby, & Tie, 2018). BOLD fMRI signals arise from changes in the relative ratio of blood oxygenated to deoxygenated hemoglobin within imaging voxels as a result of local hemodynamic responses, i.e. local changes in cerebral blood flow (CBF), cerebral blood volume (CBV), and metabolic rate of oxygen, to stimulus- or task-based changes in neural activity (Kwong et al., 1992; S. Ogawa, T. M. Lee, A. R. Kay, & D. W. Tank, 1990). This process involves a complex cascade of cellular and chemical events linking local changes in neural activity to nearby microvascular responses (a.k.a. neuro-vascular coupling cascade), which ultimately mediate the level of blood oxygenation and give rise to a localized BOLD response (Attwell et al., 2010; Catherine N. Hall, Howarth, Kurth-Nelson, & Mishra, 2016; C. N. Hall et al., 2014; Hillman, 2014; Nippert, Biesecker, & Newman, 2018).

The exact mechanism underlying the so-called neuro-vascular coupling is still not fully understood; however, two main signaling pathways have been recognized in the literature, as outlined in Figure 1.1 (Attwell et al., 2010; Catherine N. Hall et al., 2016; Hillman, 2014; Nippert et al., 2018). In summary, glutamatergic synaptic activity activates post-synaptic neurons via NMDA (N-methyl-D-aspartate) receptors, yet also acts on astrocytic glia via metabotropic glutamate receptors (mGluR), thereby increasing the rate of intracellular calcium (Ca^{+2}) (Attwell et al., 2010; Zonta et al., 2003). These two parallel signaling pathways affect arteriole and precapillary smooth muscle cells via local chemical mediators, such as nitric oxide (NO),

arachidonic acid (AA), prostaglandins (PG), potassium (K^+), and some peptides (Attwell et al., 2010; Cauli et al., 2004; Girouard & Iadecola, 2006; Catherine N. Hall et al., 2016; Nippert et al., 2018). While more research is needed to confirm the details of these two signaling pathways, it has been suggested that other neural and vascular cells may also be involved in the neuro-vascular coupling mechanism. Recent findings have attributed inhibitory γ-Aminobutyric acid (GABA) interneurons, capillary pericytes, and endothelial cells to neuronally-induced regulation of CBF; however, the exact role of these cells is still under debate (Biesecker et al., 2016; B. R. Chen, Kozberg, Bouchard, Shaik, & Hillman, 2014; Gould, Tsai, Kleinfeld, & Linninger, 2017; Guerra et al., 2018; Catherine N. Hall et al., 2016; C. N. Hall et al., 2014; Hamilton, Attwell, & Hall, 2010; Huneau, Benali, & Chabriat, 2015; Kisler et al., 2017; Nippert et al., 2018).

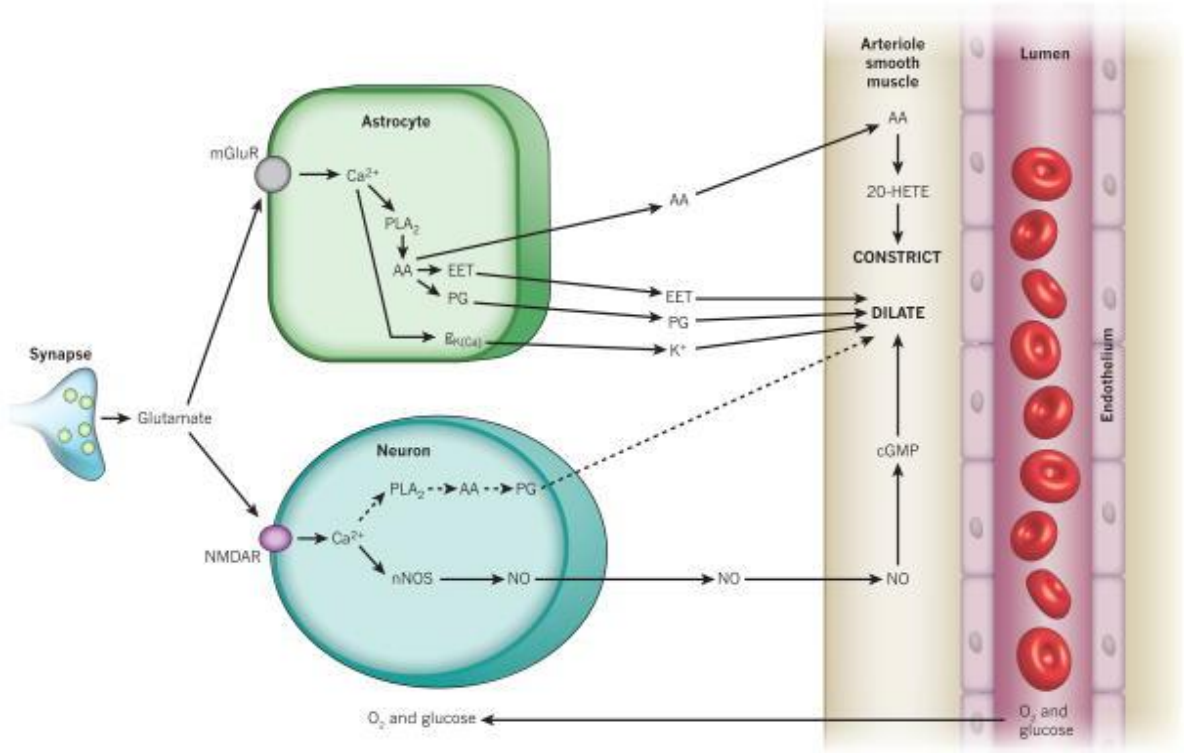

Figure 1.1. Two main signaling pathways that facilitate the neuro-vascular coupling (Attwell et al., 2010)

Despite the uncertainty of the exact details of the neuro-vascular coupling mechanism, there has been a growing interest in clinical use of the task-based BOLD fMRI technique over the last few years. The effectiveness of this technique for presurgical planning has been demonstrated on patients with epilepsy and tumors (Kumar et al., 2020; Szaflarski et al., 2017; Vakamudi, Posse, Jung, Cushnyr, & Chohan, 2020). Its equivalence or superiority compared with other standardized brain-mapping techniques, together with the technical advances in data acquisition, processing, and delivery, in addition to the development of many paradigms for visual, motor, and language mapping, have led to its widespread adoption in neurosurgical planning (DeYoe, Ulmer, Mathis, & Mueller, 2014; Janecek et al., 2013; Silva et al., 2018). In fact, to date, presurgical brain mapping has been the only clinical application of BOLD fMRI for which there are approved current-procedural terminology (CPT) codes (Hart et al., 2007). This technique also offers unique features such as its non-invasive nature, high spatial resolution, whole brain imaging, relative affordability, and extensive availability (Glover, 2011; Orringer, Vago, & Golby, 2012).

In presurgical brain mapping, using the task-based BOLD fMRI technique has been premised on the assumption that if a brain region is functionally intact, the onset of neural activity by performing a task or exposing to a stimulus should lead to a hemodynamic response, which can be detected by an MRI scanner. In this setting, localized BOLD fMRI "activation" indicates functional specificity and, potentially, serves as a biomarker of intact brain tissue. Subsequently, a lack of fMRI response near or within a site of operable pathology can be interpreted as a non-functional region that is, therefore, safe for resection and/or radiation (Silva et al., 2018).

The efficacy of fMRI for presurgical planning depends on its ability to reliably distinguish between abnormal (non-functional) brain tissue and healthy tissue; however, several clinical studies have shown that in the setting of focal brain pathologies (e.g. tumors), BOLD fMRI

activation can be compromised within functional regions (Duarte et al., 2015; Holodny et al., 2000; Hou et al., 2006 2006; Mazerolle, Ma, Sinclair, & Pike, 2018; Para et al., 2017; Pillai & Mikulis, 2014; Pineiro, Pendlebury, Johansen-Berg, & Matthews, 2002; Silva et al., 2018; Ulmer, Hacein-Bey, et al., 2004; Zaca, Jovicich, Nadar, Voyvodic, & Pillai, 2014). When underlying neurons are still functionally viable, the compromised BOLD signals presenting as false negatives (or dropouts) on brain activation maps could be related to a phenomenon known as *neuro-vascular uncoupling* (NVU). NVU refers to a situation wherein a focal type of brain pathology selectively disrupts the coupling between neurons and cerebral vasculature, thereby resulting in a locally impaired hemodynamic response to intact neuronal activity (DeYoe & Ulmer, 2005; Pillai & Zaca, 2011; Ulmer, Hacein-Bey, et al., 2004; Ulmer et al., 2003). Potential NVU in the setting of focal brain pathology can undermine the use of fMRI for presurgical planning. This is because if NVU is undetected, impaired fMRI activation can be interpreted as a non-functional region that is safe for resection or radiation, which may then cause new permanent neurological deficits (e.g., paralysis) for patients (McGirt et al., 2009; Rahman et al., 2016). Therefore, with an emphasis on the avoidance of false negatives (type II errors) in surgical interventions, a successful, reliable integration of BOLD fMRI technique into clinical practices still requires the detection of NVU for an accurate interpretation of brain activation maps.

Over the last decade, evidence has gradually been accumulated that brain-wide maps of vascular response to a vasoactive agent such as carbon dioxide (CO_2), known as cerebrovascular reactivity (CVR) maps, can potentially test the integrity of fMRI activation for potential NVU (S. Agarwal, Airan, Gujar, Sair, & Pillai, 2015; Mikulis, 2013; Pak et al., 2017; Peacock, Black, DeLone, & Welker, 2016; Pillai & Mikulis, 2014; C. H. B. van Niftrik et al., 2019; Zaca, Hua, & Pillai, 2011; Zaca et al., 2014; Zaca & Pillai, 2012). In this context, CVR "activation" (a term

borrowed from the conventional task-based BOLD fMRI) serves as an imaging marker for healthy vascular reactivity; a brain area with impaired CVR can therefore be identified as a site of potential NVU (S. Agarwal, Lu, & Pillai, 2017; Mikulis, 2013; Pillai & Mikulis, 2014; Zaca et al., 2014). In cases where a critical brain region has displayed impaired vascular responses, testing the behavioral relevance of fMRI activation maps can then verify the unresponsive area as a site of NVU (DeYoe & Raut, 2014; DeYoe & Ulmer, 2005; DeYoe et al., 2015).

CVR mapping is typically accomplished through brain-wide manipulation of the blood CO_2 level by a hypercapnic maneuver such as inhaling air with an increased CO_2 content during BOLD fMRI brain mapping (Lythgoe, Williams, Cullinane, & Markus, 1999). The use of CO_2 in fMRI-based CVR mapping is due to the unique features that this gas offers in terms of its practicality of use and sensitivity (Thomas, Liu, Park, van Osch, & Lu, 2014b). The gas CO_2 is an intrinsic agent of the human body with little toxicity that is rapidly eliminated through the lungs. More notably, this gas is a potent vasodilator that affects the contractile state of the smooth muscle cells located on arterioles and precapillaries (Attwell, Buchan et al. 2010, Chen 2018).

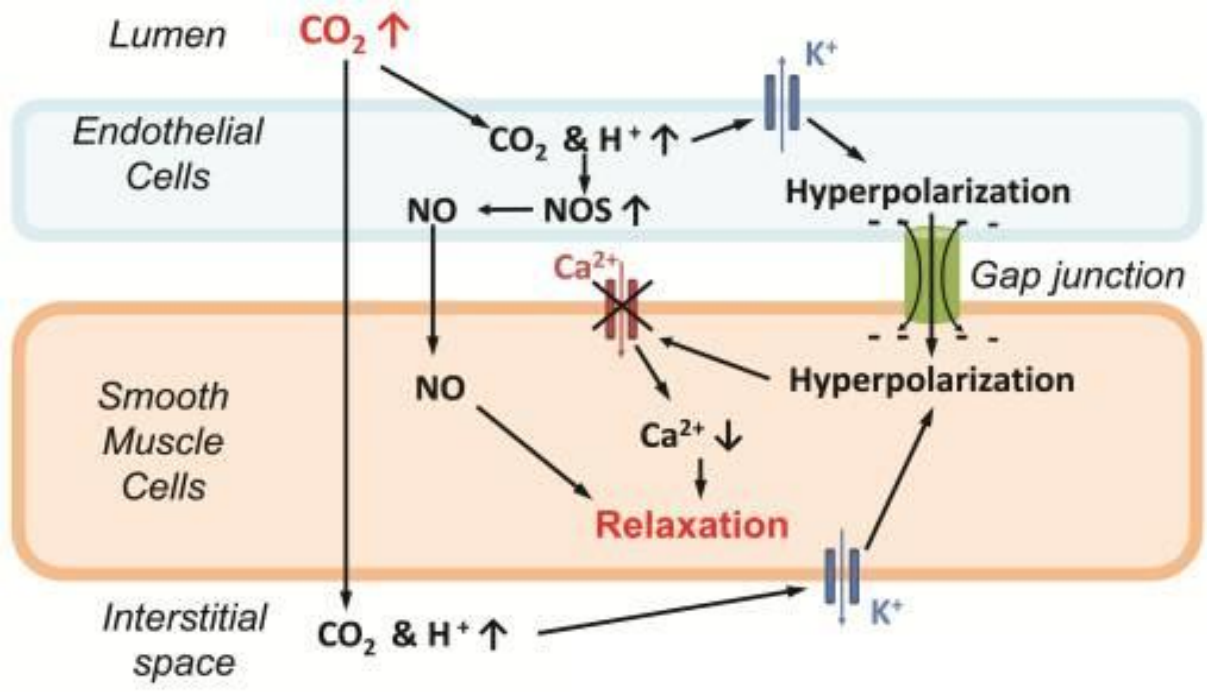

Figure 1.2. Physiological basis of CO_2-induced vascular reactivity (J. J. Chen, 2018)

Illustrated in Figure 1.2 are the two main molecular mechanisms attributed to cerebral vasodilation in response to hypercapnia challenges: 1- a direct mechanism, whereby K^+ channels on smooth muscle cells are opened as a result of both increased CO_2 and decreased pH in interstitial space, thereby causing hyperpolarization, which, in turn, disactivates voltage-dependent Ca^{+2} channels. The resulting reduction in intracellular Ca^{+2} then dilates smooth muscle cells. 2- An indirect mechanism through vascular endothelial cells, either due to hyperpolarization that can change the membrane potentials of the smooth muscle cells via gap junctions, or because of activation of nitric oxide synthase which forms NO. The diffusion of NO into the smooth muscle cells may then result in vasodilation (J. J. Chen, 2018).

As noted above, the hypercapnic-based approaches enable a global cerebrovascular response to elevations in blood CO_2 level, which can then raise the CBF by approximately 3%

(Fierstra et al., 2013; Liu, De Vis, & Lu, 2019). This increase in the CBF would, in turn, increase the level of blood oxygenation, thereby giving rise to a BOLD response. A hypercapnia-induced BOLD response largely reflects the changes in CBF compared with other factors that are typically involved in a BOLD response. In CVR studies, a hypercapnic challenge during BOLD fMRI can be the most suitable test of vasodilatory reserve capacity (Mandell et al., 2008; Pillai & Zaca, 2012). Figure 1.3 shows the relationship between the arterial partial pressure of CO_2 and the percent changes in the BOLD signal as being characterized by a sigmoid curve (Moreton, Dani, Goutcher, O'Hare, & Muir, 2016; Pillai & Mikulis, 2014).

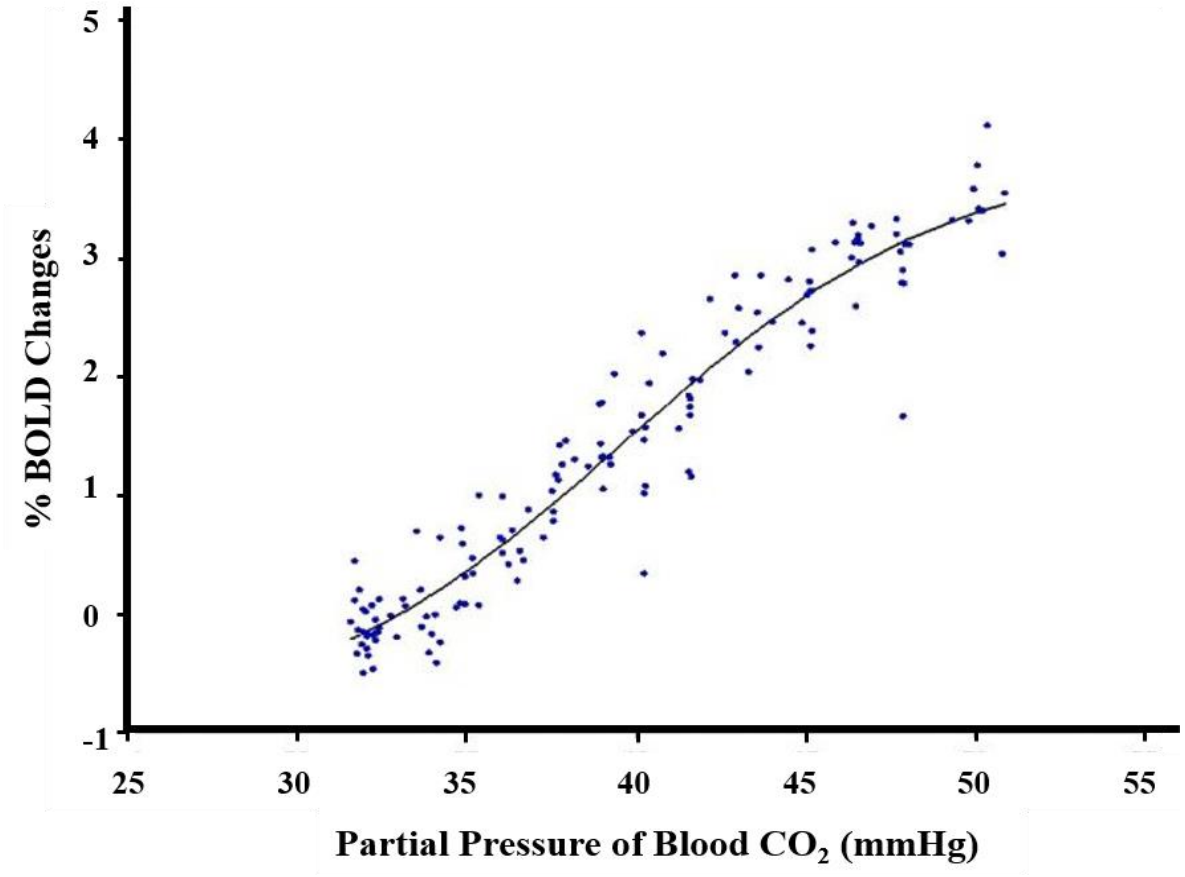

Figure 1.3. The percent BOLD signal changes vs. the partial pressure of blood CO_2 (Pillai & Mikulis, 2014)

Hypercapnia-induced CVR mapping is typically performed by a direct administration of exogenous CO_2; however, from the standpoint of clinical utility, the CO_2-inhaled technique presents practical difficulties, including a lengthy subject preparation and equipment setup time, a need for the precise control of arterial blood gases, and the continuous use of a face mask or nasal cannula within the MRI head coil. (Fierstra et al., 2013; Pillai & Mikulis, 2014; Wu, Bandettini, Harper, & Handwerker, 2015). Furthermore, despite having little CO_2 toxicity, CO_2 gas inhalation may be accompanied by some adverse events such as anxiety or panic, and/or the incidence of transient symptoms, such as dizziness and shortness of breath, in some individuals during the scan, which could potentially undermine the utility of this technique for CVR mapping (J. J. Chen, 2018; Fierstra et al., 2018; J. A. Fisher, Venkatraghavan, & Mikulis, 2018; Gorman et al., 2001; Liu et al., 2019). In addition to the implementation difficulties of these techniques, the exact quantification of CVR may be unnecessary for quality assessment of clinical fMRI activation maps, and would only be required to test the presence or absence of vascular reactivity (i.e. a qualitative test of CVR) (Pillai & Mikulis, 2014). Alternatively, performing a respiratory challenge such as breath holding can rather produce similar results but with less subject discomfort, less preparation time, and less complicated equipment (Kastrup, Kruger, Neumann-Haefelin, & Moseley, 2001; Pillai & Mikulis, 2014; Tancredi & Hoge, 2013).

In breath-hold CVR mapping, it is assumed that holding the breath increases the concentration of intervascular CO_2, which would, in turn, cause the brain-wide vasodilation (Fig. 1.2). The resultant increase of CBF would then lead to an increase in the blood oxygenation level, which could, ultimately, be detected via BOLD-contrast fMRI (Bandettini & Wong, 1997; Kastrup, Li, Glover, & Moseley, 1999; Li, Kastrup, Takahashi, & Moseley, 1999; Madden, 1993).

By providing a direct test of vascular reactivity throughout the entire brain, the breath-hold challenge can reveal brain regions where the vascular response is defective. In the case of lack of task-fMRI activation in these regions, they would, therefore, be imperative to be identified as potential NVU. For example, if fMRI signals are absent for the hand representation of primary motor cortex, the lack of breath-hold induced CVR in this region would then suggest that the task-fMRI response may have been potentially compromised due to NVU rather than neural damage (Pillai & Zaca, 2011; Zaca et al., 2011). To confirm NVU, however, one not only must show a lack of CVR, but also demonstrate that the constituent neurons are still intact. The latter can be accomplished with an appropriately designed behavioral test or other means (DeYoe & Raut, 2014; DeYoe et al., 2015).

Although the breath-hold task can be an effective approach for mapping CVR, this test has practical disadvantages that could potentially limit its widespread clinical use (J. J. Chen, 2018; Fierstra et al., 2013; Spano et al., 2013; Stock et al., 2006). For example, there is a continuous need of monitoring the subject's task performance during the scan. In addition, the breath-hold task may be unsuitable for patients with a large body habitus, chronic pulmonary diseases, or those who are debilitated, unconscious, or unable to comply with the task demands (Spano et al., 2013). Therefore, an alternative approach with less subject cooperation required and fewer technical difficulties that is still capable of detecting changes in BOLD signal to small elevations in blood CO_2 may be needed in the clinical setting.

A brain-wide test of CVR can potentially be performed by using the data from resting-state fMRI, a technique by which subjects are required to breathe regularly at rest without performing any cognitive, language, or motor tasks (J. Jean Chen & Gauthier, 2021; Golestani, Kwinta, Khatamian, & Chen, 2017; Golestani, Wei, & Chen, 2016; Jahanian et al., 2017; Lipp, Murphy,

Caseras, & Wise, 2015; Liu et al., 2017; Liu et al., 2021; Liu et al., 2020). This approach relies on spontaneous fluctuations in intravascular pressure of CO_2 during free breathing to obtain information about the cerebrovascular responsiveness (Birn, Diamond, Smith, & Bandettini, 2006; Birn, Smith, Jones, & Bandettini, 2008; B. B. Biswal, Kannurpatti, & Rypma, 2007; J. Jean Chen & Gauthier, 2021; Golestani, Chang, Kwinta, Khatamian, & Chen, 2015; Jahanian et al., 2017; Kannurpatti, Motes, Biswal, & Rypma, 2014; Kannurpatti, Motes, Rypma, & Biswal, 2011; Liu et al., 2021; Wise, Ide, Poulin, & Tracey, 2004). Based on prior literature, qualitative CVR information can be derived from low-frequency BOLD fluctuations at rest, which, presumably, contain these intrinsic blood CO_2 variations (De Vis, Bhogal, Hendrikse, Petersen, & Siero, 2018; Golestani et al., 2017; Golestani, Kwinta, Strother, Khatamian, & Chen, 2016; Liu et al., 2017; Wise et al., 2004). For example, to assess the responsiveness of cerebral vasculature, one can map a unique metric of low-frequency resting-state, known as amplitude of low-frequency fluctuations (ALFF) (Zang et al., 2007), which has been shown to also be effective in detecting NVU (S. Agarwal et al., 2017; S. Agarwal et al., 2019).

Over the last few years, there has been a growing body of research in support of using the resting-state data to test CVR as an alternative approach to the breath-hold technique (S. Agarwal et al., 2017; Golestani, Wei, et al., 2016; Jahanian et al., 2017; Lipp et al., 2015; Liu et al., 2017); however, the characteristics of the resultant CVR maps are not yet well understood, especially at the resolution of individual voxels and regarding their use for testing the integrity of clinical fMRI activation. It is of great importance to establish the characteristics of CVR metrics when little is known about the extent to which the ALFF metric of resting-state reflects vascular reactivity. Furthermore, it has not yet been determined if tiny elevations in blood CO_2 level during free breathing can efficiently enable testing vasodilatory capacity of cerebral vessels for detecting

potential NVU (S. Agarwal et al., 2017; Birn et al., 2006; De Vis et al., 2018; Golestani et al., 2017; Golestani, Kwinta, et al., 2016; Golestani, Wei, et al., 2016).

It is critical to compare resting-state CVR maps with those derived from breath holding, as the breath-hold approach has been widely accepted by the American Society of Functional Neuroradiology (ASFNR) as the standard technique for testing CVR (Pillai & Mikulis, 2014). The need for a cross-metric comparison is not to develop the best CVR metric but, rather, to understand the degree of agreement between resting-state and breath-hold CVR maps to establish their relative potential for assessing vascular reactivity. Indeed, the two metrics are not required to have identical signal components for clinical utility but, rather, to contain comparable CVR-related physiological components. A comparison between their spatial pattern would allow us to determine whether the two metrics, reflect CVR information in a similar way regardless of possible underlying mechanisms.

To the best of our knowledge, no study has been done to examine the ability of resting-state and breath-hold CVR maps to provide consistent coverage of critical brain areas. This issue becomes more important due to lack of knowledge on how large and/or how common a site of NVU could be in the setting of brain pathology. Therefore, a need exists to develop an understanding of how well these CVR maps can reveal the foci of impaired vascular responses. Finally, while the efficiency of breath-hold CVR maps in the detection of clinical NVU has been tested in a wide range of patients, much less testing has been done using the resting-state CVR maps (S. Agarwal et al., 2017; Black et al., 2017; Hsu et al., 2004; Pak et al., 2017; Para et al., 2017; Pillai & Mikulis, 2014; Pillai & Zaca, 2011, 2012; Zaca et al., 2011; Zaca et al., 2014). Such uncertainty regarding the resting-state fMRI-based metric of CVR could potentially limit its development and use as an imaging biomarker for detecting NVU. Findings from this study could

potentially be used as a prelude to the possible replacement of breath-hold scans by resting-state brain imaging for the purpose of assessing the integrity of vascular reactivity and thus, detecting potential NVU.

Statement of Purpose

The overall purpose of this study was to understand the properties of resting-state CVR maps relative to those derived from the widely accepted approach of breath holding, as a precursor to the development of imaging biomarkers for detecting potential NVU in clinical fMRI brain maps. In particular, our objective was to determine if the resting-state CVR metric is comparable to the breath-hold CVR metric and has similar characteristics. We accomplished this by focusing on three key factors: 1) the quantitative spatial correspondence between the breath-hold and resting-state CVR maps at the resolution of individual voxels, 2) the capacity of the resting-state metric to reveal foci of compromised CVR (absent-signal patches) in comparison with that of breath-hold metric, and 3) the ability of resting-state CVR maps to detect clinical NVU.

The rationale for this research was based on prior literature showing that CVR metrics obtained from both resting-state and breath-hold approaches reflect the responsiveness of underlying cerebrovasculature (Birn et al., 2006; Lipp et al., 2015). Therefore, our central hypothesis was that the resting-state and breath-hold CVR metrics arise from an identical mechanism; for example, both breath-hold and resting-state fMRI metrics of CVR are driven by fluctuations in blood CO_2 levels. If both CVR metrics arise from fluctuations in blood CO_2, then their spatial patterns should be identical, unless other contributing factors to each metric exist that together, influence the two metrics in the same way. Another prediction would be that the spatial

sampling statistics of both CVR metrics (i.e., the probability of occurrence of absent-signal patches on CVR maps) are also the same. Finally, we predicted that resting-state CVR maps would enable detecting NVU in clinical task-fMRI activation maps in a similar manner as breath-hold CVR maps. Accordingly, to test our hypothesis, we pursued the following specific aims.

Specific Aims and Hypotheses

Aim 1: To assess the spatial correspondence between breath-hold and resting-state CVR maps on a voxel-wise basis.

Previous studies have shown a qualitatively good spatial correlation between breath-hold and resting-state metrics of vascular reactivity (Birn et al., 2006; Jahanian et al., 2017; Kannurpatti & Biswal, 2008; Lipp et al., 2015). Nevertheless, the CVR maps derived from frequency-domain resting-state metrics of vascular reactivity have not yet been compared with breath-hold CVR maps at the resolution of individual voxels. Moreover, while thresholding is already widely used in clinical (and academic) settings, the effects of thresholding on the accuracy of spatial overlap between these maps has not yet been studied. In this study, we tested whether resting-state and breath-hold CVR maps are quantitatively equivalent in spatial extent on a voxel-wise basis when threshold criteria are optimally matched.

Aim 2: To determine the spatial sampling statistics of both breath-hold and resting-state CVR holes.

In principle, since the density of microvasculature in gray matter is very high, one would suppose that both breath-hold and resting-state CVR metrics should result in active voxels that are confined

predominantly to cerebral gray matter (Leung, Duffin, Fisher, & Kassner, 2016; Thomas, Liu, Park, van Osch, & Lu, 2014a); however, neither breath-hold nor resting-state CVR maps in healthy individuals completely label all regions of cerebral gray matter.

The discontinuous nature of CVR maps would then add more difficulties in using them to detect NVU by identifying whether an absent-signal patch (hole) is potentially indicative of NVU rather than of random signal losses. Thus, a need exists to statistically explore the continuity and consistency of CVR maps derived from both breath-hold and resting-state data. We hypothesized that a fair coverage of cerebral gray matter could be achieved in healthy individuals by using either breath-hold or resting-state CVR metric, and there would only be small-size holes indicative of random signal losses. Accordingly, for this aim, we tested if:

2.a. The likelihood of observing different-size holes in resting-state CVR maps is equivalent to that of breath-hold CVR maps.

2.b. The occurrence of large holes in cerebral gray matter of healthy individuals is statistically rare using either breath-hold or resting-state metrics of CVR.

Aim 3: To determine if resting-state CVR maps can reveal sites of potential NVU on clinical task-fMRI activation maps.

Based on prior literature, CVR mapping with a breath-hold challenge can effectively detect sites of potential NVU on clinical task-fMRI activation maps (Pillai & Mikulis, 2014). However, this technique has some practical disadvantages. It requires considerable subject cooperation, which could be challenging in clinical studies (J. J. Chen, 2018; Spano et al., 2013). Recently, there have been some attempts to map CVR using low-frequency BOLD signal fluctuations at rest, as such using the resting-state metric of ALFF for testing CVR (Golestani, Wei, et al., 2016). However,

the capability of resting-state CVR maps for detecting clinical NVU has yet to be established. Our hypothesis was that NVU is present only in areas where CVR is impaired. Accordingly, we tested whether holes on resting-state CVR maps spatially correspond to holes on task-fMRI activation maps, where underlying neurons are functionally intact (verified by behavioral data).

Significance

This project provides a comprehensive quantitative comparison between the two breath-hold and resting-state CVR metrics in healthy individuals from both systematic and statistical points of view, thereby establishing the normative characteristics of these metrics as an essential prelude to exploring their use with patients in a subsequent project. While the long-term goal is to use these CVR metrics for detecting potential NVU in patients, the immediate focus of this project was to quantitatively examine the similarity between the spatial patterns of resting-state and breath-hold CVR metrics and the equivalence of their spatial sampling statistics of holes in healthy individuals. It was then required to demonstrate the efficacy of resting-state CVR maps to test the integrity of clinical task-fMRI activation against potential NVU. The results of this project set the stage for more extensive clinical tests with patients having a variety of operable brain pathologies to determine the sensitivity and specificity of the resting-state metric of CVR, thereby ultimately contributing to the development of more effective imaging biomarkers for detecting clinical NVU. A reliable CVR metric to accurately detect potential NVU could provide quality assurance for using the fMRI technique in presurgical brain mapping. In such cases, by indicating potential NVU near a site of treatable brain pathology, complementary electrophysiologic or other behavioral tests can be used to further characterize the functional status of the site and to assess the risk of consequent post-treatment deficits.

If both resting-state and breath-hold CVR maps are effectively equivalent, then the resting-state approach has the advantage of not requiring a separate task and having less computational complications. As the resting-state fMRI technique becomes more widely accepted as an alternative to conventional task-based fMRI scans, both functional and CVR maps can be derived from different components of the same resting-state dataset; one component reflecting correlated neural activity within functionally specific networks, the other reflecting CVR to variations in blood CO_2.

II. Spatial Correspondence Between Resting-State and Breath-Hold CVR Maps

Introduction

The use of blood oxygenation level dependent (BOLD) functional MRI (fMRI) for presurgical brain mapping permits safer, more effective, surgery by allowing neurosurgeons to identify functional (eloquent) cortex close to a site of operable pathology (Hart et al., 2007; Jenkinson et al., 2018; Pillai, 2010; Vysotski et al., 2018). In this context, task-evoked fMRI activation serves as a biomarker for healthy brain tissue and can also indicate functional specificity (Black, Little, & Johnson, 2019; Genetti et al., 2013; Hirsch et al., 2000; Ojemann, 1993; Petrella et al., 2006; Pillai, 2010). Consequently, a lack of fMRI response near or within a site of operable pathology is interpreted as a non-functional region that is safe for surgical removal (Hirsch et al., 2000; Orringer et al., 2012). Yet, this is not always correct. The neurovascular coupling mechanism that underlies task-evoked BOLD responses can be disrupted by focal brain pathology (e.g. tumor), causing reduced or absent fMRI signals despite the presence of functionally intact neurons (Burke & Buhrle, 2006; Holodny et al., 2000; Hou et al., 2006; Pak et al., 2017; Silva et al., 2018; Ulmer, Hacein-Bey, et al., 2004; Voss et al., 2019). Such "neurovascular uncoupling" (NVU) thereby causes false negatives on the fMRI task-activation maps (Para et al., 2017; Pillai & Mikulis, 2014; Ulmer et al., 2003; Zaca et al., 2014). The detection of NVU is critical for the safe, effective use of fMRI in presurgical planning (DeYoe et al., 2015; Pak et al., 2017; Pillai & Mikulis, 2014; Silva et al., 2018). If NVU is undetected, aggressive surgery could result in resection of eloquent cortex,

thereby causing severe post-treatment neurological deficits and a diminished quality of life for the patient (Rahman et al., 2016; Zaca et al., 2011).

Unfortunately, it is not clearly understood how NVU occurs. Several pathophysiological factors have been proposed (Pak et al., 2017; Stanimirovic & Friedman, 2012). For example, NVU may occur in brain tumor patients, whereby an abnormal vascular response may be caused by tumor invasion of tissue surrounding cerebral blood vessels (Lee et al., 2009; Watkins et al., 2014). It has also been shown that an abnormally increased blood volume due to glioma-induced neovascularity may cause a ceiling effect on the BOLD signal (Hou et al., 2006). In contrast, a floor effect on the BOLD signal may result from an atypical amount of deoxygenated hemoglobin in the blood, perhaps due to a lack of sufficient blood flow (Fujiwara et al., 2004; Pillai & Mikulis, 2014). Indeed, a host of potential scenarios involving pathologic alterations in blood flow, volume, oxygenation and other factors could compromise the BOLD response despite preserved neural activity. (Here, for convenience, we use the term NVU to refer to the compromised BOLD response arising from any of these different factors.) Regardless of the exact causes of NVU, it is apparent that the offending pathology could logically occur at any point along the coupling cascade between neurons and the nearby microvasculature. However, there is currently no definitive evidence that NVU results from the disruption of the coupling cascade at early stages without also directly affecting the local vasculature (Watkins et al., 2014). Accordingly, one way to detect potential NVU is to directly test cerebrovascular reactivity (CVR) to changes in the blood concentration of carbon dioxide (CO_2) (Para et al., 2017; Pillai & Mikulis, 2014; Pillai & Zaca, 2011; Zaca et al., 2011; Zaca et al., 2014). CVR can be mapped with fMRI by performing a task consisting of alternating periods of breath-hold and normal breathing (Bright & Murphy, 2013; Kannurpatti, Motes, Rypma, & Biswal, 2010; Murphy, Harris, & Wise, 2011; Peacock et al., 2016;

Pillai & Mikulis, 2014; Tancredi & Hoge, 2013; Urback, MacIntosh, & Goldstein, 2017). Holding the breath is thought to slowly increase the concentration of blood CO_2, which is known for its intrinsic vasodilatory effect (Q. Chen & Anderson, 1997). The resultant rise in cerebral blood flow, ultimately, leads to a global BOLD response (Bandettini & Wong, 1997; Kastrup, Li, et al., 1999). Such a breath-hold challenge can be used as a direct test of vascular reactivity and can identify brain regions where such reactivity is defective (Iranmahboob et al., 2016; Pillai & Mikulis, 2014; Pillai & Zaca, 2011; Voss et al., 2019; Zaca et al., 2011; Zaca et al., 2014). Typically, such a CVR test would be used in conjunction with task-fMRI to help verify that a zone of apparently unresponsive tissue is not actually harboring viable neurons. For example, if fMRI signals are absent for the hand representation of primary motor cortex, the lack of breath-hold induced CVR in this region would suggest that the task-fMRI response may have been compromised due to NVU rather than neural damage (Pillai & Zaca, 2011; Zaca et al., 2011). To verify true NVU (as opposed to dead brain tissue), one must demonstrate that the constituent neurons are still intact, which can be accomplished with an appropriate behavioral test (DeYoe & Raut, 2014; DeYoe et al., 2015).

Although the breath-hold approach for mapping CVR offers advantages in terms of the ease of implementation, reproducibility, and standardization (Bright & Murphy, 2013; Liu et al., 2019; Pillai & Mikulis, 2014), it does have some practical disadvantages. It is not suitable for patients who cannot reliably perform a breath-hold challenge, such as those who are unconscious, debilitated or too young to comply with the task demands. It is also unsuitable for patients with a large body habitus or chronic pulmonary disease (Kannurpatti et al., 2014; Laine, Slama, Petitpretz, Girard, & Motte, 1986). In practice, there can be significant variability in breath-hold performance across patients thereby limiting its utility unless combined with continuous monitoring of end-tidal CO_2 (Bright & Murphy, 2013; Spano et al., 2013; Thomason, Burrows,

Gabrieli, & Glover, 2005; Thomason ME, 2008). Breath-hold following expiration can be more repeatable than breath-hold following inspiration. However, the former is not currently standard of practice because it is more challenging for patients (Pillai & Mikulis, 2014; Scouten & Schwarzbauer, 2008; Thomason, Foland, & Glover, 2007; Wu et al., 2015). Finally, a separate breath-hold task requires additional MRI scan time and thus, higher expense for patients. Given these limitations, an approach based on a similar mechanism but without the need to perform any specific task may provide a better alternative (Chang & Glover, 2009; Golestani, Wei, et al., 2016; Jahanian et al., 2014; Kannurpatti et al., 2014).

A potential alternative to breath-hold for CVR mapping is to use data from resting-state fMRI (Birn et al., 2006; Birn et al., 2008; B. B. Biswal et al., 2007; J. Jean Chen & Gauthier, 2021; Golestani et al., 2015; Golestani, Kwinta, et al., 2016; Golestani, Wei, et al., 2016; Jahanian et al., 2017; Kannurpatti & Biswal, 2008; Kannurpatti et al., 2014; Kannurpatti et al., 2011; Lipp et al., 2015; Liu et al., 2017; Pinto, Bright, Bulte, & Figueiredo, 2021; K. A. Tsvetanov et al., 2015; Kamen A. Tsvetanov et al., 2020; Wise et al., 2004). In this approach, CVR maps can be derived from unique low-frequency (e.g. <0.1 Hz) components of resting-state BOLD signals. Although resting-state fMRI is widely used for the mapping of multiple "functional networks" (B. Biswal, Hudetz, Yetkin, Haughton, & Hyde, 1997; B. B. Biswal, Van Kylen, & Hyde, 1997), similar signal components can also yield information about CVR (De Vis et al., 2018; Golestani et al., 2017; Golestani, Kwinta, et al., 2016; Liu et al., 2017; Yunjie Tong, Hocke, & Frederick, 2019; Wise et al., 2004). Presumably, this is due to spontaneous fluctuations in blood CO_2 during free breathing (Birn et al., 2006; Birn et al., 2008; B. B. Biswal et al., 2007; Liu et al., 2017; Yunjie Tong et al., 2019; Wise et al., 2004). Research has also shown the suitability of investigating the time-delay of these fluctuations for assessing perfusion deficits (Amemiya, Kunimatsu, Saito, & Ohtomo,

2014; Khalil et al., 2017; Ni et al., 2017), and mapping altered brain connectivity (Jahanian, Christen, Moseley, & Zaharchuk, 2018). Recently, it has been shown that the total power of low-frequency resting-state BOLD signals (H. Yang et al., 2007; Zang et al., 2007) provides a metric that can detect tumor-induced NVU on presurgical brain maps (S. Agarwal et al., 2017; S. Agarwal et al., 2018).

Whether resting-state and breath-hold CVR maps are quantitatively equivalent has yet to be established – particularly, at the resolution of individual voxels and with a comprehensive treatment of threshold setting. Previous studies have shown that resting-state maps are quite similar to those obtained from breathing a controlled mixture of exogenous CO_2 (De Vis et al., 2018; Liu et al., 2017). Moreover, both resting-state and breath-hold methods for scaling task-based BOLD signals, appear to be equivalent (B. B. Biswal et al., 2007; Di, Kannurpatti, Rypma, & Biswal, 2013; Kannurpatti & Biswal, 2008; Kannurpatti et al., 2014; Kannurpatti et al., 2011). As part of a research study on the effect of low-frequency fluctuations on task-fMRI activation, Birn et al. (Birn et al., 2006) demonstrated that BOLD amplitudes associated with free breathing at rest are similar to those induced by a breath-hold task. More recently, qualitative comparisons of breath-hold and resting-state patterns of CVR revealed overall good spatial correlation between the two maps (Jahanian et al., 2017; Lipp et al., 2015). Such evidence suggests that CVR metrics obtained from resting-state and breath-hold may arise from the same mechanism, which is thought to be CO_2-induced variations in cerebral blood flow (Birn et al., 2006). If true, then the brain-wide CVR activation patterns of the two metrics should be nearly identical even at the resolution of individual voxels. Consequently, our primary goal was to quantitatively measure the accuracy of spatial correspondence of the breath-hold and resting-state CVR brain maps.

However, there is a significant complication in comparing breath-hold and resting-state CVR metrics in that their spatial patterns are critically dependent on the thresholding criteria used to identify valid responses. Despite being widely used in clinical (and academic) setting, thresholding remains an ongoing, practical issue for CVR (and many other) brain mapping techniques. Therefore, a second goal of this study was to comprehensively determine the effects of threshold settings on the accuracy of spatial overlap between the two CVR maps. In sum, we tested the prediction that breath-hold and resting-state metrics are quantitatively equivalent in spatial extent on a voxel-wise basis when threshold criteria are optimally matched. Establishing the optimum degree of spatial agreement between the two maps will help to clarify their relative potential for mapping vascular reactivity within the brain and will provide a quantitative basis for the development of imaging biomarkers for detecting NVU in clinical cases.

Materials and Methods

Participants

In this study, we recruited nine healthy adults (5 females, mean age 26.5 years, range: 23 – 35 years), with no history of neurological disease. A written, informed consent was obtained from each participant during an interview at the time of first enrollment in the study. Prior to data collection, all experimental procedures were approved by the Institutional Review Board of the Medical College of Wisconsin (protocol PRO00020109).

Experimental Tasks

Breath-hold

The breath-hold task was a block-design paradigm modeled after previous studies and adopted as standard of practice by the American Society of Functional Neuroradiology (Black et al., 2017; Pillai & Mikulis, 2014). Each epoch consisted of a 40 sec interval of normal respiration followed by a 4 sec inhalation and then a 16 sec breath-hold. This pattern was then repeated 4 times and a 20 sec block of normal breathing was added at the end of the four cycles. A 4 sec equilibration period was also added at the beginning of each run for a total scan time of 264 s (132 image volumes). In the MRI scanner, the three task phases were cued by visual text stimuli ('normal breathing', 'inhalation', 'breath-hold') to ensure consistent performance. The presentation of visual stimuli was via a video projector onto a back-projection screen viewed by the subject through a mirror system mounted on the head coil of the MRI system. To maximize each subject's behavioral compliance, the breath-hold task was practiced in a training session prior to scanning. To help verify task performance, we also obtained real-time respiratory bellows data. Each participant performed the breath-hold task two times, and the average of the two was used for further analysis.

Resting-state

The resting-state fMRI images were collected during a 10 min interval for which subjects were instructed to remain relaxed and breathe normally with eyes open and fixed on a central marker on the screen. In addition, a 4 sec equilibration period was added at the beginning of each run. Accordingly, a total of 302 image volumes (604 s) were obtained per run. The resting-state scan was repeated two times for each participant and was performed prior to the breath-hold experiment.

Image Acquisition

MR imaging was performed with a 3 Tesla General Electric Signa Excite 750 MRI scanner at the Medical College of Wisconsin. For each subject, all images were acquired during a single session. T1-weighted anatomical images were acquired using a spoiled, gradient echo (SPGR) pulse sequence with the following parameters: repetition time (TR) = 8.2 ms, echo time (TE) = 3.2 ms, 12° flip angle, field of view of 240 mm, matrix size of 256×224, and 180 axial slices with a 1 mm slice thickness. T2*-weighted gradient echo, echo-planar imaging (EPI) fMRI scans were obtained using a 32-channel RF/gradient head coil with the following parameters: TR = 2000 ms, TE = 30 ms, 77° flip angle, field of view of 240 mm, matrix size = 96×96, and a slice thickness of 5 mm. These parameters resulted in a raw voxel size of 2.5×2.5×5 mm, which was Fourier interpolated to 1.875×1.875×5 mm. A 4 sec equilibration period was utilized for all functional MRI scans to allow for magnetization transients. We also assessed each subject's alertness after each run by asking them to rate their alertness on a scale from 1 – 5, with 1 representing highly drowsy and 5 referring to full alertness. This provided an independent measure of potential data quality and was used as an additional exclusion criterion.

Preprocessing

Data preprocessing was performed using AFNI (http://afni.nimh.nih.gov/afni, version 19.3.11, RRID:SCR_005927) (Cox, 1996). For each subject, the reconstructed datasets were preprocessed using a slightly modified version of AFNI's afni.proc.py script as follows:

For each of the two breath-hold datasets, the equilibration period (4 s) plus the next 10 image volumes (20 s) were removed using AFNI's 3dTcat. In addition, the last 20 volumes (40 s) of each breath-hold dataset were deleted due to a lack of sufficient time to entirely capture the last breath-hold response. This yielded a total of 100 images (200 s) for each of the two breath-hold datasets.

For each of the two resting-state datasets, the equilibration period (4 s) was first removed and then the timeseries was truncated to 210 images (420 s, equivalent to a 7 min scan) and roughly matching the number of data points to be used to compute the breath-hold and resting-state metrics.

The next step was to bring all functional volumes of all runs into spatial alignment with each other and with the skull-stripped T1-weighted anatomical images. This was accomplished as follows: (a) AFNI's 3dToutcount was used to identify a single time point whose associated image volume had a minimum number of voxels with extreme fMRI signal values (outliers). This volume was then used as the base for aligning all other image volumes in the timeseries after first removing any large signal spikes (AFNI's 3dDespike). The alignment process was composed of two stages: the first being co-registration within each timeseries (AFNI's 3dvolreg) and the second being registration to the anatomical dataset (AFNI's align_epi_anat.py). In practice, these two alignments were accomplished in a single step by combining the two transformation matrices (AFNI's 3dAllineate). The preceding alignment process generated six time-course signals corresponding to head movement along three directions of translation and three axes of rotation. The derivatives of the head motion signals were then also computed.

The final preprocessing step was to correct the functional datasets for the effects of head motion artifacts. For this step, the afni.proc.py script was set up so that: (1) Time points in the BOLD fMRI data having particularly aberrant values (Euclidean norm of the motion derivatives > 0.2), were identified. (2) Each voxel's timeseries was then amplitude scaled to a range of 0-200 with a mean of 100 (AFNI's 3dTstat and 3dcalc) (3) The head motion derivatives (see above) were used in a linear regression analysis using AFNI's 3dDeconvolve to model head motion effects. (4) To obtain the final "cleaned" timeseries data, AFNI's 3dTproject was used to first replace by interpolation the timepoints with excessive head motion identified in step 1, and then to regress

out the regression matrix resulting from step 3. It is worth noting that we initially tried using both the original head motion signals and their temporal derivatives to correct datasets for motion. However, examination of the timeseries data revealed that this tended to exclude some legitimate breath-hold-related responses. This was not the case when using only the motion derivatives. Therefore, we used only the motion derivatives for head motion correction. The final cleaned and corrected time-course signals were then used for all subsequent analyses.

Volumes of Interest

For each subject, two volumes of interest were created, one included both cerebral gray and white matter and the second included only cortical gray matter. Using AFNI and FSL (https://fsl.fmrib.ox.ac.uk, version: 6.0.2, RRID:SCR_002823), T1-weighted anatomical images were corrected for nonuniformity by removing possible shading artifacts (AFNI's 3dUnifize). These were then used to generate a brain-only volume (AFNI's 3dSkullStrip). The skull-stripped anatomical images were segmented into three different classes: gray matter, white matter, and cerebrospinal fluid (FSL's FAST segmentation tool) (Y. Zhang, Brady, & Smith, 2001). A whole-brain volume consisting only of the gray and white matter classes was then further processed to eliminate all non-cortical structures. This was accomplished by creating a mask of to-be-excluded structures using Prism View® (http://www.prismclinical.com, RRID:SCR_016977) software in conjunction with the standard MNI ICBM152 template (http://en.wikibooks.org/wiki/MINC/Atlases, RRID:SCR_005281) (Mazziotta, Toga, Evans, Fox, & Lancaster, 1995). The mask covered cerebellum, brainstem, and several structures in the depths of the cerebrum, including corpus callosum, thalamus, hypothalamus, basal ganglia, hippocampus, and subthalamus. For each subject, the mask was then back transformed from MNI space to the

subject's native space. Finally, the mask was used to remove all the non-cortical structures from the whole-brain gray+white matter volume. We refer to the resulting volume as the gray/white matter volume of interest, 'GWM-VOI'. In addition, the white matter volume was removed from the GWM-VOI so as to create a VOI consisting only of cortical gray matter, here termed the 'GM-VOI'.

Data Analysis

CVR data analysis was performed in three major steps: (Step 1) Compute metrics of CVR for each voxel in the GWM-VOI using (1a) the breath-hold data and (1b) the resting-state data. (Step 2) Optimize the spatial correspondence between CVR activation and cortical gray matter by testing a wide range of threshold settings. (Step 3) Optimize and compare the spatial overlap of the breath-hold and resting-state CVR patterns within cortical gray matter by testing a wide range of threshold combinations for both metrics.

Step 1a. Computing the Breath-hold CVR Metric: An initial perusal of the data revealed significant individual differences in the latency and time-course of BOLD responses to the breath-hold task. Consequently, to ensure maximum sensitivity and accuracy for detecting each subject's vascular response to the breath-hold task, we used a unique method to empirically measure the respiratory response waveform for each individual subject as follows: (i) an accurate estimate of the unique waveform of their respiratory response was first obtained; (ii) using this waveform, a breath-hold CVR metric was then computed for each voxel throughout the brain.

(i) To obtain an accurate estimate of the unique waveform of each subject's breath-hold response, we began by identifying a sample of strongly responding voxels (an example waveform

is shown in Fig. 2.1A). This was accomplished computationally by cross correlating an initial estimate of the respiratory response with the empirical fMRI waveform for each voxel. The initial estimate was obtained by convolving the breath hold task timing (Fig. 2.1C) with a generic respiratory response function (RRF), defined by Birn et al. (Birn et al., 2008):

$$RRF = 0.6t^{2.1}e^{-t/1.5}-0.0023t^{3.54}e^{-t/4.25} \quad \text{(Equation 2.1)}$$

The top 1% most highly correlated empirical signals were then averaged, and the resulting waveform was smoothed with a three-point order statistic filter (Cox, 1996), defined as:

$$Y_t=(0.7)\text{median}(X_{t-1}, X_t, X_{t+1})+(1.15)\max(X_{t-1}, X_t, X_{t+1})+(0.15)\min(X_{t-1}, X_t, X_{t+1})$$

(Equation 2.2)

In the above equation, for each time point (t) in the timeseries, the smoothing filter uses 3 input values of X_{t-1}, X_t, and X_{t+1} to compute one output value (Y_t). Such filtering helped avoid having the fit be driven by spurious noise components, thereby yielding a better approximation of the subject's respiratory response (Fig 2.1B). The smoothed timeseries was then used for the subsequent analyses.

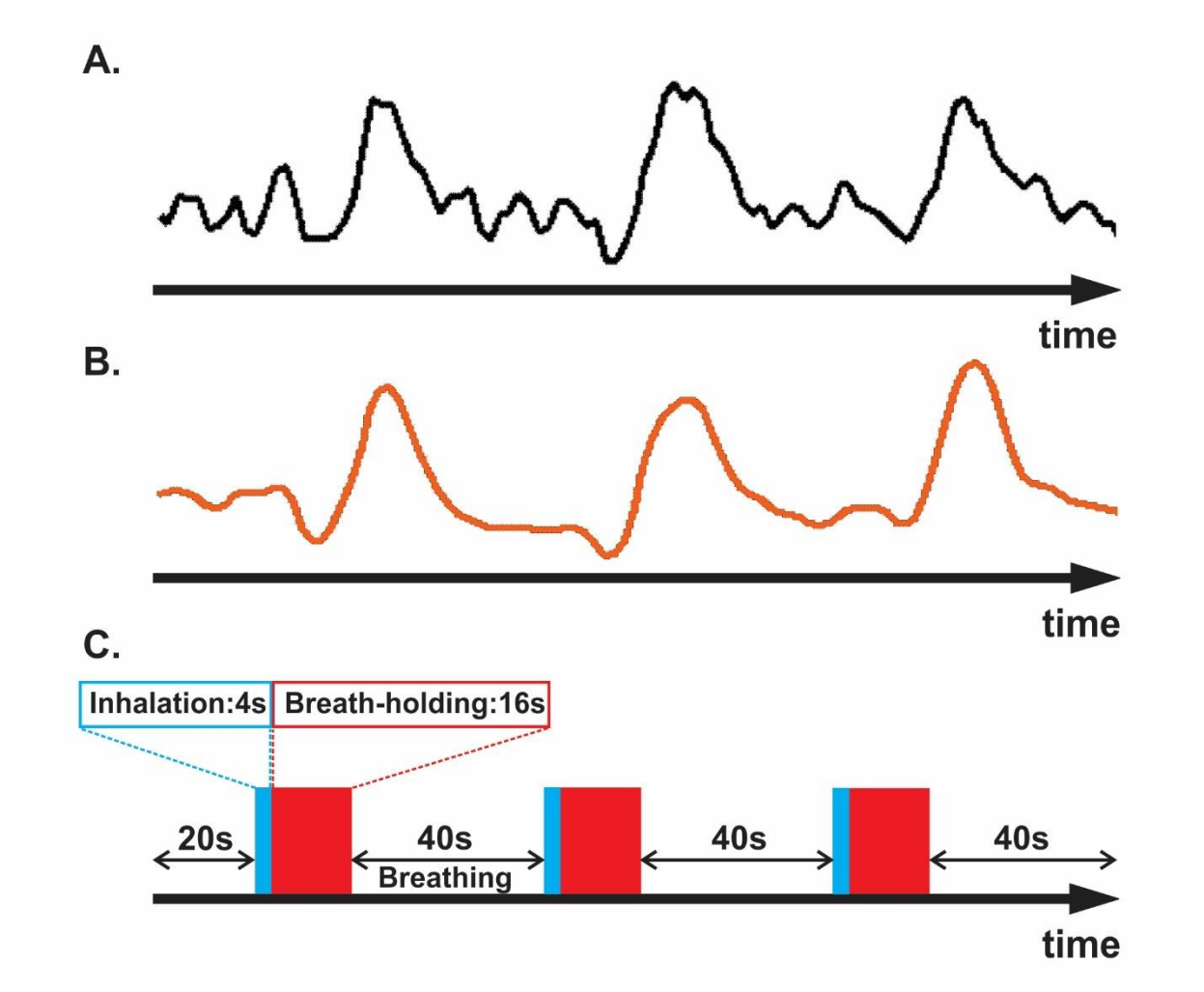

Figure 2.1. (A): Averaged empirical breath-hold BOLD time series for a representative subject. (**B):** The subject's estimated respiratory response waveform. (**C**): Breath-hold task consisting of three epochs of 4 sec inhalation (blue), 16 sec breath-hold (red), and 40 sec normal breathing.

(ii) To compute final breath-hold CVR metrics, each subject's personalized respiratory response was used in a general linear regression analysis against the original empirical breath-hold time-series using AFNI's 3dDeconvolve. This was performed by shifting the subject's personalized respiratory response from 0 to 4 TR relative to each voxel's empirical time-series and computing a regression fit coefficient (beta) for each time delay. For each voxel, the most statistically significant beta coefficient was then used as the final breath-hold CVR metric.

Step 1b. Computing the Resting-state CVR Metric: The resting-state fMRI signal power within a frequency band from 0.01 to 0.08 Hz, known as the Amplitude of Low Frequency Fluctuation (ALFF), was used directly as the resting-state metric for each voxel (H. Yang et al., 2007; Zang et al., 2007). We will refer to the ALFF metric as the resting-state "CVRe" metric, where the "e" implies "estimate".

Step 2. Optimizing Overlap of CVR Maps with Gray Matter: The CVR activation pattern is thought to be confined predominantly to gray matter because of the latter's high density of microvasculature (Thomas et al., 2014b). Therefore, for each metric, we first searched for a threshold setting that would optimize the spatial correspondence between the CVR activation pattern and cortical gray matter, while also minimizing CVR activation appearing artifactually in white matter. This was done independently for both the breath-hold and resting-state maps by exploring a range of threshold criteria and classifying voxels at each threshold setting as CVR responsive or not. Accordingly, for each threshold setting, voxels were classified as either: true positive (TP), true negative (TN), false positive (FP), or false negative (FN) as defined in Table 2.1A. Such a classification thus yielded one of the four binary combinations of 11, 00, 10, and 01 for each voxel. The analysis was restricted to the GWM-VOI, and the resulting classification proportions were reported in a two-by-two contingency table (see Appendix A). At each threshold setting, the overlap between the resulting CVR activation pattern and cortical gray matter was assessed using accuracy (Acc) and Dice coefficients computed as:

$$\text{Acc} = \frac{\text{TP+TN}}{\text{TP+TN+FP+FN}} \qquad \text{(Equation 2.3)}$$

$$\text{Dice} = \frac{2\text{TP}}{2\text{TP+FP+FN}} \qquad \text{(Equation 2.4)}$$

For each metric, this process was repeated over a full range of threshold settings to find the optimal threshold that maximized the accuracy of spatial overlap (as defined by equation 2.3 above). A custom MATLAB program was used to perform this analysis.

Step 3. Comparing Breath-hold CVR and Resting-state CVRe Maps: Having first established thresholds that optimized overlap of CVR maps with gray mater, we directly compared the breath-hold CVR and resting-state CVRe patterns with each other by again exploring a full range of potential thresholds for each metric. To quantify the spatial overlap of the two maps, we again classified voxels according to the presence or absence of a response for each metric and for each different pair of threshold settings. Arbitrarily, we used the resting-state CVRe metric as a logical "predictor" of the breath-hold CVR metric. Voxels were classified as either: true positive (TP), true negative (TN), false positive (FP), or false negative (FN) as defined in Table 2.1B. The resulting voxel proportions for each threshold pair were reported as a two-by-two contingency table (see Appendix A) and used to compute correspondence accuracy (equation 2.3) and Dice coefficient (equation 2.4).

Table 2.1. Voxel-wise Classification in **(A):** CVR vs. Gray Matter Comparisons, and **(B)** Resting-state CVRe vs. Breath-hold CVR Comparisons. **GM:** Gray Matter; **TP:** True Positive; **TN:** True Negative; **FP:** False Positive; **FN:** False Negative; 1 = Present; 0 = Absent.

Voxel-wise Classification

A. CVR vs. GM Comparison			**B. Resting-state CVRe vs. Breath-hold CVR Comparison**		
Class	**CVR**	**GM**	**Class**	**Resting-state CVRe**	**Breath-hold CVR**
TP	1	1	TP	1	1
TN	0	0	TN	0	0
FP	1	0	FP	1	0
FN	0	1	FN	0	1

Results

In accordance with the structure of our data analysis, we discuss the results in two main sections: (1) the association of CVR-responsive voxels with gray versus white matter and (2) a voxel-wise comparison of the breath-hold CVR and resting-state CVRe maps with each other. In both instances, the comparisons were highly dependent on the threshold criteria used to identify CVR responsive voxels, but in both cases, clearly optimal threshold settings that maximized the spatial correspondence could be identified.

CVR vs. Gray Matter

As illustrated in Figures 2.2A and 2.2B, the accuracy of spatial correspondence between gray matter and both the breath-hold CVR and resting-state CVRe metrics varied dramatically with CVR threshold setting. The accuracy was calculated as the summation of CVR-responsive voxels in gray matter (true positive) and non-responsive voxels in white matter (true negative) relative to the total number of voxels (equation 2.3 above). For both metrics, there was a clear

optimum threshold that maximized the correspondence accuracy. The inset figures in Figure 2.2A and 2.2B make this relationship clearer by showing that at low thresholds there is inappropriate labeling of white matter, whereas at high thresholds, the labeling becomes too sparse in gray matter. At the threshold of maximum accuracy (Thresholds 0.4 and 40 in Fig. 2.2A and 2.2B, respectively), labeling of gray matter is high yet inappropriate labeling of white matter is low. The resultant breath-hold CVR and resting-state CVRe maps at these optimum threshold settings (maximizing correspondence accuracy) are shown in Figures 2.2C (red voxels) and 2.2D (green voxels), respectively.

Complete analyses for the CVR vs. gray matter comparisons (at optimal thresholds) are shown in Tables 2.2 and 2.3 for the resting-state CVRe and breath-hold CVR metrics, respectively. For all subjects, paired t-tests revealed that CVR/gray-matter overlap accuracy and Dice scores were significantly higher for resting-state than for breath-hold (Acc: 71.7 ± 3.7% vs. 63.1 ± 4.7%, $p < 0.01$; and Dice: 74.2 ± 3.4% vs. 65.8 ± 4.3%, $p < 0.01$). Tables 2.2 and 2.3 suggest that the better accuracy of resting-state reflects its relatively higher labeling within gray matter (TP: resting-state 40.8 ± 2.9%, vs. breath-hold 35.6 ± 3.3%, $p < 0.01$) and better avoidance of white matter (TN: resting-state 30.9 ± 3.3%, vs. breath-hold 27.6 ± 4.3%, $p < 0.01$). In other words, resting-state CVRe is more selectively localized to gray matter than breath-hold CVR. This is also qualitatively evident in Figures 2.2D vs. 2.2C for a representative subject.

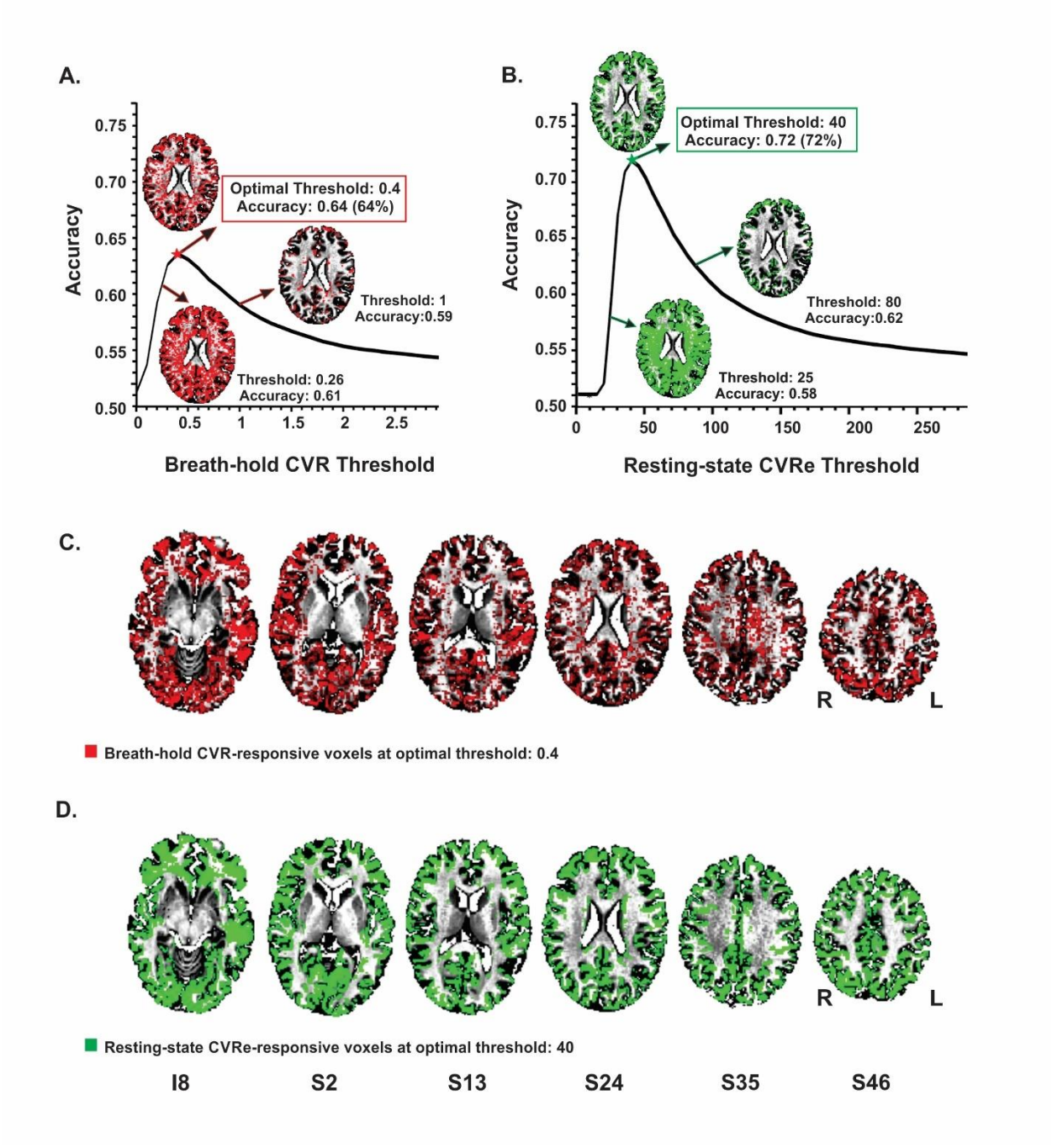

Figure 2.2. Optimizing thresholds to maximize accuracy of spatial overlap between CVR responses and gray matter. (**A):** Breath-hold CVR accuracy vs. threshold with example CVR brain patterns (red) for thresholds of 0.26, 0.4, and 1. **(B):** Resting-state CVRe accuracy vs. threshold with example CVR brain patterns (green) for thresholds of 25, 40, and 80. By decreasing the threshold from 1 to 0.26 in A, and from 80 to 25 in B, more complete coverage of the gray matter is obtained but at the cost of inappropriate labeling of white matter. (**C), (D):** Axial brain maps for thresholds marked by stars in A, and B that optimized overlap accuracy of gray matter with breath-hold CVR (C: red) and resting-state CVRe (D: green). Labels below images indicate relative slice position in mm (**I:** inferior, and **S:** superior). Accuracy is defined in equation #3. Slice right/left (R/L) orientation is radiologic standard.

Table 2.2. Voxel-wise Correspondence of Resting-state CVRe and Gray Matter. Accuracy and Dice coefficients (right columns) were computed from the voxel classification data (middle columns) using equations 2.3 and 2.4. Voxel classification procedures are described in Methods. This analysis was limited only to the gray and white matter volume of interest. **Acc:** Accuracy, **Dice:** Dice coefficient, **TP:** True Positive, **TN**, True Negative, **FP**, False Positive, **FN:** False Negative, **Ave:** Average, **SD**: Standard Deviation

Voxel-wise Correspondence of Resting-state CVRe and Gray Matter

Subject	TP (%)	TN (%)	FP (%)	FN (%)	Acc (%)	Dice (%)
#1	45	32	15	8	77	79.7
#2	41	35	17	7	76	77.4
#3	39	33	13	15	72	73.6
#4	37	30	22	11	67	69.2
#5	38	35	15	12	73	73.8
#6	42	32	18	8	74	76.4
#7	45	26	22	7	71	75.6
#8	41	27	21	11	68	71.9
#9	39	28	22	11	67	70.3
Ave ± SD	**40.8 ± 2.9**	**30.9 ± 3.3**	**18.3 ± 3.5**	**10 ± 2.3**	**71.7 ± 3.7**	**74.2 ± 3.4**

Table 2.3. Voxel-wise Correspondence of Breath-hold CVR and Gray Matter. Accuracy and Dice coefficients (right columns) were computed from the voxel classification data (middle columns) using equations 2.3 and 2.4. Voxel classification procedures are described in Methods. This analysis was limited only to the gray and white matter volume of interest. **Acc:** Accuracy, **Dice:** Dice coefficient, **TP:** True Positive, **TN**, True Negative, **FP**, False Positive, **FN:** False Negative, **Ave:** Average, **SD**: Standard Deviation

Voxel-wise Correspondence of Breath-hold CVR and Gray Matter

Subject	TP (%)	TN (%)	FP (%)	FN (%)	Acc (%)	Dice (%)
#1	36	31	17	16	67	68.6
#2	37	33	19	11	70	71.2
#3	36	28	19	17	64	66.7
#4	29	28	24	19	57	57.4
#5	34	30	20	16	64	65.4
#6	35	31	19	15	66	67.3
#7	41	24	24	11	65	70.1
#8	34	23	25	18	57	61.3
#9	38	20	30	12	58	64.4
Ave ± SD	**35.6 ± 3.3**	**27.6 ± 4.3**	**21.9 ± 4.1**	**15 ± 3**	**63.1 ± 4.7**	**65.8 ± 4.3**

Breath-hold CVR vs. Resting-State CVRe

Figure 2.3 illustrates the effect of threshold setting on the accuracy of spatial correspondence between the breath-hold CVR and resting-state CVRe activation patterns. In this case, the accuracy calculations were restricted just to the cortical gray matter ROI (GM-VOI). (However, brain images in Figure 2.3 show labeling of both gray and white matter). The resulting 3-dimensional accuracy surface was saddle-shaped as illustrated in Figure 2.3A. The threshold

settings that were determined in the previous analysis to optimize the correspondence of each CVR map with gray matter are indicated by the dashed arrows (red for breath-hold and green for resting-state) with the corresponding accuracy indicated by the star at mid-point of the saddle-shaped surface. The corners of the surface are associated with extreme threshold settings that force all voxels to be classified as active for both metrics (A4), only breath-hold CVR (A3), only resting-state CVRe (A2), or neither metric (A1). This was true for all subjects even though the precise shape of the surface varied somewhat from subject to subject.

As illustrated in Figure 2.3B, superimposing the two optimized patterns shows that they cover roughly the same regions but are not identical (matching voxels in yellow). The resting-state CVRe pattern (green + yellow) appears to demonstrate more complete coverage of gray matter with less encroachment into white matter. In contrast, the breath hold pattern (red + yellow) has excessive, inappropriate labeling of white matter.

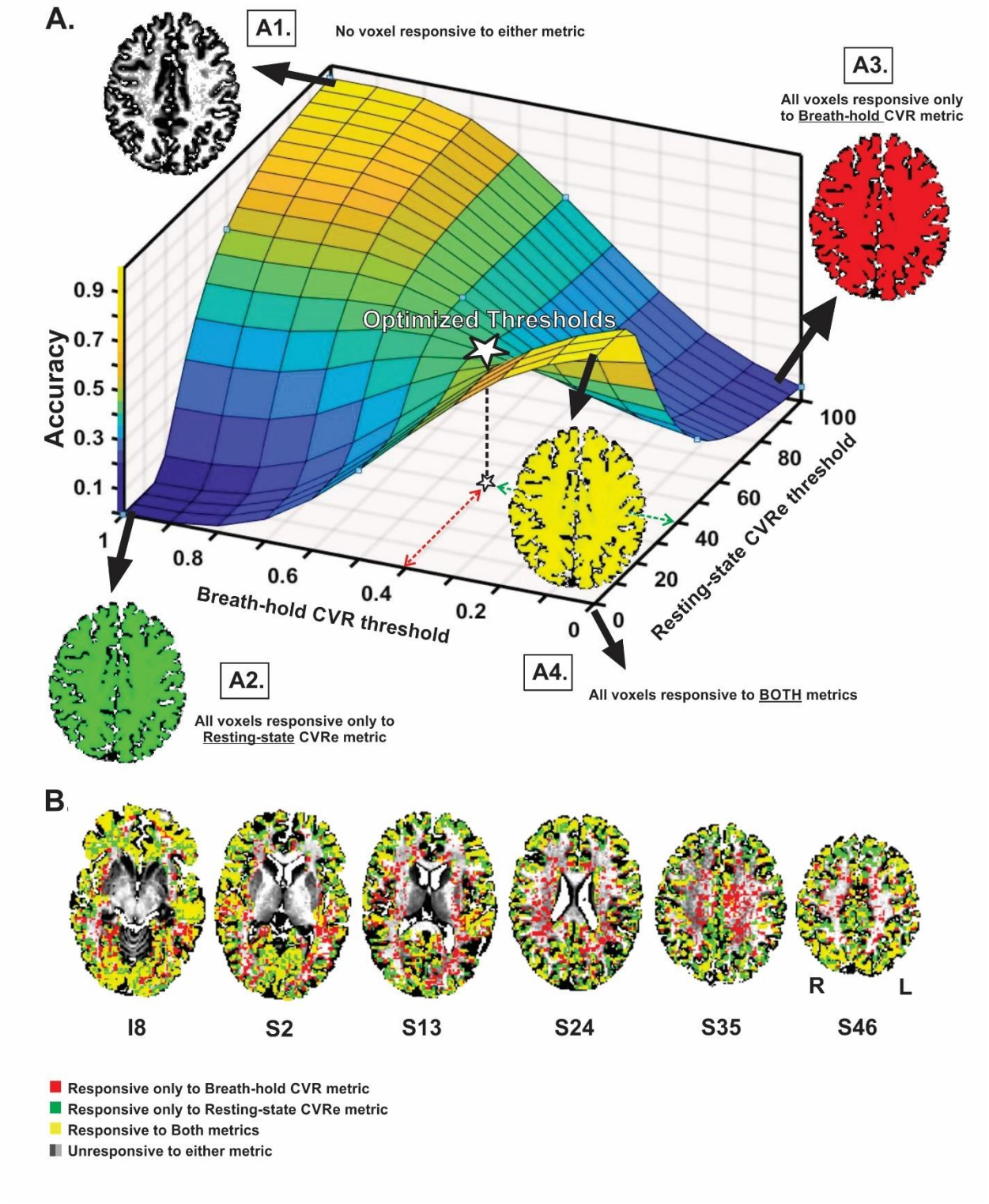

Figure 2.3. (**A):** Accuracy of spatial correspondence between breath-hold and resting-state CVRe within cortical gray matter as a function of threshold. Optimal threshold pair that maximized segregation of CVR responses to gray matter shown by dashed red and green arrows. Accuracy for those optimal thresholds is indicated by star. Moving threshold settings towards biased corners forces all voxels to be classified as CVR responsive to one (A2, A3), both (A4) or

neither (A1) CVR metric. (**B):** Axial brain images with overlaid CVR activation maps at optimal threshold settings (0.4 and 40 for breath-hold and resting-state CVRe maps, respectively). Labelling in gray and white matter is illustrated though accuracy measures pertain to the gray matter VOI only. Voxel color code indicated at lower left. Labels under slice images indicate relative slice position in mm (**I:** inferior, and **S:** superior). Labels below the slice image in the right show the orientation of all slice images (**R:** right, and **L:** left).

Table 2.4 shows the complete analysis quantifying the spatial correspondence between the breath-hold CVR and resting-state CVRe activation patterns for all subjects. In this case the computations were restricted only to voxels within gray matter (GM-VOI). At the level of individual voxels, the mean accuracy of spatial correspondence between the two metrics was 73.6 ± 3.4%, ranging from 69% to 81%. Similarly, the Dice coefficients ranged from 77% to 88.3% with an average of 82.2 ± 3%.

Table 2.4. Voxel-wise correspondence of Resting-state CVRe and Breath-hold CVR. Resting-state CVRe was used as a predictor of Breath-hold CVR. Accuracy and Dice coefficient metrics of spatial correspondence (right columns) were computed from the voxel classification data (middle columns) using equations 2.3 and 2.4. Voxel classification procedures are described in Methods. This analysis was limited only to the gray matter volume of interest. **Acc:** Accuracy, **Dice:** Dice coefficient, **TP:** True Positive, **TN**, True Negative, **FP**, False Positive, **FN:** False Negative, **Ave:** Average, **SD**: Standard Deviation.

Voxel-wise Correspondence of Resting-state CVRe and Breath-hold CVR Patterns

Subject	TP (%)	TN (%)	FP (%)	FN (%)	Acc (%)	Dice (%)
#1	65	9	20	6	74	83.3
#2	72	9	13	6	81	88.3
#3	59	14	17	10	73	81.4
#4	52	17	25	6	69	77
#5	56	18	18	8	74	81.2
#6	62	11	23	4	73	82.1
#7	65	9	22	4	74	83.3
#8	62	13	19	6	75	83.2
#9	60	10	18	12	70	80
Ave ± SD	**61.4 ± 5.7**	**12.2 ± 3.5**	**19.4 ± 3.6**	**6.8 ± 2.4**	**73.6 ± 3.4**	**82.2 ± 3**

Unthresholded Breath-hold CVR vs. Resting-State CVRe

Although our primary goal in this study was to compare breath-hold and resting-state metrics as they have typically been utilized in the clinical field with thresholding, it is informative to briefly compare the unthresholded metrics. Figure 2.4A illustrates a scatter plot of the unthresholded metrics (after normalization of their respective amplitude ranges) for a representative subject. There was a moderate linear correlation of the two metrics ($r = 0.50$) but with significant scatter. This result was consistently obtained for all subjects (mean correlation =

0.53). The spatial distribution of the unthresholded metrics within the GWM-VOI are illustrated for a representative subject in Figures 2.4B and 2.4C. To contrast the two distributions, we computed the difference between the two metrics for each voxel (after normalization of their respective amplitude ranges). Figure 2.4D illustrates the brain pattern of this difference metric. Consistent with our original analysis, this shows that there are no obvious large regions of significant mismatch between the breath-hold CVR and resting-state CVRe metrics. The local voxel-wise differences are more or less randomly distributed throughout gray matter.

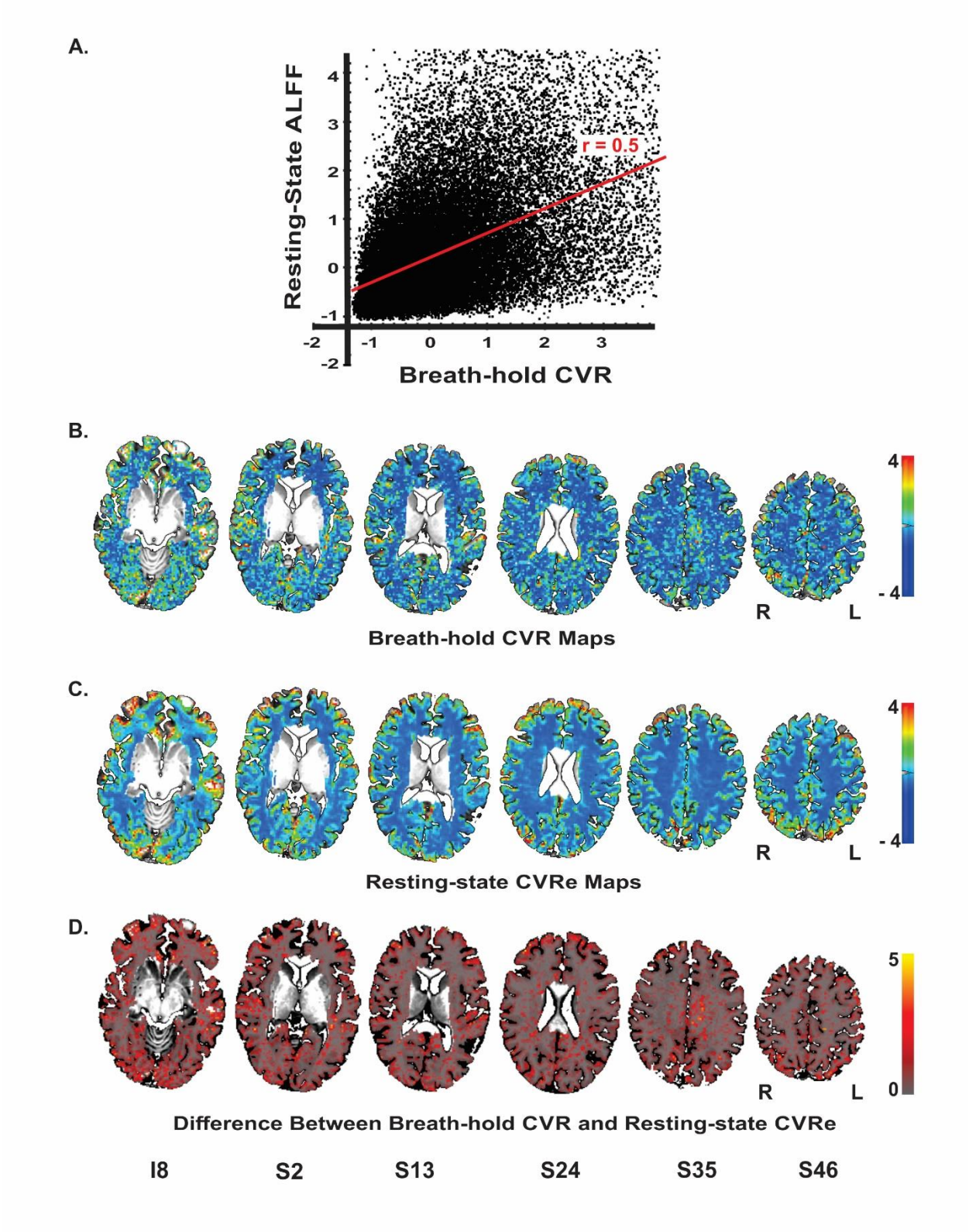

Figure 2.4. Unthresholded Breath-hold CVR vs. Resting-state CVRe. (**A):** Scatterplot of the unthreshold resting-state and breath-hold CVR metrics for a representative subject. Each point represents one voxel in the cortical gray matter.

Full range of data has been clipped to 95% of voxels. The two metrics are correlated with a correlation coefficient of 0.50. (**B), (C), and (D):** Axial brain images with overlaid unthresholded maps of breath-hold CVR (B), resting-state CVRe (C), and difference metric (D). Voxel color code indicated at right. Labels under slice images indicate relative slice position in mm (I: inferior, and S: superior). Slice right/left (R/L) orientation is radiologic standard.

Discussion

The primary goal of this study was to compare a resting-state metric to a widely accepted breath-hold CVR metric to determine if their activation patterns were spatially equivalent at a voxel level of resolution appropriate for presurgical brain mapping. Since local blood flow regulation within cerebral cortex is largely controlled by gray matter microvasculature, we first identified threshold settings for each metric that optimized gray matter coverage while minimizing artifactual spread into white matter. Having spatially optimized CVR responses in this manner, we then quantified the degree of spatial overlap of the two metrics on a voxel-by-voxel basis (see Appendix C).

The main findings of this study are: (1) The correspondence between breath-hold CVR and resting-state CVRe maps and their association with cortical gray matter are highly dependent on the CVR threshold settings. (2) Both breath-hold and resting-state metrics have clearly optimal thresholds that maximize their coverage and segregation relative to gray versus white matter. (3) At optimal threshold settings, the spatial pattern of activation for the two metrics differs significantly at a voxel level of resolution with the resting-state metric providing better coverage and segregation to cortical gray matter. (4) At the voxel level, the two metrics had moderate overlap accuracy, ranging from 69% to 81% overlap with a mean of 73.6%. Despite this modest correspondence at the voxel scale, the patterns were nevertheless qualitatively consistent on a more global scale as reported previously by others (Jahanian et al., 2017; Lipp et al., 2015). These results

allow us to reject our prediction that "the breath-hold and resting-state metrics are quantitatively equivalent in spatial extent on a voxel-wise basis when threshold criteria are optimally matched".

Our results showed that, when optimized, cross-metric correspondence accuracy was relatively modest ranging from 69-81% across our nine subjects. One might ask why this result seems somewhat at odds with previous reports of good correspondence using breath-hold and/or resting-state metrics as indicators of healthy versus impaired CVR (S. Agarwal et al., 2017; De Vis et al., 2018; Iranmahboob et al., 2016; Jahanian et al., 2017; Liu et al., 2017; Pillai & Zaca, 2011; Christiaan Hendrik Bas van Niftrik et al., 2016; Zaca et al., 2011; Zaca et al., 2014). The critical effect of optimizing threshold selection in the present study is likely the most important difference between our approach and those of previous studies, where CVR thresholds were often set by z-score significance as in task-fMRI or to obtain full coverage of gray matter (Jahanian et al., 2017; Lipp et al., 2015). Our approach of optimizing threshold settings for each individual was motivated by clinical utility in which a patient-specific approach is paramount. This is somewhat different from previous studies that were focused on comparing metrics across subjects (Lipp et al., 2015).

We felt that it was important to examine the correspondence of our CVR metrics at a voxel resolution of 2.5×2.5×5 mm which is generally consistent with current clinical studies. In contrast previous studies have often used larger voxel sizes (Golestani, Wei, et al., 2016; Jahanian et al., 2017) and/or coarse spatial smoothing with a 4-8 mm FWHM kernel (S. Agarwal et al., 2017; De Vis et al., 2018; Iranmahboob et al., 2016; Lipp et al., 2015; Liu et al., 2017; Pillai & Zaca, 2011; Christiaan Hendrik Bas van Niftrik et al., 2016; Zaca et al., 2011; Zaca et al., 2014). This tends to produce artifactually uniform and continuous maps thereby obscuring their true discontinuous nature as documented in the present study. Heavy smoothing also will obscure smaller CVR

anomalies making the detection of large (relatively rare) dropouts more reliable at the expense of spatial precision. The potentially smallest detectable CVR dropout is unclear, in part, because the precision of microvascular control is poorly defined (Attwell et al., 2010), but may reflect the 1-2mm spacing of individual arterioles that penetrate cortical gray matter (Duvernoy, Delon, & Vannson, 1981; El-Bouri & Payne, 2016). If so, routine use of smaller imaging voxels and less smoothing might enhance the detection of more subtle CVR defects that may prove to be of clinical relevance.

It should be stressed that our study was focused on providing a quantitative measure of how well the patterns of the two CVR metrics agreed for individual subjects (ultimately patients), not on proving that the spatial patterns or the level of agreement were the same across individuals. Consequently, the most relevant statistical issue was the rate of agreement across the thousands of voxels within each individual. While such a descriptive statistic is sufficient for this purpose, we also did test multiple subjects. This was to illustrate the consistency of correspondence across a sample of individuals, but not to test whether it was identical across subjects. Nevertheless, we did find that the rate was surprisingly consistent, varying by only 3.4% across our sample of 9 subjects (Table 2.4.).

A second important goal of our study was to critically examine the effects of threshold settings on the spatial properties and correspondence of breath-hold and resting-state metrics. This was motivated by the fact that thresholding of CVR and fMRI maps is ubiquitous in the literature and in current clinical practice. Yet, its effects are rarely explored systematically and comprehensively. In the present study, we explored wide ranges of threshold settings in order to show that the spatial correspondence of the two metrics varies significantly, but in understandable ways, with changes in threshold. We feel that this is an important caveat to the interpretation of

previous studies that examined the spatial patterns of the two metrics. Typically, an arbitrary or poorly justified threshold was used for the classification of voxels as being CVR responsive or not (Cohen & Wang, 2019; De Vis et al., 2018; Golestani, Wei, et al., 2016; Jahanian et al., 2017; Lipp et al., 2015; Liu et al., 2017; Pillai & Zaca, 2011; Zaca et al., 2011; Zaca et al., 2014). Indeed, it was not uncommon for the threshold settings in previous studies to be adjusted to obtain full coverage of gray matter while ignoring potentially inappropriate coverage of white matter. It was also quite common for CVR maps to be thresholded in the same manner as task-based fMRI activation despite having different physiological bases (S. Agarwal et al., 2017; Jahanian et al., 2017). Such approaches can result in an inflated rate of false positive CVR responses, thereby underestimating the occurrence of zones having compromised CVR (Lipp et al., 2015; Liu et al., 2017), which in a surgical scenario, can increase the risk of ablation of viable brain tissue. Notably, even after optimizing threshold settings, the accuracy of overlap of our CVR metrics with gray matter tended to be modest (approx. 70%-80%) at its maximum. This reflected a combination of incomplete labeling of gray matter with some inappropriate CVR activation within white matter. However, this is precisely the goal of using an unbiased criterion to optimize the threshold selection. Note that simply maximizing sensitivity does not explicitly take into account the concurrent effect on proliferation of false positives. Indeed, arbitrarily lowering the CVR threshold to obtain more complete labeling of gray matter (i.e. to maximize detection of true positives) will unavoidably increase inappropriate labeling of white matter (i.e. increased rate of false positives) resulting in a reduction of overall correspondence accuracy (Fig. 2.2A and 2.2B). To be clear, however, we do not advocate that thresholding of clinical CVR maps is necessarily the best way to analyze the data. Rather, our purpose here is to ensure that if practitioners do elect to threshold

their brain maps, that they are aware that arbitrary selection of the threshold settings can produced a biased map.

Interestingly, our exploration of a wide range of threshold settings for the cross-metric CVR comparison produced a saddle-shaped accuracy surface, wherein the optimal thresholds obtained in the CVR vs. gray matter comparison were located at, or very close to, the center of the surface (white star in Fig. 2.3A). From a methodological standpoint, the saddle area represents the best accuracy attainable without artificially pushing the thresholds toward the biased corners of the surface where extreme settings artificially force all voxels to be classified as responsive or not (Fig. 2.3, A1-A4). For example, inset Figure 2.3., A4 illustrates how threshold values at the front corner force all voxels to be true positive (TP), meaning that they are all classified as responsive for both resting-state CVRe and breath-hold CVR metrics thereby forcing the correspondence accuracy to be 1.0 (100%). In other words, the more that threshold settings are forced toward the corners, the more biased the accuracy value becomes. We stress that this is an important point that both clinicians and researchers should note: Arbitrary adjustment of thresholds is very likely to create a biased CVR map!

Besides the importance of thresholding in creating unbiased CVR maps, we also found that the optimal thresholds for best segregation of CVR responses to gray matter corresponded precisely with the thresholds that were independently optimized for unbiased comparison of the two metrics with each other. From a conceptual standpoint, a likely explanation is that maximizing the CVR spatial overlap relative to gray versus white matter may also effectively optimize the patterns to reflect the spatial distribution of the underlying vascular structures that produce CVR signals and are known to be concentrated in gray matter. Note that while the fortuitous match

between the two sets of thresholds does not prove our assumption that true CVR signals should primarily arise from the highly vascularized gray matter, it is consistent with its general validity.

Although we comprehensively explored the effects of thresholding, we also cross-checked our overall conclusions about the spatial characteristics of the two metrics by examining unthresholded CVR maps and an unthresholded difference metric (Fig. 2.4). We showed that the breath-hold and resting-state metrics are indeed quantitatively correlated though somewhat loosely (Fig. 2.4A). Thus, both the unthresholded maps and analysis are consistent with our conclusion that, overall, the two metrics are grossly similar in amplitude and spatial distribution but can vary significantly at the voxel level.

A potentially important limitation of this study is that it focuses on breath-hold CVR and resting-state CVRe metrics that are both thought to primarily test the vascular responsiveness to variations in blood CO_2 levels. As a potential indicator of disrupted CVR, vasoactivation represents only one stage in the complex cascade of physiological events linking neuronal activity to an fMRI response. In principle, neurovascular coupling could fail due to pathological effects on earlier stages of the cascade prior to the vascular smooth muscle response. Whether this can actually occur in clinical practice is unknown but physicians who are responsible for interpreting the results of CVR testing should be made aware of this potential caveat.

Our prediction that breath-hold and resting-state CVR metrics would produce matching brain maps was based on the premise that both arise from ongoing changes in blood CO_2 levels. Although, our observations of significant cross-metric correspondence are consistent with this scenario, the lack of a closer correspondence at the voxel level suggests that additional neuronal and/or physiological factors (such as cardiac pulsation or respiration) may cause some variability in the two maps (Chu, Golestani, Kwinta, Khatamian, & Chen, 2018; Golestani et al., 2017;

Golestani, Kwinta, et al., 2016; K. A. Tsvetanov et al., 2015; Kamen A. Tsvetanov et al., 2020). For example, artifactual labeling of white matter in the breath-hold CVR maps may partly reflect head motion that typically accompanies the active breath-hold task thereby reducing overlap accuracy. (This may also account for the more selective and complete coverage of gray matter by the resting-state metric.) On the other hand, resting-state ALFF may not exclusively reflect CVR alone, but also may contain contributions from other neuronal and/or physiological factors such as cardiac pulsation and respiration (S. Agarwal et al., 2017; De Vis et al., 2018; Golestani et al., 2017; Golestani, Kwinta, et al., 2016; Makedonov, Black, & Macintosh, 2013; K. A. Tsvetanov et al., 2015). However, if such factors influence both metrics in the same way then this may potentially enhance the correspondence between the two though not necessarily due to CVR (K. A. Tsvetanov et al., 2015; Kamen A. Tsvetanov et al., 2020). In particular, we were concerned that the correspondence between our two metrics might be affected by tissue-specific physiological factors such as whole-brain, global signals, cerebrospinal fluid pulsation, etc. However, we found that explicit removal of tissue-based signal components did not alter our results or conclusions. Importantly, the inclusion of additional (neuronal and/or physiological) signal components in a CVR metric does not necessarily invalidate its use as an indicator of compromised hemodynamics. Indeed, for the purpose of assessing fMRI activation integrity in the clinical context of surgical guidance, a qualitative rather than fully quantitative measure of CVR can be sufficient (Pillai & Mikulis, 2014).

We were also concerned that both breath-hold and resting-state patterns reflect a significant amount of random noise which will necessarily reduce the maximum obtainable spatial correspondence. To quantitatively assess this latter noise factor, we estimated the maximum attainable concordance by comparing two independent samples of breath-hold CVR data with each

other. Similarly, we also compared two independent samples of resting-state CVRe data. For a sample of 5 of our original subjects, the resulting mean correspondence accuracies were 64% for breath-hold CVR and 80% for resting-state CVRe while the mean cross-metric correspondence accuracy was 71.4% (see Appendix B). The lower self-concordance of the breath-hold metric may reflect patient variation in task performance (Bright & Murphy, 2013) and the artifactual effects of head motion which typically accompany an active breath-hold task. This may also be the primary factor limiting accuracy in the cross-metric correspondence.

Another consideration was that the lower self-correspondence of the breath-hold data might reflect a lack of sufficient sensitivity to detect all of the valid responses. In principle, this could occur if the breath-hold respiratory response is temporally unique for each person. Indeed, there is evidence that breath-holding induces BOLD changes that are relatively slower than for free breathing at rest (Birn et al., 2008). To circumvent this concern, we separately measured the respiratory response waveform for each individual subject and used it as a template for detecting each subject's breath-hold CVR signals throughout the brain. We even tested each subject's personalized respiratory response waveform with a range of delays to ensure maximum sensitivity for each voxel.

Although the primary focus of the present study was to compare two popular breath-hold CVR and resting-state CVRe metrics having clinical potential, we stress that they do not necessarily represent the best or most accurate measures of CVR that have been, or could be, devised. Indeed, these two metrics, as used in common practice, provide a qualitative rather than precisely quantitative test of cerebrovascular reactivity. Yet, for clinical use as a marker of potential fMRI "dropout" in presurgical brain maps, this can be sufficient. Fortunately, the path to a more quantitative and potentially informative metric is being actively pursued. Passive arterial

CO_2 and/or respiratory-volume signals can provide a more quantitative estimate of CVR from resting-state data (Birn et al., 2006; Golestani, Wei, et al., 2016; Jahanian et al., 2017). A number of recent studies have also explored latency maps computed from resting-state data in healthy controls and patients with cerebrovascular disorders (Amemiya et al., 2014; Aso, Jiang, Urayama, & Fukuyama, 2017; Christen et al., 2015; Khalil et al., 2017; Ni et al., 2017; Y. Tong et al., 2017). Such latency maps are thought to reflect both the arrival of cerebral blood flow and the reaction time of vasculature to changes in blood CO_2 (De Vis et al., 2018), thus providing alternate metrics of blood perfusion and vascular reactivity.

From the standpoint of clinical utility, it is important to note that the significantly better, more specific, coverage of gray matter by the resting-state CVRe metric may offer some modest advantage over the breath-hold technique as a biomarker for testing fMRI activation integrity. The use of resting-state has the advantage of not requiring a separate breath-hold task. Moreover, as the resting-state fMRI technique becomes more widely accepted as an alternative to conventional task-based fMRI for brain mapping, both functional and CVR maps can be derived from the same resting-state dataset. Since an important long-term goal is to use these metrics clinically for detecting potential NVU in patients facing invasive brain surgery, the results of this study provide a strong base for more extensive clinical tests with patients having a variety of operable brain pathologies. Such clinical studies will be needed to verify that both breath-hold CVR and resting-state CVRe metrics are able to reliably detect NVU in patients with ongoing brain pathology.

Conclusions

Our quantitative comparison suggests that breath-hold CVR and resting-state ALFF maps are spatially similar, but not identical at a voxel level of resolution. Their mutual correspondence as well as their accurate association with cerebral gray matter are critically dependent on the threshold settings chosen to identify valid CVR-responsive voxels and this must be considered when interpreting CVR brain maps. The resting-state pattern appears to segregate more accurately relative to gray versus white matter and has more complete coverage of gray matter than the breath-hold pattern. Additionally, the higher correspondence between two independent samples of the resting-state maps compared to two samples of the breath-hold maps suggests that the resting-state CVRe metric may be a modestly more reliable biomarker while also avoiding the need for consistent task performance with potentially compromised clinical patients. It should be noted that both metrics provide incomplete and variable labeling of gray matter at the resolution of individual voxels. Previous reports of reliable detection of CVR loss in clinical patients typically have used subjective threshold settings and high levels of spatial smoothing that obscure this variability, resulting in an unknown loss of sensitivity for detecting small, yet potentially significant CVR anomalies.

III. Spatial Sampling Statistics of Resting-State Vs. Breath-hold CVR Holes

Introduction

Ever since the approval of current-procedural terminology (CPT) codes in 2007, task-based functional Magnetic Resonance Imaging (fMRI) using Blood Oxygenation Level Dependent (BOLD) contrast has been employed in presurgical brain mapping of patients with focal brain pathology (e.g., tumors) (Baig et al., 2016; Barone et al., 2014; Hart et al., 2007; Jenkinson et al., 2018; Wengenroth et al., 2011). However, despite increasingly evident advantages, this technique is not routinely used for image-guided neurosurgical planning due to concern over the quality of BOLD fMRI signals (S. Agarwal, Sair, & Pillai, 2021; Holodny et al., 2000; Para et al., 2017; Silva et al., 2018; Ulmer, Hacein-Bey, et al., 2004). The concern arises from the fact that the BOLD response is not a direct measure of neural activity and derived from a complex cascade of events between neurons and nearby microvasculature (Attwell et al., 2010; S. Ogawa, T.M. Lee, A.R. Kay, & D.W. Tank, 1990). In situations wherein a focal abnormality can selectively disrupt this neuro-vascular coupling cascade, task-induced changes in neuronal activity cannot lead to regional hemodynamic responses and therefore, no changes in the relative ratio of blood oxygenated to deoxygenated hemoglobin occurs within imaging voxels. The consequential lack of BOLD responses due to such neuro-vascular uncoupling (NVU) will then appear as activation dropouts in functionally intact brain areas (Pillai & Zaca, 2011; Pineiro, Pendlebury, Johansen-Berg, & Matthews, 2002; Ulmer et al., 2004; Ulmer et al., 2003; Zaca, Hua, & Pillai, 2011; Zaca, Jovicich, Nadar, Voyvodic, & Pillai, 2014; Zaca & Pillai, 2012). Such false negatives can potentially

confound the interpretation of activation maps within functionally important brain areas (a.k.a. eloquent areas), leading to inadvertent surgical damage (DeYoe et al., 2015; Pillai & Mikulis, 2014; Ulmer et al., 2004). Therefore, for successful integration of BOLD fMRI brain mapping into the surgical plan, it becomes a matter of great importance to enable testing for fMRI activation integrity against NVU (Para et al., 2017).

As acknowledged by the American Society of Functional Neuro-Radiology (ASFNR) in 2014, cerebrovascular reactivity (CVR) mapping can be of benefit for detecting potential sites of NVU on task-based BOLD fMRI activation maps (J. Jean Chen & Gauthier, 2021; Mikulis, 2013; Pak et al., 2017; Peacock et al., 2016; Pillai & Mikulis, 2014; C. H. B. van Niftrik et al., 2019; Zaca et al., 2011; Zaca et al., 2014; Zaca & Pillai, 2012). For this purpose, CVR maps are achieved from BOLD responses to changes in the blood level of carbon dioxide (CO_2), either actively triggered by a breath-hold challenge (Bright & Murphy, 2013; Murphy et al., 2011; Peacock et al., 2016; Pillai & Mikulis, 2014; Tancredi & Hoge, 2013; Urback et al., 2017) or passively caused during a resting-state scan (Birn et al., 2006; B. B. Biswal et al., 2007; Golestani et al., 2015; Golestani, Kwinta, et al., 2016; Golestani, Wei, et al., 2016; Jahanian et al., 2017; Kannurpatti & Biswal, 2008; Kannurpatti et al., 2014; Lipp et al., 2015; Liu et al., 2017; Liu et al., 2021; Liu et al., 2020; Wise et al., 2004). Elevations in blood CO_2 by either cued or free breathing result in a brain-wide vasodilation, thereby increasing the cerebral blood flow, which can be detected by BOLD contrast fMRI (Birn et al., 2006; J. J. Chen, 2018). A labeled area on CVR maps is used as an imaging marker for healthy vascular reactivity, indicating the ability of regional vasculature to increase blood flow, potentially in response to neuronal activity (Liu et al., 2019). Hence, a locally compromised-CVR patch in accordance with task-based activation dropouts can potentially

specify a site of NVU, where caution must be taken during surgical treatments (J. Jean Chen & Gauthier, 2021; Pillai & Mikulis, 2014; C. H. B. van Niftrik et al., 2019; Zaca et al., 2014).

To assess the vascular response integrity using brain-wide maps of CVR, one would expect that the pattern of labeled areas should predominantly be confined to highly vascularized gray matter (as opposed to relatively poorly vascularized white matter) (Thomas et al., 2014b). Indeed, it was quite common in previous research that brain areas within the gray matter were defined as regions of interest and/or CVR thresholding was adjusted for maximal coverage of gray matter areas (S. Agarwal et al., 2017; Zaca et al., 2014). Nevertheless, neither breath-hold nor resting-state CVR maps, while being adjusted for optimum coverage of gray vs. white matter, completely label all regions of cerebral gray matter in healthy individuals (Catchlove et al., 2018; Kastrup, Li, et al., 1999; Hanzhang Lu et al., 2014; Peacock et al., 2016). The discontinuous nature of CVR maps raises concern about their ability to differentiate an NVU-related compromised patch from random signal losses. Certainly, lack of knowledge about the size of clinical NVU, and/or its probability of occurrence under different conditions, adds even more difficulties in using CVR maps to identify whether a hole on task-based fMRI activation is potentially indicative of NVU. Consequently, if CVR maps are to be effective in testing the integrity of clinical fMRI activation against NVU, it is required to closely examine their capacity in revealing the foci of impaired vascular response in healthy individuals as a baseline. Given that a hole on a CVR map can only be identified as potential NVU if its spatial size is statistically unlikely in healthy individuals, the primary goals of this study were to (1) assess the spatial sampling statistics of different-size holes on CVR maps in healthy individuals and (2) determine whether the sensitivity of resting-state CVR spatial patterns in detecting potential NVU is statistically equivalent to that of breath-hold CVR.

Since both breath-hold and resting-state metrics are thought to be driven by breathing-induced fluctuations in blood CO_2 (Birn et al., 2006; Golestani, Wei, et al., 2016), we tested the prediction that the likelihood of observing different-size holes in resting-state CVR maps is equivalent to that of breath-hold CVR maps. Another prediction would be that CVR maps in healthy individuals should only contain relatively small-size holes indicative of random signal losses. Hence, we tested whether the occurrence of large holes in cerebral gray matter of healthy individuals is statistically rare using either breath-hold or resting-state metrics of CVR.

Materials and Methods

Participants

Nine healthy young adults, with no history of neurological disease, participated in this study (5 females and 4 males; mean age of 26.5 years, range: 23 – 35). Prior to data collection, all experimental procedures were approved by the Institutional Review Board of the Medical College of Wisconsin (protocol PRO00020109). For each participant, a written and informed consent was collected during an interview at the time of first enrollment in the study. The consent forms explained the nature of study and potential risks to participants.

Experimental Scans

All MRI scans were performed in one session and explained to participants prior to entering the scanner room. Participants were also reminded of each scan/task verbally prior to imaging. Each participant was first required to complete T1-weighted anatomical scans followed by

performing resting-state scans and then breath-hold scans, always in the same order, as described below.

Resting-state

We acquired resting-state fMRI images for all participants while they breathed normally and kept their eyes open and fixated on a small cross at the middle of the screen during a 10-minute interval. The resting-state data acquisition was accomplished with an additional 4 sec equilibration period at the beginning of the scan for a total scan time of 604 s (302 image volumes). The resting-state scans were repeated twice for all participants, except for one person who only performed a 7-minute resting-state task with an initial 8 sec equilibration period for a total scan time of 428 s (214 image volumes).

Breath-hold

Based on previous research (Pillai & Mikulis, 2014), we modeled the breath-hold task as a block-design paradigm with 4 epochs of breathing-inhalation-holding periods; each epoch involved a 40 sec normal breathing, 4 sec inspiration, and 16 sec breath-hold interval, respectively. A 20 sec interval of normal breathing was also added at the end of the fourth epoch (Fig. 2.1C). To ensure consistent performance among all participants, we supplied visual text stimuli ("normal breathing," "inhalation," "breath-hold") to cue participants for different phases of the breath-hold task during the scan. The presentation of visual text stimuli was via an LCD video projector onto a back-projection screen viewed by the subject through a mirror system mounted on the head coil of the MRI system. The breath-hold task was repeated two times with an additional 4 sec equilibration period at the beginning of each run. As a result, a total of 132 image volumes (264 s) was collected for each participant per run. For all individuals, in addition to verbal explanation, the breath-hold task was practiced with each participant in a training session prior to scanning.

MRI Acquisition Parameters

All images were acquired using a 3 Tesla General Electric Signa Excite 750 MRI scanner (GE Healthcare, Wisconsin, USA), with a custom 32-channel RF/gradient head coil. BOLD fMRI scans were obtained using a T2*-weighted gradient echo, echo-planar imaging (GRE-EPI) pulse sequence with the following parameters: TR = 2000 ms, TE = 30 ms, flip angle = 77°, field of view = 240 mm, matrix size = 96 × 96, and a slice thickness of 5mm). These parameters resulted in raw voxel size of 2.5 × 2.5 × 5 mm, which was Fourier interpolated to 1.875×1.875× 5 mm. As described above, we used a 4 or 8 sec. equilibration period for each functional MRI scan to allow for magnetization transients. During the functional scans, participants were instructed to remain relaxed and breathe normally with their eyes open and fixed on a central marker on the video display. T1-weighted anatomical images were collected using a spoiled, gradient recalled (SPGR) pulse sequence with the following parameters: TR = 8.2 ms, TE = 3.2 ms, flip angle = 12°, field of view = 240 mm, matrix size = 256 × 224, and 180 axial slices with a slice thickness of 1 mm). For all participants, image collection was performed within a single imaging session. In order to provide an independent measure of potential data quality, we also assessed the alertness level of each subject after each run by asking them to rate their alertness on a scale from 1 – 5, with 1 representing “highly drowsy” and 5 referring to “full awareness.” For all participants, real-time respiratory bellows data were collected to further assess the quality of task performance.

Analysis Software

All images were processed using the AFNI/SUMA (http://afni.nimh.nih.gov/afni, version 19.3.11) (Cox, 1996) software packages. FSL (https://fsl.fmrib.ox.ac.uk, version: 6.0.2) together with Prism View® (RRID:SCR_016977; http://www.prismclinical.com) were used to create volumes of interest for each subject. Using the 'recon-all' function in the Freesurfer (http://surfer.nmr.mgh.harvard.edu, version 6.0.0) software package, the pial and white matter surfaces were also created for each subject from their high-resolution T1-weighted images. The optimization of threshold settings for mapping both breath-hold and resting-state CVR activation was accomplished using a custom MATLAB program (R2017a). Constructing the probability distribution of different-size holes and additional statistical analyses were performed using Microsoft Excel 2016 and MATLAB (R2017a).

Preprocessing

The details on data pre-processing are described in Chapter II. In short, the reconstructed datasets were pre-processed using a script generated by AFNI's *afni.proc.py* in the following order: (1) The equilibration period was removed from all datasets (AFNI's 3dTcat). The timeseries of each breath-hold dataset was truncated to 100 image volumes (200 s). For each resting-state dataset, the timeseries was limited to the first 210 image volumes (420 s, equivalent to a 7 min scan). (2) The successive images of each functional timeseries were co-registered (AFNI's 3dvolreg) and then cross-registered to the skull-stripped anatomical images (AFNI's align_epi_anat.py). The alignment process was performed in a single step by combining the matrices computed from the rigid body and volume registration transformations (AFNI's 3dAllineate). (3) Spatial smoothing using an isotropic gaussian filter kernel with full width at half maximum (FWHM) size of 4mm was applied on functional data (AFNI's 3dMerge). (4) Each

voxel's timeseries was scaled to a range of 0-200 with a mean of 100. (5) The linear trend was removed from the scaled timeseries. The derivatives of head motion signals (the motion magnitude at each time point) as computed by AFNI's 3dvolreg in step 2 were employed as motion regressors in a linear regression analysis (AFNI's 3dDeconvolve). The resulting regression matrix was then projected out of the timeseries data (AFNI's 3dTproject) to yield the final cleaned signals.

Volumes of Interest

T1-weighted anatomical images were brain-masked (AFNI's 3dSkullStrip) after being corrected for nonuniformity (AFNI's 3dUnifize). Each skull-stripped anatomical dataset was segmented into three different tissue classes: gray matter, white matter, and cerebrospinal fluid (FSL's FAST segmentation tool) (https://fsl.fmrib.ox.ac.uk, version: 6.0.2, RRID:SCR_002823) (Y. Zhang et al., 2001). A whole-brain gray+white matter volume was then created. Separately, a mask of non-cortical structures was manually created using Prism View® software (http://www.prismclinical.com, RRID:SCR_016977) together with the standard MNI ICBM152 template (http://en.wikibooks.org/wiki/MINC/Atlases, RRID:SCR_005281) (Mazziotta et al., 1995). The mask was then used for the exclusion of unwanted non-cortical structures from the whole-brain gray+white matter volume, yielding a volume consisting of only the cortical gray matter and white matter (GWM-VOI). Ultimately, by excluding the white matter volume, a volume consisting only of cortical gray matter was created (GM-VOI).

Data Analysis

Data analysis was performed in two major steps: (Step 1) For each subject, we first obtained the spatial patterns of breath-hold and resting-state metrics while maximizing inclusion of areas in cortical gray matter with minimum encroachment into the white matter. (Step 2) We then computed the frequency of different-size holes in the resulting spatial patterns to estimate the average likelihood that each size of hole could occur in healthy subjects.

Step1. Optimized Maps of Resting-State and Breath-Hold Metrics: Creating optimized maps of resting-state and breath-hold metrics is discussed in detail in Chapter II. A brief description is as follows: we first computed the resting-state and breath-hold metrics of CVR for each subject. The resting-state fMRI measure of amplitude of low frequency fluctuations (ALFF) was obtained by calculating the power of each voxel's timeseries within the low-frequency range of 0.01 – 0.08 Hz (AFNI's 3dRSFC) (Zang et al., 2007). We will refer to the ALFF metric as the resting-state "CVRe" metric, where the "e" implies "estimate." To compute a breath-hold CVR metric for each voxel, we first acquired an accurate estimate of the subject's unique respiratory response waveform (AFNI's 3ddelay). The waveform was then used in a series of regression analyses (with multiple time lags from 0 – 4 TR) against the original empirical breath-hold timeseries (AFNI's 3dDeconvolve). This resulted in 5 waveform-fit (beta) coefficients for each voxel; one for each time delay. Essentially, each beta coefficient was a measure of the amplitude of the fitted waveform. Ultimately, for each voxel, we obtained the time lag that yielded the best fit of its timeseries to the subject's respiratory response waveform. The beta coefficient corresponding to the voxel's optimal time lag was then used as that voxel's breath-hold CVR metric.

Having computed the resting-state and breath-hold metrics for each voxel, we then produced optimized maps of these metrics by maximizing coverage of gray matter while simultaneously minimizing labeling of white matter. The optimization was accomplished by

exploring a wide range of threshold settings for each metric. For each threshold setting, voxels were first classified based on their CVR status (presence = 1 or absence = 0) and whether they were within gray matter (=1) or not (= 0), thereby assigning one of the four binary combinations of 11, 00, 10, or 01 to each voxel. We then computed the accuracy of CVR/gray matter overlap for each threshold setting. This allowed us to identify the threshold setting that yielded maximum overlap accuracy. Ultimately, all CVR-present voxels within the GM-VOI were mapped using the optimal threshold settings (Fig. 3.1).

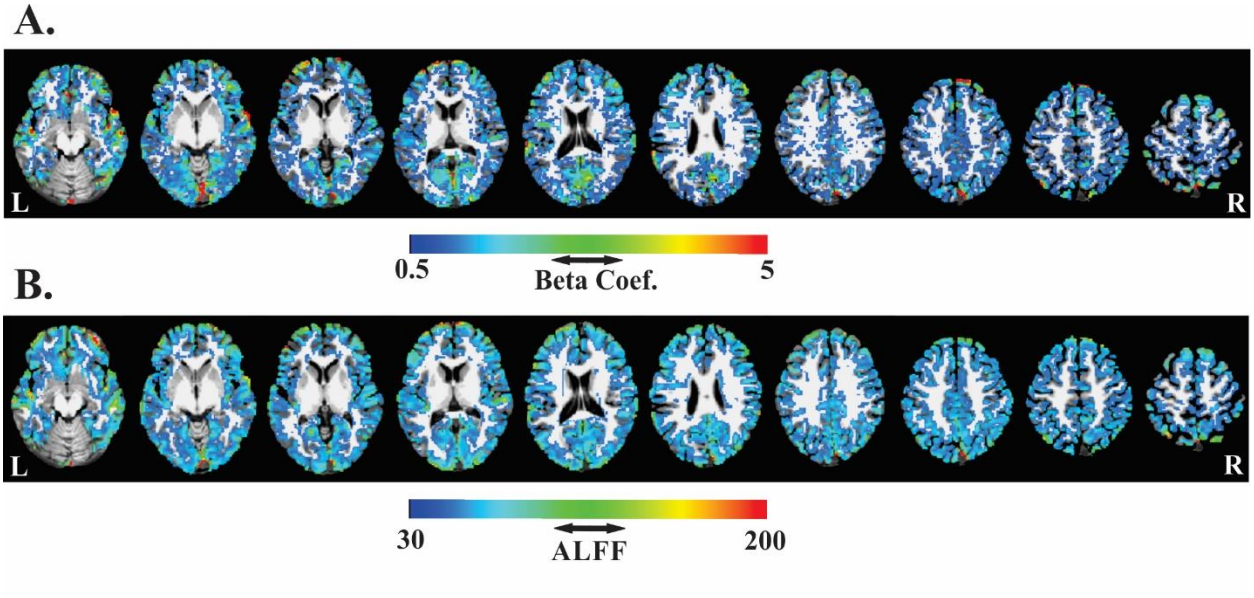

Figure 3.1. Optimized breath-hold CVR **(A)** and resting-state CVRe **(B)** spatial patterns masked to cortical gray+white matter overlaid with axial T1-weigthed images for a representative subject. Optimal threshold settings for breath-hold metric (Beta Coef.) and resting state metric (ALFF) were 0.5 and 30, respectively. **R:** right; **L:** left; **Coef.:** coefficient.

Step 2. Computing The Average Likelihood of Different-Size Holes on CVR Maps: For each subject, the brain maps of the resting-state and breath-hold metrics were separately thresholded and then logically inverted to yield binary maps of CVR holes (Fig. 3.2A and 3.2B). These maps were then projected onto cortical surface models (AFNI's 3dVol2Surf), and nodes belonging to

each CVR hole were grouped together to generate different-size clusters (AFNI's SurfClust) (Fig. 3.2C and 3.2D). The connectivity parameter for node-level clustering was defined based on a maximum distance of 2 edges between neighboring nodes. The identified clusters were sorted by size and a rank was assigned to each cluster. Surface-based datasets were then created so that the value at each node was set to be the ranking of the cluster to which they belong. The resulting clustered datasets were then mapped onto the volumetric domain (AFNI's 3dSurf2Vol), and the number of voxels in each cluster (cluster size) was obtained. Finally, the number of occurrences of each cluster size and the total number of clusters were calculated and used to determine the probability that a given cluster (hole) size is observed in an individual's CVR maps relative to all holes:

$$\text{Probability}_{(\text{cluster size n relative to all clusters})} = \frac{\text{Frequency of cluster size n}}{\text{Total number of clusters}} \qquad \text{(Equation 3.1)}$$

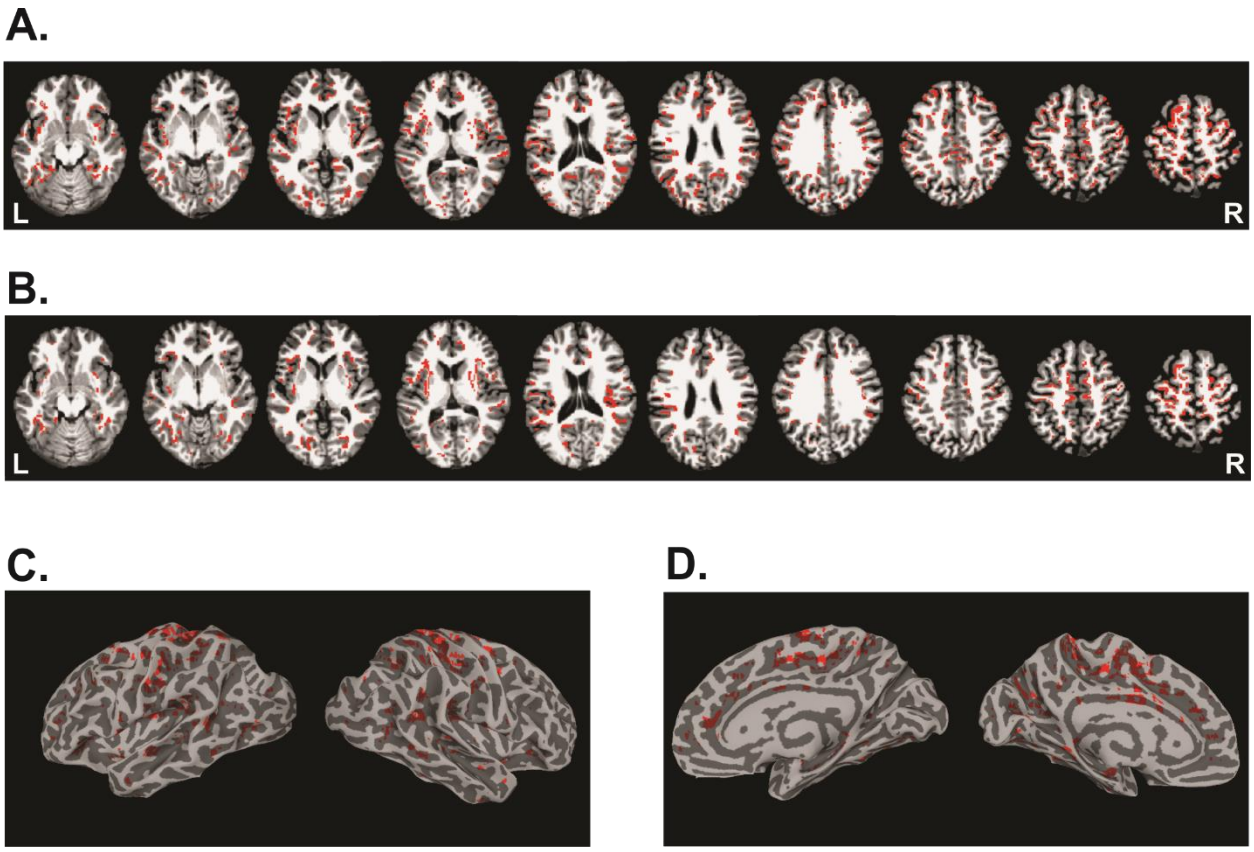

Figure 3.2. Breath-hold CVR holes **(A)** and resting-state CVRe holes **(B)** overlaid with the axial T1-weigthed images confined to cortical gray matter for a representative subject. Breath-hold CVR **(C)** and resting-state CVRe **(D)** holes mapped on surfaces for the same subject, respectively. **R:** right; **L:** left.

Finally, by computing the average probability that each size of holes could occur in our sample of nine healthy subjects, the probability distribution of different-size holes in CVR maps was formed as a function of the cluster size (volume). Figure 3.3 depicts a schematic diagram summarizing our data analysis methodology.

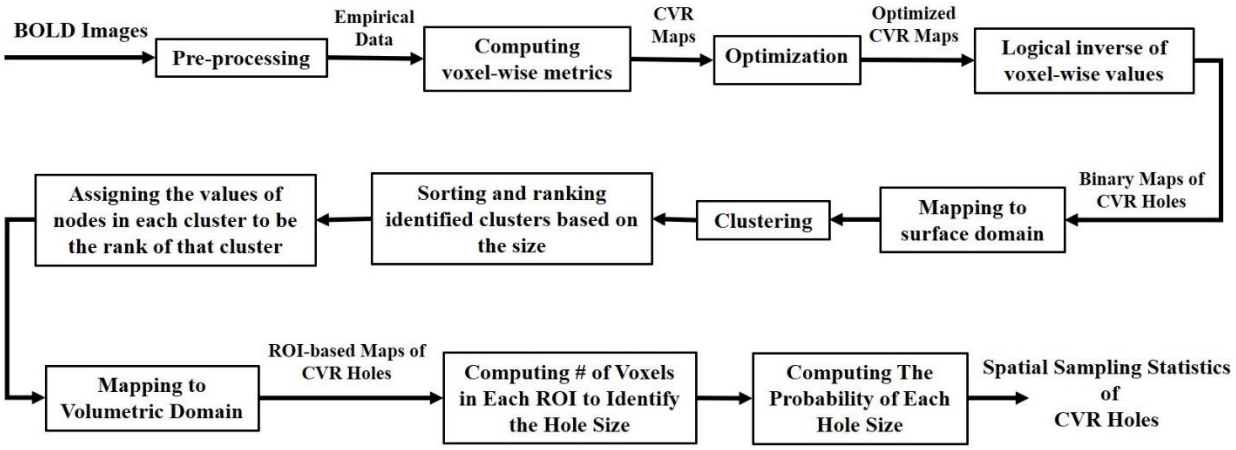

Figure 3.3. Schematic Diagram of Data Analysis.

Statistical Analysis

In this study, all parametric values are reported in the format of average ± standard error. To test if the likelihood of observing different-size holes in breath-hold CVR maps is equivalent to that of resting-state CVR maps, we sought to determine whether there was a significant difference in the probability distributions of breath-hold CVR versus resting-state CVRe holes. This was accomplished by performing a two-way, repeated measures ANOVA with cluster size and CVR metric as main factors. This allowed us to statistically compare average probabilities associated with different-size clusters for the two CVR metrics. A *P*-value of 0.05 was considered significant.

The second objective of this study was to test whether the occurrence of large holes in cerebral gray matter of healthy individuals is statistically rare using either breath-hold or resting-state metrics of CVR. For this purpose, with the assumption that the mean probability distribution of our sample is representative of the healthy population, we sought to identify the minimum size

of a hole that is unlikely to be observed in an individual by chance. For each metric, this was performed by specifying a hole volume at which the average probabilities would add up to 95% (i.e., p-value < 0.05). The identified hole volume was appointed as a threshold on the cluster size from which any larger hole would have an incidence chance of less than 5%.

Results

Figure 3.4 demonstrates the mean probability distribution of different-size holes on the resting-state and breath-hold CVR maps for our sample of nine healthy individuals.

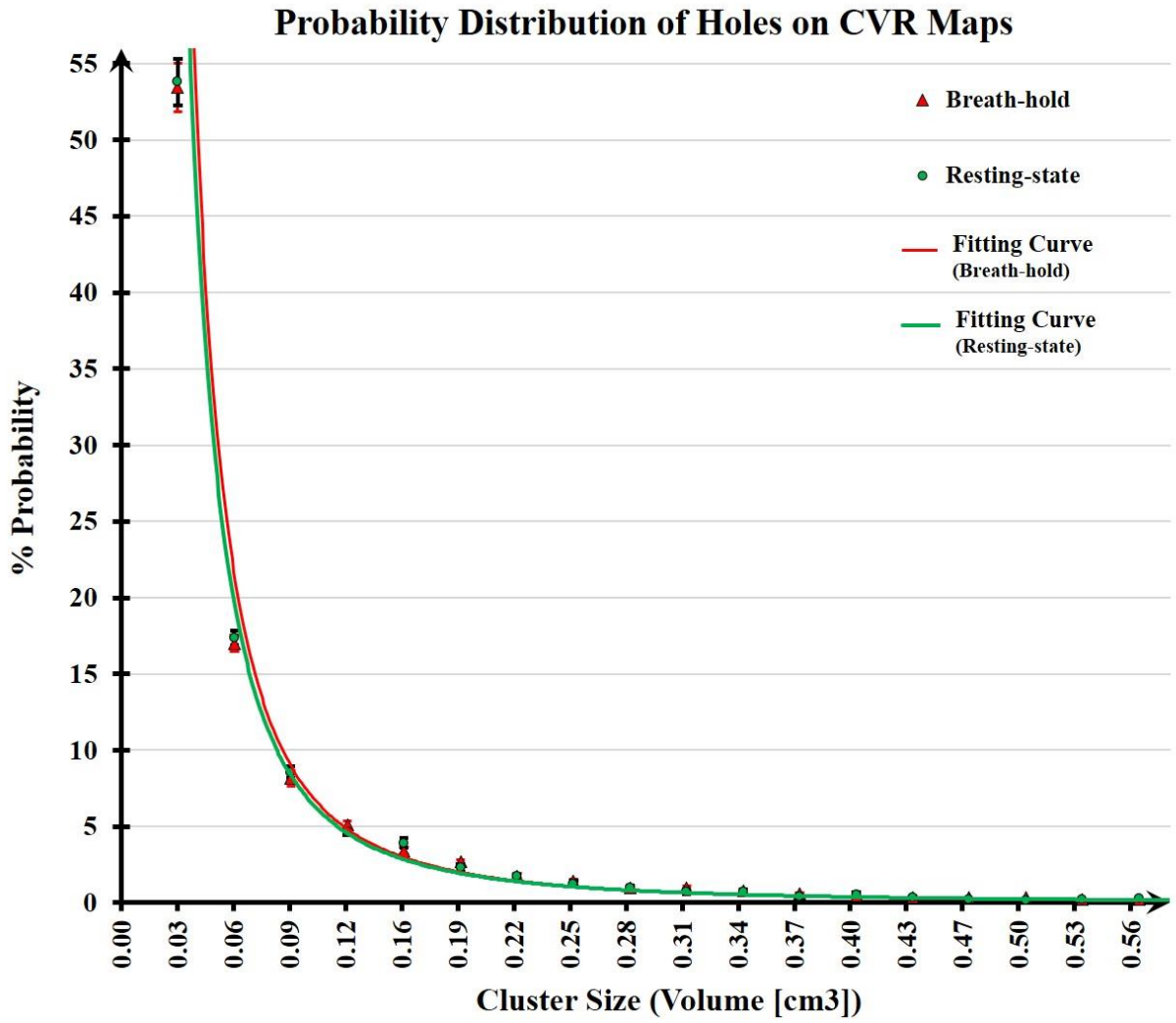

Figure 3.4. The probability distribution of CVR holes for resting-state (green) and breath-hold (red) as a function of cluster volume for a sample of 9 healthy individuals.

As illustrated in Figure 3.4., the average probability that a CVR hole could occur in healthy individuals declined dramatically as cluster size increased. The best-fitting curve to the breath-hold data points was modeled as a decaying power function $Y = 0.054X^{-2.161}$, wherein Y and X are the estimated values of the probability and the cluster size, respectively. The accuracy of fit was 94% ($R^2 = 0.94$). Similarly, the curve of best fit to the resting-state data points was modeled as $Y = 0.056X^{-2.112}$, which explains 97% of the data variations ($R^2 = 0.97$).

In Figure 3.4., the two distributions seem to entirely overlap to each other. Consistent with our observation, a two-way repeated measures ANOVA (Resting-state/Breath-hold CVR × cluster size distribution) revealed no statistically significant differences between the mean probability distributions of resting-state and breath-hold CVR holes ($p < 0.05$). As demonstrated in Figure 3.5, there was a minimum hole size for each metric at which the cumulative sum of hole probabilities exceeded 95%. The identified hole size was identical for both metrics and was equivalent to a CVR hole of 0.31 cm^3 (i.e. nearly 10 voxels).

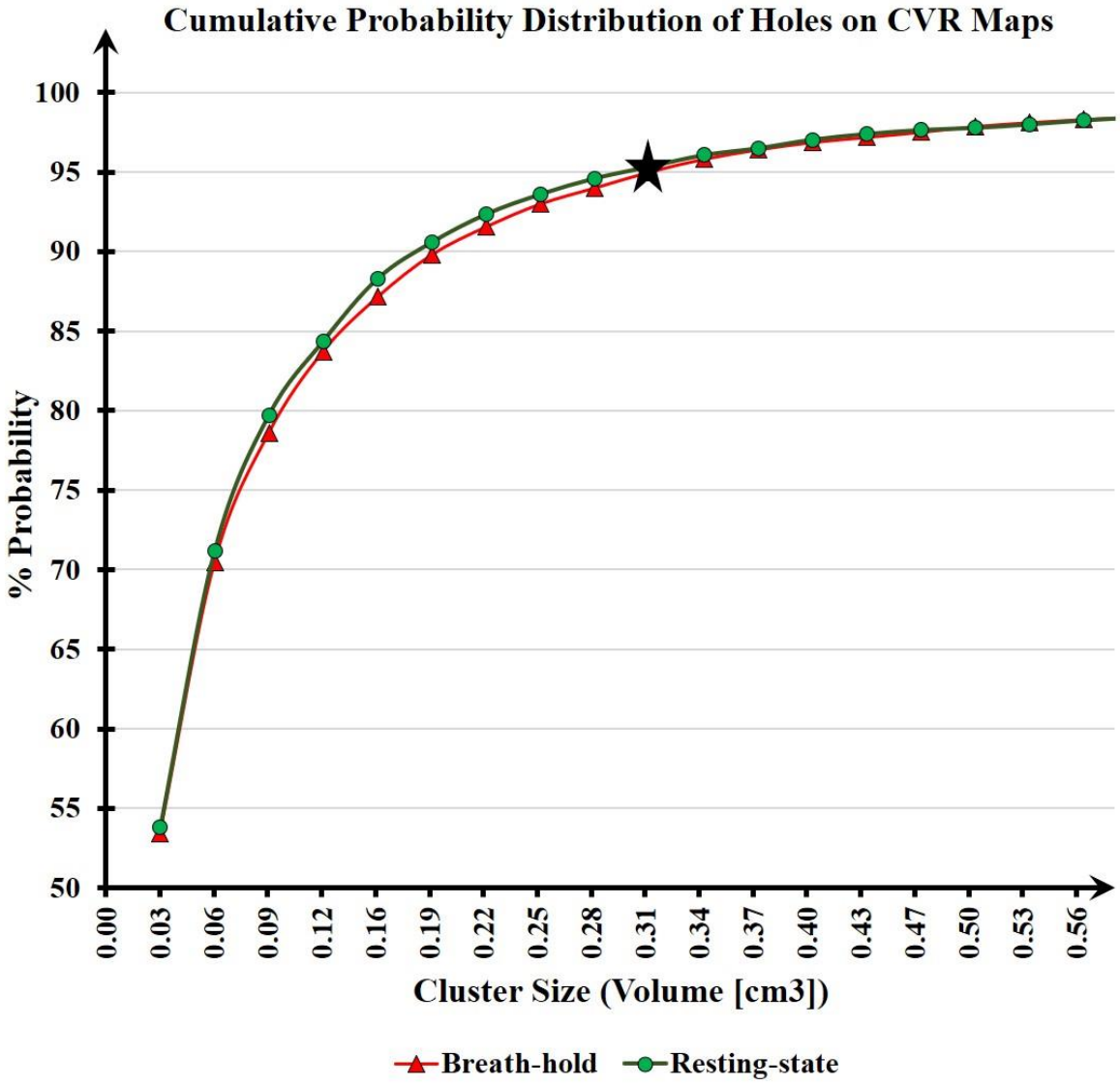

Figure 3.5. Cumulative probability distributions of resting-state CVRe holes (green) vs. breath-hold CVR holes (red). The black star indicates the threshold (.31 cm^3) at which any larger holes would have less than 5% chance of occurrence.

As a further cross-check on our methods, we also assessed the probability distribution of CVR holes for a different sample of healthy individuals. For this purpose, we performed the same analyses on an independent sample of nine healthy control subjects from the Epilepsy Connectome

Project (ECP), a National Institutes of Health-sponsored project jointly managed by the Medical College of Wisconsin (MCW) and the University of Wisconsin-Madison (UW).

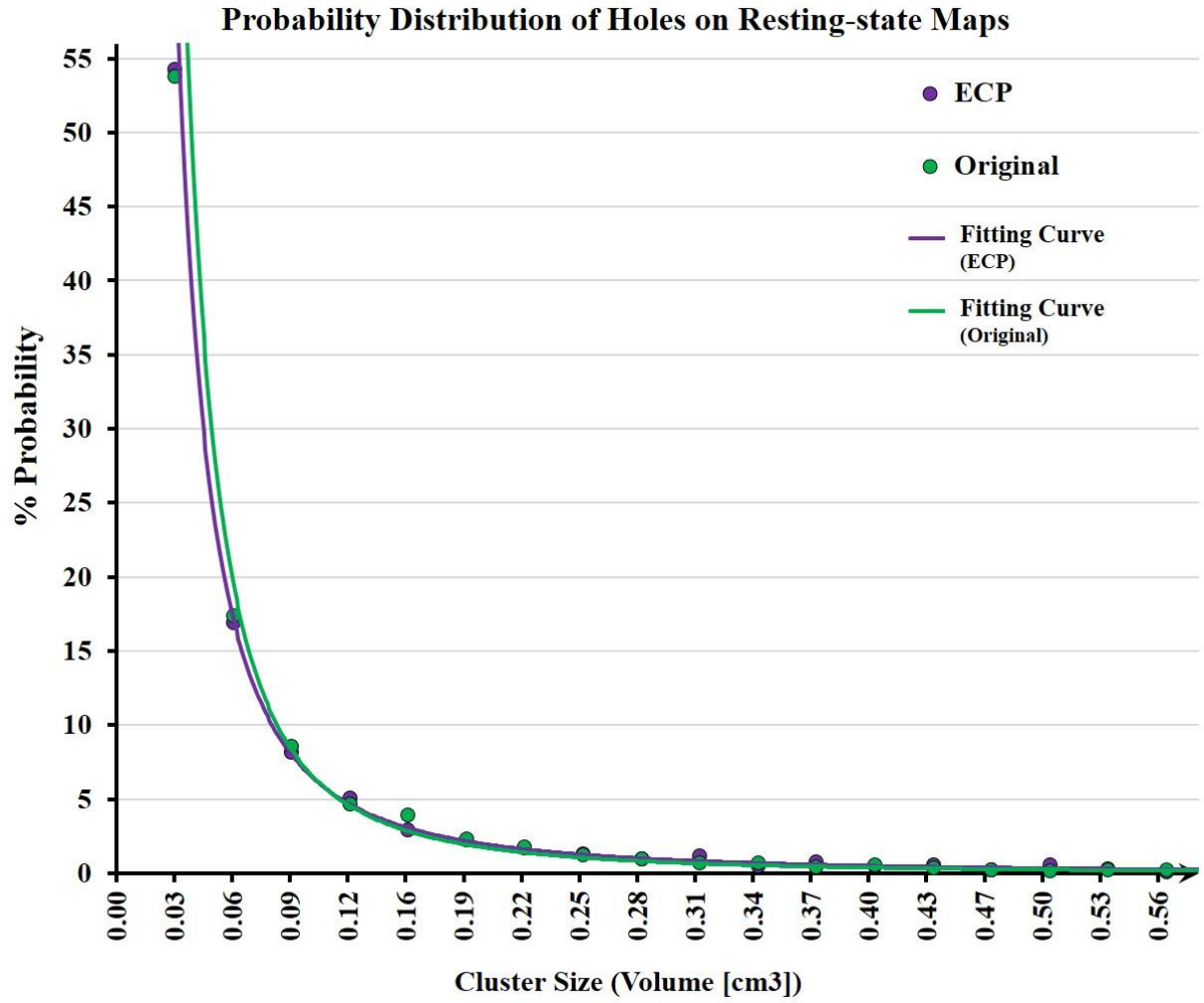

Figure 3.6. The probability distribution of CVRe holes on resting-state maps of nine ECP controls (purple) vs. our nine healthy individuals (green).

The results of statistical analysis [(two-way repeated measures ANOVA (ECP/Original CVR × cluster size distribution), ($p < 0.01$)] did not reveal any significant difference in the

probability distribution of holes between ECP and our original resting-state data (Fig. 3.6). In the ECP data, the minimum hole volume with a maximum incidence risk of 5% was 0.37 cm^3 (i.e. nearly 12 voxels) (Fig 3.7).

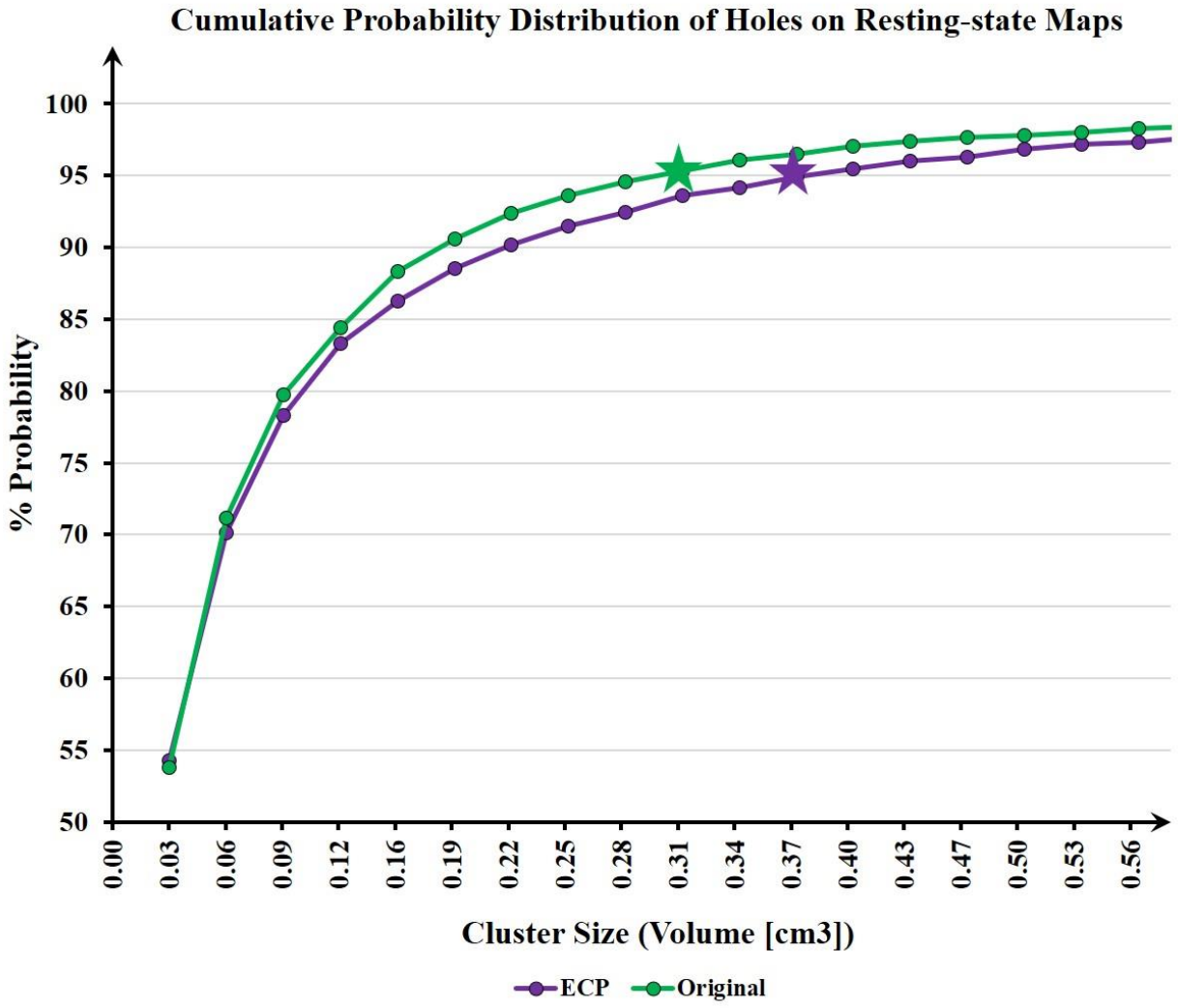

Figure 3.7. Cumulative probability distributions of CVR holes in ECP (purple) vs. our original (green) resting-state maps. Thresholds on hole volumes were 0.31 and 0.37 cm^3 for original (green state) and ECP (purple star) data, respectively.

Discussion

In this study, we investigated the capacity of BOLD CVR maps derived from breath holding and resting-state free breathing to reveal foci of impaired vasoreactivity. This was accomplished by first optimizing each CVR map for maximum coverage of highly vascularized gray matter, and then computing the probability that a CVR hole in a given size could occur due to random signal variation. Having achieved the spatial sampling statistics of CVR holes in this manner, we also determined quantitatively how unlikely it would be for a relatively large CVR hole to occur by chance for each metric.

The main findings of this study are: (1) For both resting-state and breath-hold metrics, the probability distribution of BOLD-CVR holes rapidly decline as the size (volume) of holes increases. (2) In healthy adults, the spatial sampling statistics of different-size holes on CVR maps derived from resting-state data are comparable to those derived from breath-hold data. (3) CVR holes with a volume larger than 0.31 cm^3 on either resting-state or breath-hold maps has less than 5% risk of occurring by chance. These findings were consistently obtained for all participants.

Overall, the results of this study provided sufficient evidence to conclude that the likelihood of observing different-size holes in breath-hold CVR maps is equivalent to that in resting-state CVRe maps. Our prediction was based on the premise that both breath-hold and resting-state metrics arise from breathing-induced blood CO_2 fluctuations. Our observation of comparable spatial sampling statistics of CVR holes between the two metrics was consistent with this scenario, suggesting that, perhaps, resting-state CVRe maps similarly reflect variations in CVR to blood CO_2 fluctuations as breath-hold CVR maps. Such a possibility was proposed by others based upon the significant spatial correlation obtained between the two maps of breath-hold

and resting-state based CVR measurements on a global scale (Birn et al., 2006; Jahanian et al., 2017; Lipp et al., 2015). These studies, however, failed to take into account the effect of random noise variation on labeling patterns of the two metrics throughout the brain.

The main objective of this study was to explore the spatial characteristics of CVR maps in terms of their continuity and uniformity to establish their usefulness for testing fMRI BOLD activation integrity. This was motivated by our initial perusal of CVR maps which revealed a patchy labeling pattern using either metrics after the optimization for maximum coverage of gray matter. In clinical settings, where CVR maps are typically thresholded to be mainly confined to gray matter areas, we feel that the sporadic feature of these maps may serve as an important caveat to previous clinical studies on the interpretation of absent-CVR patches as foci of CVR defects (S Agarwal, Sair, & Pillai, 2017; S. Agarwal et al., 2021; Nishida et al., 2018; Pak et al., 2017; Peacock et al., 2016; Pillai & Zaca, 2011; Zaca et al., 2011; Zaca et al., 2014). In the present study, we demonstrated how likely a certain-size hole could occur in CVR maps of healthy subjects due to random noise variations in order to determine the sensitivity of CVR maps to detect vascular dysfunction. This then provides a basis to statistically quantify the capability of these maps to interrogate the intactness of vasoreactivity. This approach opposed previous research that investigated quantitative CVR measurements at the voxel level and/or the spatial distribution of CVR responsive voxels in a global scale (De Vis et al., 2018; J. A. Fisher et al., 2018). For a methodological standpoint, this study is thus the first to treat the spatial characteristics of CVR maps from a statistical point of view, with a focus on the incidence risk of CVR holes.

Our exploration of the spatial sampling distribution of holes on CVR maps allowed us to specify a threshold of hole size from which any larger holes would be statistically unlikely to occur in healthy subjects. We showed that both resting-state and breath-hold metrics have an identical

threshold of 0.31 cm^3, wherein the risk for the hole to be a signal-loss area by chance alone is less than 5%. These results allow us to conclude that the occurrence of large holes in cerebral gray matter of healthy individuals is statistically rare using either breath-hold or resting-state metrics of CVR. Consistent with this prediction, we also showed that the extent to which the two metrics identify statistically unlikely large holes is equivalent. From the clinical standpoint, this suggests that both maps of CVR have the same capacity to indicate areas with impaired vasoreactivity. These results provide evidence in support of the premise that both metrics arise from ongoing changes in blood CO_2. Nevertheless, we stress that our objective was not to show that the two metrics exclusively reflect CVR alone. Indeed, it is quite possible that other factors rather than CVR-related physiological components could contribute to each metric. However, the results of this study implied that both metrics have similar contributions from CVR and/or similarly affected by other factors, thereby may equally be effective in being used clinically to characterize a site of compromised vasoreactivity.

Our results demonstrated that a standard limit for tradeoff decisions on the results of CVR testing can be assigned to be a hole volume of 0.31 cm^3 using either breath-hold or resting-state CVR metrics. Although there is no clinical information on the size of a pathology-related site of impaired vasoreactivity indicative of NVU, the determination of the threshold of 0.31 cm^3 on the hole size merits further considerations. Perhaps one of the most important considerations is that the optimization of labeling patterns for maximum coverage of gray matter may not necessarily reveal CVR with full potential. Indeed, the distribution of vasculature in gray matter is about 75% higher than adjacent white matter, which suggests that the CVR is predominantly, but not entirely, confined to gray matter (H. Lu et al., 2005; van Gelderen, de Zwart, & Duyn, 2008). Different areas of cortical gray matter may vary temporally and spatially in vascular reactivity to changes in

blood CO_2, which could also be the case between the gray and white matter areas (Liu et al., 2020; Thomas et al., 2014a). Moreover, from a methodological standpoint, our initial perusal of the data revealed that the voxel-based clustering in deep cortical folds was very likely to place small groups of absent-signal voxels in a large cluster. We minimized the effect of folded cortical cortex on clustering by mapping the CVR holes from the volume domain onto the surface domain. Afterwards, to avoid any biases on surface-based clustering, a maximum distance of two edges was used between neighboring nodes. Though, the mapping and clustering parameters may still cause neighboring small holes to artificially be combined together, thereby forming a relatively larger hole, which would, in turn, affect the probability distribution of holes to decrease with a lower slope as a function of the cluster size.

While the primary focus in this study was to compare the ability of two breath-hold and resting-state CVR metrics to test the integrity of vascular reactivity, our overall conclusions were also cross checked with a different sample of healthy individuals from the ECP. We showed that there is no statistically significant difference in spatial sampling statistics of resting-state CVRe holes between the two samples. The minimum hole volume with a maximum incidence risk of 5% for the ECP data was 0.37 cm^3. We speculate that the recruitment of different age and sex groups in the ECP study is likely to be the most important factor that has shifted the threshold on the cluster size (Miller et al., 2019).

Conclusions

A global test of CVR based on the breath holding approach has been widely accepted as an essential addition to presurgical fMRI brain mapping for detecting potential NVU. The present

study provided evidence suggesting that both breath-hold and resting-state maps are able to interrogate the intactness of cerebral vasoreactivity to the same extent. The likelihood of an absent-signal patch in a given size to occur by chance in healthy subjects is statistically comparable between the resting-state and breath-hold maps. In sum, the incidence risk of large holes in either resting-state or breath-hold CVR maps is statistically rare so that any hole larger than 0.31 cm^3 cannot have more than 5% risk of being indicative of signal losses by chance. Clinically, this potentially offers a standard threshold on the size of CVR holes for making tradeoff decisions on the results of CVR testing thereby identifying regions of likely NVU in patients. Additionally, our comparison between two different samples of individuals suggests that the voxel size and acquisition protocols do not significantly change the decision-making threshold on different hole sizes.

IV. Resting-State CVR Maps for Detecting Potential NVU in Clinical Task-fMRI Activation Maps

Introduction

In the surgical treatment of patients with focal brain pathology such as tumors, accurate assessment of the extent of safe removal of brain tissue is essential, particularly in areas that are functionally critical (a.k.a. eloquent cortex). This is because the surgery-related damage to these areas can result in neurological deficits which would, in turn, diminish the quality of life for patients (Laurent et al., 2019; Rahman et al., 2016). The task-based blood oxygenation level dependent (BOLD) functional magnetic resonance imaging (fMRI) technique has provided an opportunity for neurosurgeons to non-invasively interrogate the intactness of brain tissue, thereby identifying diseased areas that are safe for resection or radiation (Atlas et al., 1996; Baig et al., 2016; Barone et al., 2014; Holodny et al., 2000; Janecek et al., 2013; Jenkinson et al., 2018; Pillai & Zaca, 2012; Stummer et al., 2008). In this context, BOLD signals are not direct measures of neuronal activity but rather the effects of neuronal-mediated vasoreactivity on blood oxygenation as reflected by a change in the concentration of blood deoxygenated hemoglobin in imaging voxels during MRI (Attwell et al., 2010). Neuro-vascular coupling mechanisms underlying this function, however, are very likely to be disturbed under a variety of conditions, such as tumors, which could then result in compromised BOLD signals within functionally-intact brain regions (S. Agarwal et al., 2021; Jiang et al., 2010; Pak et al., 2017; Para et al., 2017; Pillai & Mikulis, 2014; Pillai & Zaca, 2011, 2012; Ulmer et al., 2003; Ulmer, Salvan, et al., 2004; Zaca et al., 2011; Zaca et al., 2014).

An obvious vulnerability when it comes to the possibility for a neuro-vascular interaction loss, referred to as neuro-vascular uncoupling (NVU), is the risk of false negatives on task-based fMRI activation (a.k.a. Type II Error) (S. Agarwal et al., 2021). While surgical interventions typically emphasize the avoidance of false negatives, it is of crucial importance to detect NVU-related task-fMRI activation dropouts to successfully integrate this technique into the surgical plan; otherwise, its use may come at the cost of irreparable damage resulting in unintended consequences for patients (Ulmer, Hacein-Bey, et al., 2004). For example, a neurosurgeon may erroneously relate believe a lack of BOLD fMRI responses to non-functional brain tissue that is safe for resection or radiation. Such misinterpretation of fMRI data may then lead to an overly aggressive therapy that removes as much abnormal tissue as possible, but also includes the unintended resection/radiation of enclosed eloquent tissue, thereby causing neurological deficits and a diminished quality of life for patients. The potential for such misinterpretation underestimates the effectiveness of fMRI brain mapping in image-guided neurosurgical planning (S. Agarwal et al., 2016; S. Agarwal et al., 2021; S. Agarwal, Sair, Yahyavi-Firouz-Abadi, Airan, & Pillai, 2015; Balthazar et al., 2014; DeYoe & Ulmer, 2005; DeYoe et al., 2014; DeYoe et al., 2015; Duarte et al., 2015; Holodny et al., 2000; Mazerolle et al., 2018; Mikulis, 2013; Pak et al., 2017; Para et al., 2017; Pillai & Mikulis, 2014; Pineiro et al., 2002; Silva et al., 2018; Ulmer, Hacein-Bey, et al., 2004; Ulmer et al., 2003; Watkins et al., 2014; Zaca et al., 2011).

Current efforts to detect NVU have been focused on testing cerebrovascular reactivity (CVR), an index of cerebrovascular reserve that refers to the ability of cerebral vessels to adjust their caliber in response to physiologic demands (Joseph A. Fisher & Mikulis, 2021; C. H. B. van Niftrik et al., 2019). Theoretically, NVU can ensue from the disturbance of physiological function at any point along the coupling cascade between neurons and cerebral vessels; however, evidence-

based clinical outcomes suggest that the occurrence of NVU, regardless of where it is initiated, will eventually result in locally impaired vasomotor function (Watkins et al., 2014). This demonstrates the paramount significance of a direct test of CVR for quality assessment of clinical task-based fMRI maps. It is imperative that a brain region with compromised CVR similar to an impaired task-fMRI activated area, is identified as a potential site of NVU, and caution must be taken for a reliable interpretation of functional data (De Vis et al., 2018; Pak et al., 2017 2017; Pillai & Mikulis, 2014; Pillai & Zaca, 2012; Zaca et al., 2011).

CVR mapping is typically achieved by using BOLD signals in response to changes in blood CO_2 levels induced by actively modulating the breathing pattern such as during a breath-hold challenge (Donahue et al., 2009; Fierstra et al., 2013; Kannurpatti et al., 2010; Pillai & Mikulis, 2014; Pinto, Jorge, Sousa, Vilela, & Figueiredo, 2016; Tancredi & Hoge, 2013). In this way, the cerebral blood flow is regulated by relaxing the vasodilatory factors lining the arterioles and precapillaries due to decreasing the intracellular pH as the intravascular CO_2 concentration is increased. The induced changes in the level of blood oxygenation can then be detected by BOLD fMRI (Bandettini & Wong, 1997; J. J. Chen, 2018; Kastrup, Kruger, Glover, & Moseley, 1999; Kastrup, Li, et al., 1999; Li et al., 1999; Madden, 1993). Nevertheless, this approach has some practical disadvantages, such as the need for considerable subject cooperation, which may be challenging in clinical practice (Jahanian et al., 2017; Liu et al., 2017; Liu et al., 2021). To circumvent this and other issues, resting-state fMRI data can be utilized as an alternative approach for CVR mapping (Birn et al., 2006; Birn et al., 2008; B. B. Biswal et al., 2007; De Vis et al., 2018; Di et al., 2013; Golestani et al., 2017; Golestani, Wei, et al., 2016; Jahanian et al., 2017; Jahanian et al., 2014; Kalcher et al., 2013; Kannurpatti & Biswal, 2008; Kannurpatti et al., 2014; Lipp et al., 2015; Liu et al., 2017; Taneja et al., 2019; Yunjie Tong et al., 2019; K. A. Tsvetanov

et al., 2015; Wise et al., 2004). Evidence from these studies revealed that low-frequency resting-state BOLD fluctuations carry information associated with vasoreactivity to intrinsic blood CO_2 elevations during free breathing over time. Such an approach should, presumably, enable the detection of areas with compromised vasoreactivity, thereby potentially indicating NVU (De Vis et al., 2018). The resting-state CVR maps can be adversely affected by NVU in a similar manner to task-based fMRI maps (S. Agarwal et al., 2017; J. Yang et al., 2020). To leverage this fact, the examination of the spatial correspondence between the task-fMRI activation and resting-state CVR maps in a cohort of patients with focal pathology would provide a confirmatory approach to conclusively indicate the extent to which the resting-state CVR maps enable the identification of NVU-induced false negatives in clinical task-based fMRI activation.

In this study, our objective was to investigate the ability of resting-state CVR maps to reveal potential sites of NVU in task-based fMRI activation maps of patients with brain tumors. Our central hypothesis was that NVU is only present in areas where CVR is impaired. Accordingly, we tested whether holes on resting-state CVR maps spatially correspond to holes on task-based fMRI activation maps, where underlying neurons are functionally intact (as verified by behavioral data). This study is the first step toward qualifying the degree of association and predictability between resting-state CVR and task-fMRI maps for identifying potential NVU. The results of this project provide a starting point for further clinical studies to determine the sensitivity and specificity of resting-state CVR in a broader population of patients with brain pathology.

Materials And Methods

Participants

A publicly available database, collected by Pernet et al. (2016), was used for this study. The database is freely accessible at https://ukdataservice.ac.uk, and includes data from 22 patients with different types of brain tumors (Pernet et al., 2016). The data was first collected as part of a pilot study to validate the use of task-based fMRI brain mapping for neurosurgical planning (Pernet et al., 2016). For each patient, the primary researchers collected imaging data, demographic information, diagnosis reports, and the results of behavioral tests and clinical examinations.

In order for us to include a patient from the database, the data needed to contain: (1) Both task and resting-state fMRI images; and 2) A tumor within or near eloquent cortex around the posterior frontal lobe, or around the anterior parietal lobe, or above of the upper surface of the temporal lobe. The latter was considered as those areas could be mapped by motor task-fMRI scans thereby including but not limited to Primary Motor (M1), Supplementary Motor (SM), and Pre-motor (Pre-M) areas. These selection criteria resulted in a total number of 13 patient datasets for our study. Table 4.1 summarizes non-imaging data of 13 patients.

Table 4.1. Patients' Data (Demographic, Tumor, Behavioral, and Clinical)

Patient	Age	Sex	Tumor Type	Tumor Location	Behavioral & Clinical Data
P.A.	27	F	Astrocytoma II	Left Temporal	No Pre-op report of abnormality
P.B.	63	F	GBM	Left M1	No Pre-op report of abnormality, +NART & +COWAT
P.C.	43	M	Oligodendrocyte II	Left SMA	No Pre-op report of abnormality, +NART & +COWAT
P.D.	25	F	Astrocytoma III	Right SMA	No Pre-op report of abnormality, +NART
P.E.	28	F	Meningioma	Right SMA	No Pre-op report of abnormality, +NART & +COWAT
P.F.	54	M	Meningioma	Left Pre-M	No Pre-op report of abnormality, +NART & +COWAT
P.G.	65	F	Metastatic Lung Cancer	Right S1	No Pre-op report of abnormality, +NART
P.H.	42	M	GBM	Right M1	No Pre-op report of abnormality, +NART, Post-op hemiplegia following by partial recovery
P.I.	40	F	GBM	Right M1	No Pre-op report of abnormality
P.J.	49	F	GBM	Right M1	No Pre-op report of abnormality, +NART
P.K.	41	M	Oligodendrocyte II	Right Pre-M	No Pre-op report of abnormality, +NART
P.L.	41	M	Astrocytoma II	Right Insula	No Pre-op report of abnormality, +NART & +COWAT
P.M.	50	M	---	Right M1	Presurgical Motor Seizure

F: Female; **M:** Male; **M1:** Primary Motor Cortex; **SMA:** Supplementary Motor Area; **Pre-M:** Premotor Cortex; **Pre-op:** Pre-operation; **Post-opt**: Post-operation; **NART:** National Adult Reading Test (oral reading test); **COWAT:** Controlled Oral Word Association Test (verbal fluency test); **+** indicates that the patient performed the test successfully.

Imaging Data

The primary researchers collected functional imaging data including, but not limited to, two protocols per patient: a 7.5 min motor task and a 5 min resting-state scan. The motor task was a block-design paradigm consisting of alternating finger tapping (unilateral), foot twitching (unilateral), and lip pursing. The task activation blocks were interleaved with blocks of rest, during which subjects fixated on a cross on the screen. The motor-task scan consisted of 184 image volumes including 4 dummy scans at the beginning and epochs of 30 sec activation–rest with finger-onsets (TR) = [0 36 72 108 144], foot-onsets (TR) = [12 48 84 120 156], and lips-onsets (TR) = [24 60 96 132 168] (See http://doi.org/10.5255/UKDA-SN-851861 for more information). More details about the sequences can be found in previously published papers, in which the validity of fMRI protocols was supported by test-retest analyses on healthy controls (Krzysztof J Gorgolewski et al., 2013; K. J. Gorgolewski, Storkey, Bastin, & Pernet, 2012; Krzysztof J. Gorgolewski, Storkey, Bastin, Whittle, & Pernet, 2013). In our project, we also used tumor and edema volumes from the tissue-classes dataset of each patient.

Imaging Data Acquisition

The primary researchers acquired imaging data on a General Electric Signa HDxt 1.5Tesla scanner (GE Healthcare Signa HDxt, Waukesha, WI) at the Center for Clinical Brain Sciences, University of Edinburgh, UK (Pernet et al., 2016). The metadata related to imaging data is available at http://doi.org/10.5255/UKDA-SN-851861. Accordingly, the acquisition parameters for T1-weighted anatomical images were as follows: 3D inversion recovery prepared (IRP) imaging volumes, field of view of 256 mm, slice thickness of 1.5mm, acquisition matrix of 256 ×

256, TR = 10 sec, TE = 4 sec, 8° flip angle, and 156 oblique coronal images. Using an 8-channel, phased array head coil, the acquisition parameters for T2*-weighted single-shot gradient echo, echo-planar imaging fMRI scans were as follows: field of view 256 mm, slice thickness = 4 mm, TR = 2500 ms, TE = 50 ms, flip angle = 90°, acquisition matrix of 64 × 64, and 30 oblique axial slices per volume. All functional runs started with 4 dummy scans.

Preprocessing

We performed the data preprocessing with the AFNI (http://afni.nimh.nih.gov/afni, version 19.3.11, RRID:SCR_005927) software package (Cox, 1996). For each patient, we first deobliqued the reconstructed structural and functional volumes with different obliquities (AFNI's 3dWarp) and then conducted the preprocessing using an *afni.proc.py* script as follows: For each motor-task functional dataset, the first 4 dummy scans were discarded (AFNI's 3dTcat), yielding a total of 180 images. All functional volumes of all runs (task-based and resting-state) were brought into spatial alignment with each other (volume registration), with the skull-stripped T1-weighted anatomical images, and with the standard space using the AFNI default Talairach space template (TT_N27+tlrc) (Holmes et al., 1998). This was performed by first identifying a single time point whose associated image volume had a minimum number of voxels with extreme fMRI signal values (a.k.a. outliers) (AFNI's 3dToutcount). This volume was then used as the base for aligning all other image volumes in the timeseries after first removing any large signal spikes (AFNI's 3dDespike). The alignment process itself was composed of three stages: (1) co-registration within each timeseries (AFNI's 3dvolreg), (2) registration to the anatomical dataset (AFNI's align_epi_anat.py), and (3) registration to the standard space of Talairach using the TT_N27 space template (AFNI's @auto_tlrc). These three alignments were accomplished in a single step by

combining the three transformation matrices (AFNI's 3dAllineate). The preceding alignment process generated six time-course signals corresponding to head movement along three directions of translation and three axes of rotation. The derivatives of the head motion signals were then also computed. The next pre-processing step was to smooth each run with a 6 mm full width at half max (FWHM) Gaussian kernel (AFNI's 3dmerge) and create a brain-masked dataset (AFNI's 3dAutomask). Finally, the functional datasets were corrected for the effects of linear trend and head motion through the following: (1) time points in the BOLD fMRI data having particularly aberrant values (Euclidean norm of the motion derivatives > 0.2), were identified, (2) each voxel's timeseries was then scaled to a range of 0-200 with a mean of 100 (AFNI's 3dTstat and 3dcalc), (3) to model head motion effects, AFNI's 3dDeconvolve was used with the head motion signals and their derivatives (see above) in a linear regression analysis while ignoring the aberrant timepoints identified in step (1), and (4) to obtain the "cleaned" timeseries data, the aberrant time points identified in step (1) were replaced by interpolation, and the motion signals (from step 3) were regressed out (AFNI's 3dTproject). Ultimately, the cleaned and corrected time-course signals were included for the analysis, regardless of the subject's behavioral and clinical data.

Data Analysis

Task-based fMRI Activation Maps

In this study, we performed the data analysis at the individual subject level. On a voxel-wise basis, task-related BOLD responses were identified using a general linear model analysis (AFNI's 3dDeconvolve). In this way, a fitted model of multiple scaled reference waveforms was estimated for each voxel's time series. The model resulted in statistical maps for the significance

of the fit and BOLD amplitudes (a.k.a. beta coefficients) in response to the task relative to the rest (a.k.a. the baseline model). Standard activation maps were then created by computing Z-scores from the results of general linear model analysis. Our analysis was limited to the data associated with a lip-pursing task due to its bilateral representation. Finally, to identify active voxels, a dual threshold setting was used. This was performed by computing a cluster-size thresholding that controlled the false positive rate (FPR) globally for a given voxel-wise p-value threshold (AFNI's 3dClustSim & 3dFWHMx). The voxels surviving the cluster-size thresholding for a nominal 1% FPR and an uncorrected p-value of 0.001 were then found (AFNI's 3dClusterize) and used for all subsequent analyses.

Resting-state CVR Maps

For each voxel, the resting-state fMRI signal power within a frequency band from 0.01 to 0.08 Hz (a.k.a. amplitude of low-frequency fluctuation [ALFF]) was computed and used as the voxel's resting-state CVR metric (AFNI's 3dRSFC) (Yang et al., 2007; Zang et al., 2007). We will refer to the ALFF metric as the resting-state "CVRe" metric, where the "e" implies "estimate".

ROIs

To create ROIs, the following steps were performed: (1) Using the standard brain atlas of TT-Daemon (Lancaster et al., 2000), we created a mask in each hemisphere including the Brodmann areas 1 - 4 (AFNI's Draw Dataset Plugin); (2) Using the FSL's FAST segmentation tool (https://fsl.fmrib.ox.ac.uk, version: 6.0.2, RRID:SCR_002823), the skull-stripped T1-weighted anatomical images were segmented into three different classes: gray matter, white matter, and cerebrovascular fluid (Y. Zhang et al., 2001). The volume consisting only of the gray matter was then further processed to ensure that the volume had not been contaminated by some portions of diseased areas, thus, a mask including tumor and edema volumes was used to remove

diseased tissue from the gray matter volume; (3) The masks defined in step (1) were restricted to the gray matter volume and resampled to have the same voxel size and dimension as the statistical datasets (AFNI's 3dresample); (4) The masks for each patient were visually examined to ensure they encompassed the primary motor and somatosensory areas, mainly due to the possibility of tumor-induced anatomical compression or deformation.

Statistical Analysis of Task-fMRI Activation Maps

The lip-pursing fMRI activation was compared between the two ipsilesional and contralesional ROIs based on the assumption that fMRI activation should be intact in the contralesional hemisphere and symmetrical across hemispheres in a disease-free brain (White et al., 1997; Zaca et al., 2014). The comparison was performed by using a two-sample student's t-test to determine if the mean Z-score in the ipsilesional ROI was significantly less than that in the contralesional ROI (p-value < 0.01). A significantly reduced mean Z-score of the ipsilesional vs. contralesional ROI would then suggest that locally impaired BOLD responses might be due to NVU rather than neuronal damage. To verify true NVU, the results were cross-validated with the behavioral and clinical data. A normally preserved behavioral response (lip movement) would then indicate preserved neural function and thereby confirm the occurrence of NVU.

Statistical Analysis of Resting-state CVRe Maps

For each patient, the spatial pattern of resting-state metric was thresholded for maximum coverage of gray matter with minimal labeling of white matter. The details on threshold setting are described in Chapter 2. A binary map was then created based on the voxels' CVR status (presence = 1 or absence = 0). The presence of resting-state CVRe metric was compared between the two ipsilesional and contralesional ROIs. This was performed by using a chi-square goodness of fit

test to determine if the presence of resting-state ALFF in the ipsilesional ROI was significantly lower than that in the contralesional ROI (p-value < 0.01).

Comparing Task-fMRI Activation Vs. Resting-state CVRe Maps

To further establish a backup statement for our results, we quantitatively examined the spatial association between resting-state CVRe and task-fMRI activation maps. This examination was performed for each patient by first converting the two maps into their binary version based on the status (presence=1 or absence=0) of resting-state CVRe and task-fMRI activations. A measure of spatial similarity (SS) between the two maps was then computed for each ROI as follows:

$$SS = \frac{\text{(resting-state CVRe) } \cap \text{ (task-based fMRI)}}{\text{(resting-state CVRe) U (task-based fMRI)}} \qquad \text{(Equation 4.1)}$$

The measure of SS could range from 0% – 100%. For each patient, the computed measure in ipsilesional ROI was then evaluated compared to the measure of SS obtained from data in the contralesional ROI.

Results

In general terms, the patient cohort studied in this project was organized into four broad NVU categories: (1) “Late-stage NVU”, (2) “Early-stage NVU”, (3) “NO-NVU (viable tissue)”, and (4) “NO-NVU (non-viable tissue)”. As previously mentioned, the term NVU refers to a situation in which the neuro-vascular coupling cascade is disturbed by focal pathology such as a tumor, though the underlying neurons remain functionally intact. Figure 4.1 displays the NVU

scenario schematically. Here, we used the term “Late-stage NVU” to explain a situation wherein the tumor had a profound impact on neuro-vascular coupling at the point of vasculature, causing vasoreactivity dysfunction while leaving the underlying neurons functionally intact (Fig. 4.1). From a surgical standpoint, an absence of both task-activation and CVR in peritumoral regions was then characterized as “Late-stage NVU,” when neither tissue displacement nor clinical evidence that the patient had lip/face-function deficit or difficulty in task performance existed. Contrarily, the term “Early-stage NVU” was used to signify a condition in which the lack of BOLD response within a functionally intact area could not be explained by vasomotor dysfunction (Fig. 4.1). This differed from a situation in which loss of task-related fMRI activation despite the presence of CVR and intact behavioral data could occur due to a physical displacement of active tissue as a result of the presence of the tumor mass. In the case of “Early-stage NVU”, we ruled out this possibility through inspection of anatomical alignment. Moreover, the patients whose impaired task-fMRI activation were consistent with clinical evidence of behavioral deficit, were classified as “NO-NVU (non-viable tissue)”. Finally, if the task-fMRI activation pattern was normal, or an atypical activation pattern was a consequence of a unilateral shift of activated areas (functional displacement), the case would then be categorized into the class of “NO-NVU (viable tissue).”

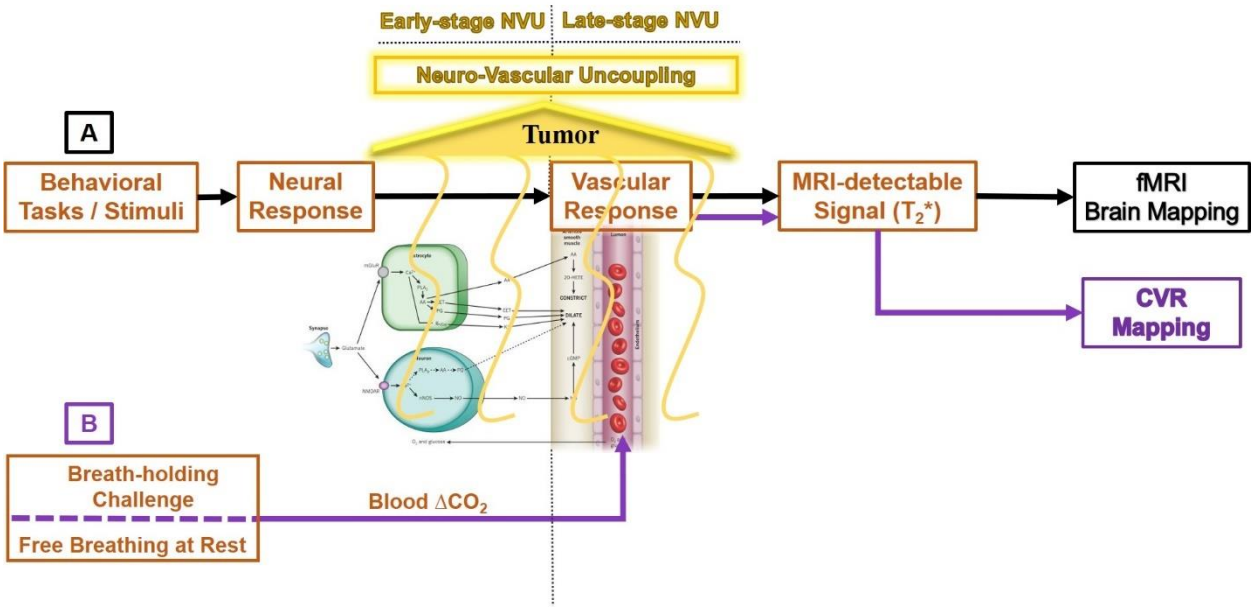

Figure 4.1. (A) Schematic diagram of task-based fMRI brain mapping based on neuro-vascular coupling mechanisms (black arrows). The image shows different components involved in the neuro-vascular coupling cascade (Attwell et al., 2010). The presence of tumor can disrupt the neuro-vascular coupling cascade at any stage from neurons to vessels (shown here in yellow), termed as neuro-vascular uncoupling. There is a possibility for Late-stage NVU due to pathology-induced vascular dysfunction or Early-stage NVU due to disturbance of coupling at a stage before vasculature. **(B)** CVR mapping based on vascular response to changes in blood CO_2 induced by breath-holding or free breathing at rest (purple arrows). **CVR**: cerebrovascular reactivity; **NVU:** neuro-vascular uncoupling; **CO_2:** carbon dioxide; **fMRI:** functional magnetic resonance imaging.

Figure 4.2. presents the four possible outcomes for patient classification in terms of NVU as a schematic diagram. A task-fMRI activation map would be labeled as impaired if the asymmetrical activation could not be due to the physical displacement of the functional tissue. . The neural viability, tested behaviorally, would be considered impaired if the patient experienced any behavioral deficits and/or difficulties in the task performance. When the task-fMRI activation map was identified as impaired despite having any behavioral abnormality, the status of CVR would then suggest the occurrence of early- or late-stage NVU. It is important to note that the implementation of testing the impaired task-fMRI activation for potential NVU in the clinical setting would be to inspect the CVR maps in conjunction with the task-fMRI maps.

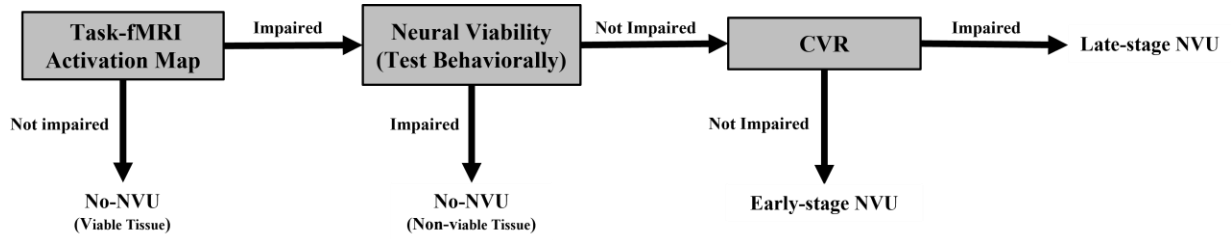

Figure 4.2. Schematic diagram for patient classification to either one of the four NVU categories: "No-NVU (Viable Tissue)", "No-NVU (Non-viable Tissue)", "Late-stage NVU", and "Early-stage NVU". **CVR:** cerebrovascular reactivity; **NVU:** neuro-vascular uncoupling, **fMRI:** functional magnetic resonance imaging.

Here we discuss the results in three main sections: (1) the comparison of ipsilesional vs. contralesional task-based fMRI activation as a method to determine impaired patterns of activity, (2) the comparison of resting-state CVRe within motor areas in the ipsilesional hemisphere with that of the contralesional hemisphere, and (3) the NVU classification of all patients based on the association between the resting-state CVRe and task-fMRI activation maps, together with the patients' behavioral and clinical data.

Ipsilesional vs. Contralesional Task-fMRI Activation

Of the 13 patients for whom both resting-state and task-based fMRI data were available, a total of four patients exhibited comparable task-induced BOLD responses within the two ipsilesional and contralesional hemispheres. The rest of nine patients (i.e. nearly 70% of all patients), however, displayed a significant decrease of task-fMRI activation within the ipsilesional vs. contralesional hemisphere (Student t-test, p-value < 0.01). For these patients, the task-fMRI activation maps were labeled as asymmetrical. Table 4.2 summarizes the results from the lip-

pursing fMRI activation comparisons between the two hemispheres for the 13 patients with brain tumors.

Table 4.2. Lip-pursing Task-fMRI Activation Comparisons Between the Two Hemispheres

Patient	Ipsilesional BOLD Response (Mean Z-score ± SD)	Contralesional BOLD Response (Mean Z-score ± SD)	Ipsilesional vs. Contralesional Activation
P.A.	3.4 ± 2.5	3.3 ± 2.8	Comparable
P.B.	2.5 ± 2.8	1.9 ± 2.6	Comparable
P.C.	5.8 ± 3.1	5.1 ± 2.6	Comparable
P.D.	2.1 ± 3.2	2.0 ± 3.0	Comparable
P.E.	2.6 ± 3.6	4.9 ± 4.2	Asymmetrical
P.F.	1.3 ± 2.1	4.8 ± 2.3	Asymmetrical
P.G.	2.1 ± 3.1	8.4 ± 6.8	Asymmetrical
P.H.	0.0	3.1 ± 4.0	Asymmetrical
P.I.	1.7 ± 2.4	5.5 ± 3.0	Asymmetrical
P.J.	0.6 ± 1.6	2.4 ± 3.3	Asymmetrical
P.K.	1.8 ± 2.6	4.4 ± 3.0	Asymmetrical
P.L.	3.5 ± 4.0	5.7 ± 4.6	Asymmetrical
P.M.	1.8 ± 2.2	5.3 ± 2.5	Asymmetrical

SD: standard deviation; **BOLD:** blood oxygenation level dependent

Ipsilesional vs. Contralesional Resting-state CVRe Metric

A summary of the resting-state CVRe comparisons between the two ROIs for the 13 patients is shown in Table 4.3. The resting-state CVRe pattern was labeled as impaired when the proportion of resting-state CVRe-present voxels within the ipsilesional ROI was significantly less than that of contralesional ROI (Chi-square, goodness of fit, $p < 0.01$).

Table 4.3. Resting-state CVRe Comparisons Between the Two Hemispheres

Patient	Ipsilesional CVR-present Voxels	Contralesional CVR-present Voxels	Ipsilesional vs. Contralesional CVR
P.A.	88%	94%	Comparable
P.B.	92%	86%	Comparable
P.C.	71%	77%	Comparable
P.D.	80%	88%	Comparable
P.E.	50%	64%	Impaired
P.F.	29%	66%	Impaired
P.G.	27%	52%	Impaired
P.H.	45%	68%	Impaired
P.I.	74%	99%	Impaired
P.J.	93%	89%	Comparable
P.K.	70%	59%	Comparable
P.L.	92%	86%	Comparable
P.M.	88%	92%	Comparable

%: percentage; **CVR:** cerebro-vascular reactivity

NVU Classification of Patients

Table 4.4 summarizes the results of step-by-step decision-making process for all 13 patients by which each patient was categorized into one of the four NVU categories. Overall, eight patients were identified as cases of "NO-NVU (viable-tissue)", four patients were classified as the group of "Late-stage NVU", and one patient was labeled as "Early-stage NVU". Notably, of the 13 patients reviewed in this study, no one was designated as a case of "NO-NVU (non-viable tissue)".

Table 4.4. NVU Classification of Patients with Brain Tumors

Patient	Asymmetric Task-fMRI Activation?	Impaired CVR?	Behavioral Deficits?	Tissue Displacement?	Additional Information?	Classification
P.A.	No	No	No	No	No	NO-NVU (viable tissue)
P.B.	No	No	No	No	No	NO-NVU (viable tissue)
P.C.	No	No	No	No	No	NO-NVU (viable tissue)
P.D.	No	No	No	No	No	NO-NVU (viable tissue)
P.E.	Yes	Yes	No	No	No	Late-stage NVU
P.F.	Yes	Yes	No	No	No	Late-stage NVU
P.G.	Yes	Yes	No	No	No	Late-stage NVU
P.H.	Yes	Yes	No	No	No	Late-stage NVU
P.I.	Yes	Yes	No	Yes	No	NO-NVU (viable tissue)
P.J.	Yes	No	No	Yes	No	NO-NVU (viable tissue)
P.K.	Yes	No	No	No	Yes	NO-NVU (viable tissue)
P.L.	Yes	No	No	No	Yes	NO-NVU (viable tissue)
P.M.	Yes	No	No	No	No	Early-stage NVU

CVR: cerebrovascular reactivity; **NVU:** neurovascular-uncoupling; **fMRI:** functional magnetic resonance imaging

In summary, patients P.A.–P.D. revealed comparable task-fMRI activation and resting-state CVRe between the two ipsilesional and contralesional hemispheres. For these patients, the status of task-fMRI activation maps were comparable (not impaired). Consistent with these results, the clinical data did not show that these patients experienced any motor function deficit and/or task performance difficulty. Consequently, they were classified as "NO-NVU (viable tissue)". Among the rest of patients with asymmetric task-fMRI activation, a total of five patients (i.e. P.E. – P.I.) exhibited a significantly lower rate of ipsilesional resting-state CVRe-present voxels (Chi-Square goodness of fit, $P < 0.01$). Notably, clinical data for this group of patients did not reveal any evidence of behavioral deficit or difficulty with the task performance. Of this group, the four patients of P.E. – P.H. were characterized as "Late-stage NVU", which accounted for

approximately 45% of total cases who had shown an impaired pattern of task-fMRI activation across the two hemispheres (i.e. nearly 31% of all patients). Notably, scrutinizing the data of the fifth patient (i.e. patient P.I.) revealed a shift of activated area within the ipsilesional hemisphere, presumably due to structural deformation caused by the tumor mass. Perhaps, due to local folding of the tissue, the asymmetrical task-fMRI activation map for this patient, despite a lack of behavioral deficit or task performance difficulty, should not be labeled as impaired. The patient was more likely to be characterized as a case of "NO-NVU (viable tissue)".

Patients P.J. – P.M. also exhibited asymmetric task-fMRI activation but comparable resting-state CVRe between the two ROIs. Moreover, for all these patients, no evidence of behavioral deficits was found in their clinical data. Notably, for patient P.J., a careful examination of the data demonstrated anatomical distortion in the side of tumor and a relocation of activated area within the ipsilesional hemisphere. Due to the asymmetrical but preserved activation pattern and the lack of behavioral deficit experienced by this patient, we categorized this case into the class of "NO-NVU (viable tissue)' [See *Illustrative Case Reports* section below for more details]. The examination of data for the other two patients (i.e. P.K. and P.L.) revealed that the asymmetry of activation in their task-fMRI brain maps was associated with an ipsilesional absence of BOLD responses in areas distant from the tumor with a little (if no) chance of resection. Such an asymmetry could be explained by the tumor and its edema affecting the neuro-vascular coupling in the remote areas as a consequence of traveling the tumorous cells along the microvasculature. However, the preserved CVR and the lack of behavioral deficit would make this scenario less likely to occur. In these cases, the suspected brain regions were potentially characterized as "NO-NVU (viable tissue)" (See *Illustrative Case Reports* section below for more details). Finally, patient P.M. revealed an absence of activation in peritumoral regions wherein the resting-state

CVRe was present. This patient, with lack of activation in areas proximal to the tumor, was classified into the class of "Early-stage NVU" [See *Illustrative Case Reports* section below for more details].

Spatial Similarity between Task-fMRI Activation and Resting-state CVRe Maps

To further establish a quantitative basis for the results of our NVU classification, we quantitatively examined the spatial correspondence between the task-fMRI activation and resting-state CVRe maps. For this purpose, we used the spatial similarity metric to test how similar the two maps were in the ipsilesional ROI in relation to that of the contralesional ROI. Table 4.5 summarizes the results of voxel-wise comparisons between the spatial patterns of task-fMRI activation and resting-state CVRe maps in each ROI and the percent of changes in their spatial similarity within the ipsilesional ROI relative to the contralesional ROI.

Overall, a total of five patients (i.e. patients P.I. – P.M.) had a relatively compromised spatial similarity between the two maps in the ipsilesional vs. contralesional hemisphere. For patients P.I. and P.J., consistent with our observations of structural deformation and the displacement as well as the decreased size of activated areas, the two maps had a relatively poor spatial similarity in the ipsilesional ROI compared with that of the contralesional ROI. The percent difference between the two ipsilesional and contralesional SSs was -38% and -58% for patient P.I. and patient P.J., respectively. In patients P.K. and P.L., however, the two maps of task-fMRI activation and resting-state CVRe had a relatively moderate spatial agreement in the ipsilesional vs. contralesional hemisphere (percentage difference in P.K. = -23% and P.L. = -24%). These

results were anticipated due to an absence of activation in ipsilesional areas remote from the tumor despite fairly preserved resting-state CVRe. Patient P.M. had also a comparatively poor spatial correspondence between the task-fMRI activation and resting-state CVRe in the ipsilesional vs. contralesional ROI (48% vs. 81%). This result closely corresponds with the lack of activation adjacent to the tumor, wherein the resting-state CVRe was preserved (i.e. “Early-stage NVU”).

As could be expected, the percent difference between SS measures for patients P.D. – P.G. who identified as “Late-stage NVU”, was in a moderately similar range to that for patients P.A. – P.D. who had comparable both task-fMRI activation and resting-state CVRe maps (3% – 17% vs. 4% – 17%). Such a result for “Late-stage NVU” patients showed that the compromised areas (holes) in task-fMRI activation maps spatially correspond to that of resting-state CVRe maps, so that relatively comparable SS measures were obtained for the two hemispheres.

Table 4.5. Spatial Similarity of Task-fMRI Activation with Resting-State CVRe Comparisons between Two ROIs

Patient	Ipsilesional Measure of SS	Contralesional Measure of SS	Percentage Difference
P.A.	79%	67%	**+ 16%**
P.B.	49%	51%	**- 4 %**
P.C.	69%	62%	**+ 11%**
P.D.	51%	43%	**+ 17%**
P.E.	70%	65%	**+ 7 %**
P.F.	58%	53%	**+ 8 %**
P.G.	68%	66%	**+ 3 %**
P.H.	55%	65%	**- 17%**
P.I.	55%	81%	**- 38%**
P.J.	23%	42%	**- 58%**
P.K.	43%	54%	**- 23%**
P.L.	41%	53%	**- 24%**
P.M.	48%	81%	**- 53%**

SS: spatial similarity; **+:** increase; **-:** decrease

Illustrative Case Reports

The lip-pursing task-fMRI activation and the optimized resting-state CVRe maps are shown in a series of patients, including one case for different situations discussed in *NVU Classification of Patients* above (in the present study, no patients fell in the 'No-NVU non-viable tissue' category). For each case, the steps to take for classifying the patient to one of the NVU categories are described in detail.

Case Report No.1 – Patient P.F.: "Late-stage NVU"

Illustrated in Figure 4.3. are the task-fMRI activation and the resting-state CVRe maps of a 54-year-old man with a meningioma involving the left frontal lobe. Presurgical fMRI brain mapping with a lip-pursing task demonstrated asymmetrical activation in terms of magnitude and extent within the ipsilesional vs. contralesional hemisphere, potentially indicative of impaired neural function (Fig. 4.3, first row). However, the patient's behavioral and clinical examinations did not reveal obvious lip/face weakness or poor task performance, suggesting that the underlying neurons were not dysfunctional. Additionally, resting-state CVRe maps showed a significantly reduced presence of CVR throughout the left versus right motor cortex (Note reversal of left/right in figure), most notably in the posterolateral corner of the tumor (Fig. 4.3, orange arrow in second row). Lack of CVR in this area suggested that the compromised task-fMRI activation could be due to vascular dysfunction induced by the tumor, rather than due to neural damage. "Late-stage NVU" was then confirmed by the absence of a lip/face-function deficit.

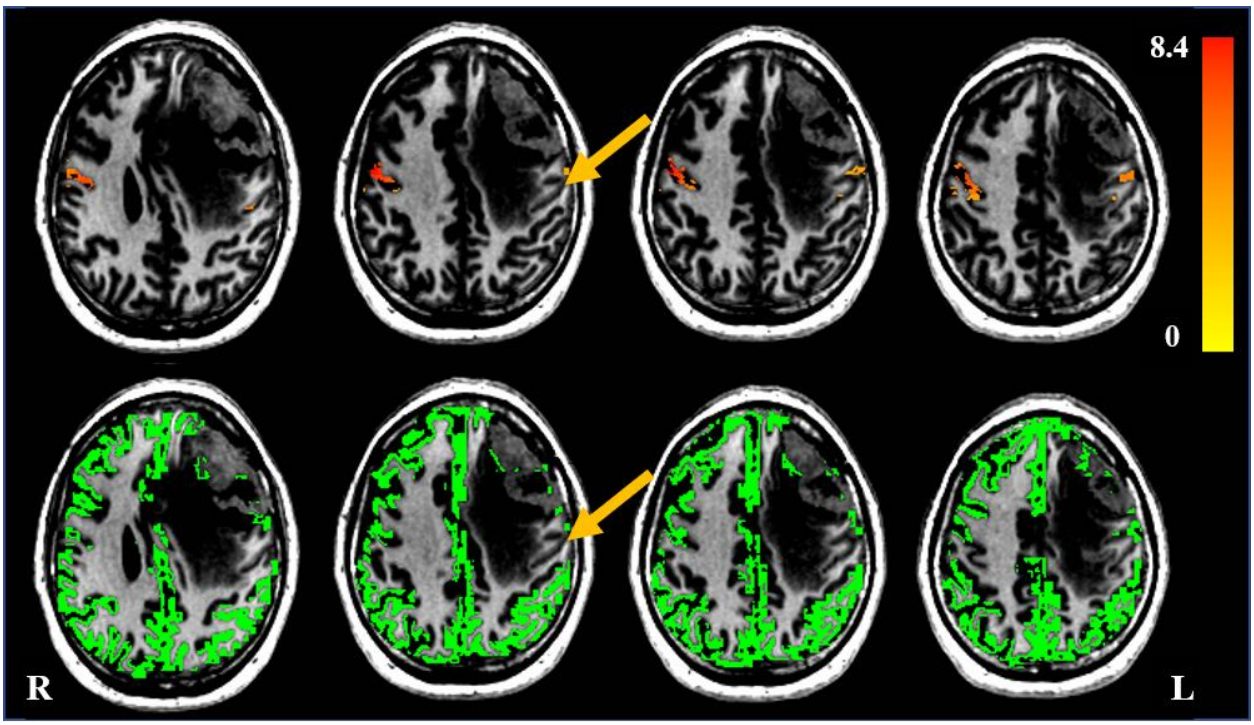

Figure 4.3. Late-stage NVU. **Top:** Axial representation of task-fMRI activation in motor areas. **Bottom:** Axial representation of resting-state CVRe (green) in cortical gray matter. Orange arrows show a brain area with absence of both task-fMRI activation (top) and resting-state CVRe (bottom) due to "Late-stage NVU". **R:** right, **L:** left.

Case Report No.2 – Patient P.M.: "Early-stage NVU"

Figure 4.4 shows the lip-pursing fMRI activation and the resting-state CVRe maps of a 50-year-old man with a brain tumor located in the right primary motor cortex. In behavioral and clinical reports of the patient, there was no evidence of neurological deficits or behavioral abnormality, except that the patient did experience a seizure prior to surgery. The lip-pursing task showed asymmetric activation posterior to the tumor (Fig. 4.4, first row). A comparison of task-fMRI activation between the two hemispheres revealed a significantly impaired BOLD response within the right versus the left motor areas. In contrast, resting-state CVRe maps showed robust BOLD-CVR activation throughout the right hemisphere (Fig. 4.4, second row). Additionally, no report of an obvious motor-function deficit or poor task performance was found in medical records

of the patient, suggesting that the compromised fMRI activation within the tumor bed (orange arrows) could not be a consequence of neural damage or the inability of vessels to dilate. Consistent with this interpretation, there was a relatively lower spatial similarity between the two task-fMRI activation and resting-state CVRs maps in the right vs. the left ROI. Ultimately, the lack of a task-based BOLD response in the posterior edge of the tumor, together with a robust presence of resting-state CVRe, was characterized as “Early-stage NVU”.

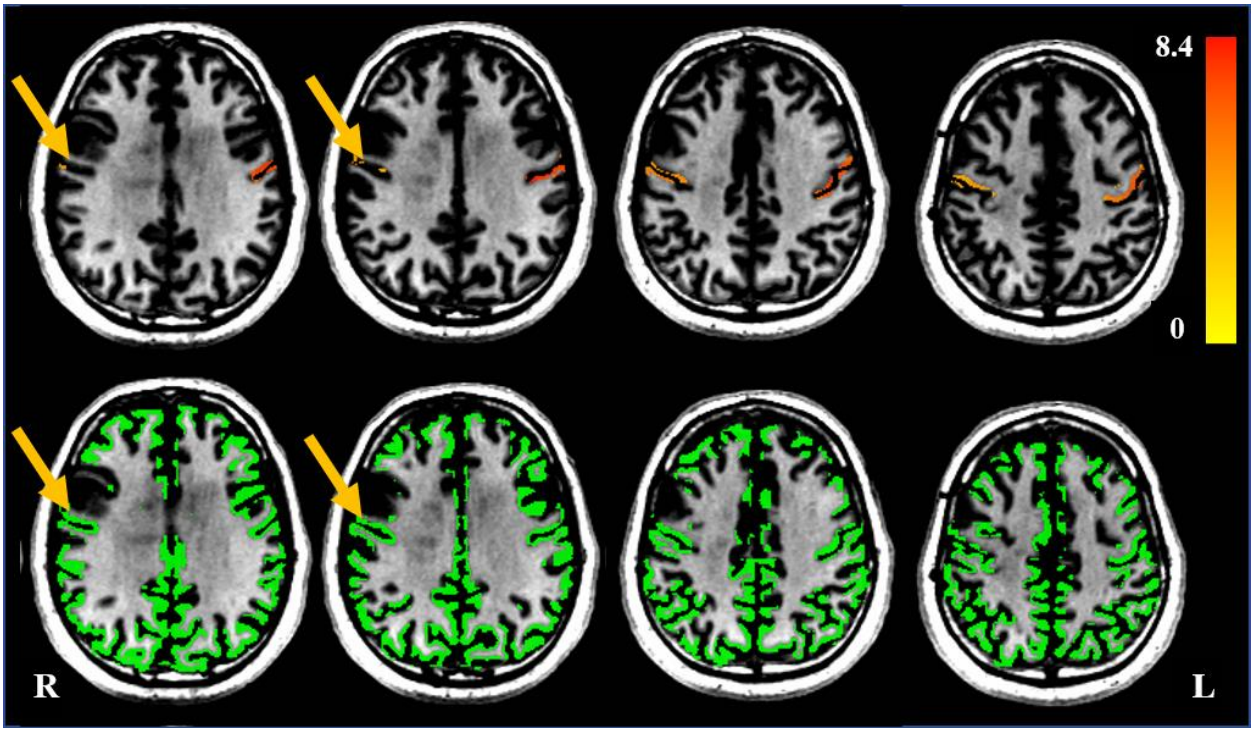

Figure 4.4. Early Stage NVU. **Top:** Axial representation of task-fMRI activation in motor areas, and **Bottom:** resting-state CVRe activation (green) throughout the cortical gray matter ROI. Orange arrows indicate a brain area adjacent to tumor with lack of task-fMRI activation but a robust presence of resting-state CVRe, classified as “Early-stage NVU”. **R:** right, **L:** left.

Case Report No.3 – Patient P.C.: "NO-NVU (Viable Tissue)"

Figure 4.5 demonstrates the axial images of task-fMRI activation and resting-state CVRe for a 43-year-old male patient with an oligodendrocyte located in the left supplementary motor area. The lip-pursing task revealed a statistically comparable activation pattern between the two hemispheres (Fig. 4.5, first row). Along with the symmetrical fMRI activation, robust resting-state CVRe activation was observed throughout the cortical gray matter volume (Fig. 4.5, second row). The functional results were confirmed based on the patient's normal behavioral and clinical examination. Accordingly, the lip-pursing fMRI activation for this patient could not be suspected of NVU and thus, classified as "NO-NVU (viable tissue)".

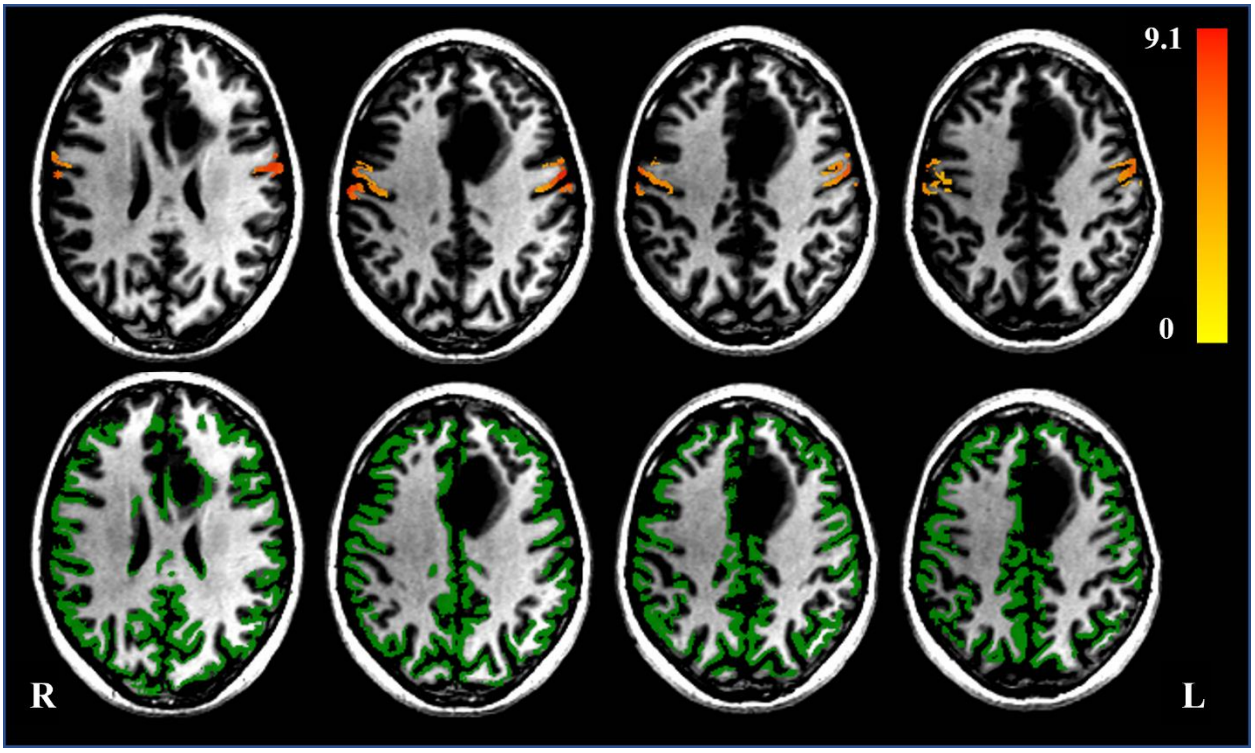

Figure 4.5. NO-NVU (Viable Tissue). **Top:** Axial images of task-fMRI activation in motor areas, and **Bottom:** resting-state CVRe activation (green) throughout the cortical gray matter volume**. R:** right**, L:** left.

Case Report No.4 – Patient P.J.: "NO-NVU (Viable Tissue)" – Physical Displacement of Functional Tissue

The presurgical task-fMRI activation and resting-state CVRe maps of a 49-year-old female patient diagnosed with a glioblastoma multiforme (GBM) in the right primary motor cortex are presented in Figure 4.6. For this patient, despite lack of obvious lip/facial weakness or difficulty in task performance, the lip-pursing task showed robust fMRI activation in the left motor areas but dramatically compromised activation within the homologous areas in the right hemisphere (orange arrows). In contrast, robust BOLD-CVR activation was displayed within the cortical gray matter volume in the two hemispheres. With careful examination of the data, however, a relatively small, activated area was detected in an anterior-superior direction (blue arrows). The relocation of activated area was perhaps a consequence of anatomical deformation due to the tumor mass, more notable in the anterior and anterolateral edges of the tumor. These data suggested that the task-fMRI activation had been diminished due to physical tissue deformation, rather than due to neuronal or vascular dysfunction. The displacement of cortical tissue and perhaps the local folding of sulci in this case suggested that the compromised areas were less likely to be indicative of NVU, though resection of these areas might still cause post-treatment neurological deficits due to damage to other neurons. This case was thus more likely to be in the class of "NO-NVU (viable tissue)".

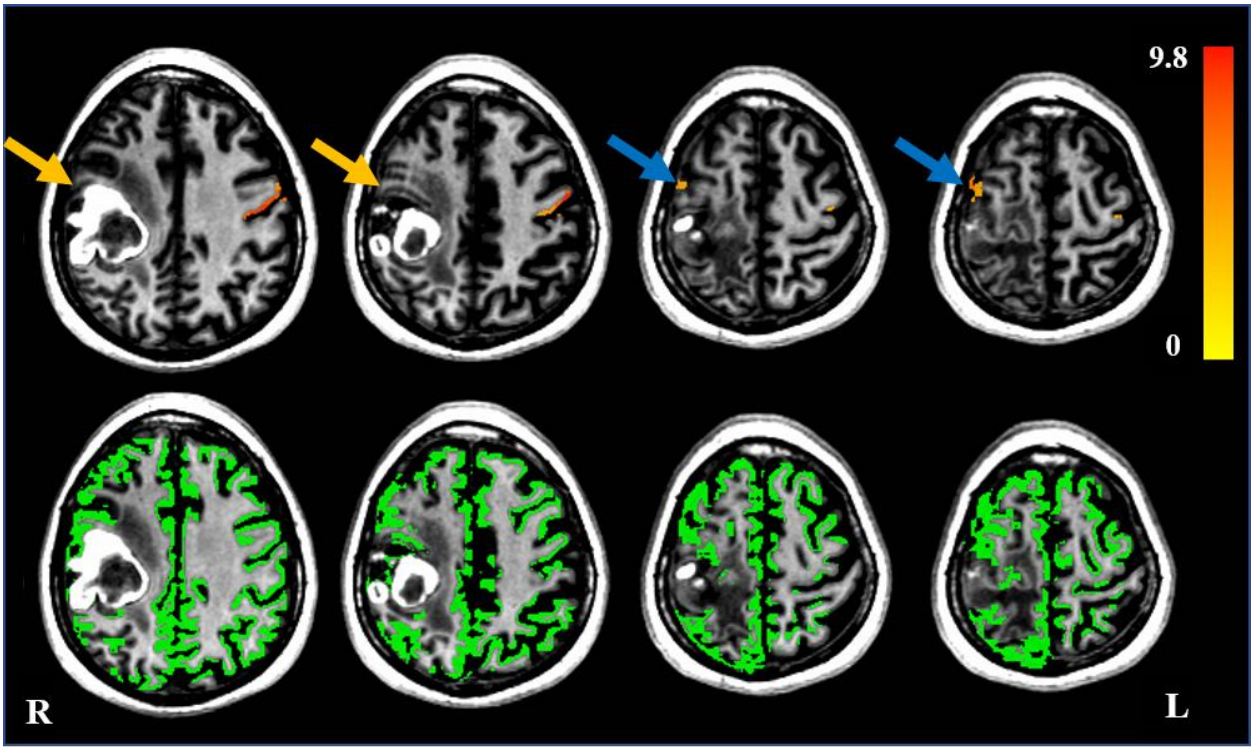

Figure 4.6. NO-NVU (Viable Tissue) – Physical Displacement of Functional Tissue**. Top:** Axial images of task-fMRI activation in motor areas, and **Bottom:** resting-state CVRe activation (green) throughout the cortical gray matter volume. Orange arrows indicate areas with compromised task-fMRI activation. Blue arrows show the shift of activated area in a superior-anterior direction. **R:** right, **L:** left.

Case Report No.5 – Patient P.L.: "NO-NVU (Viable Tissue)" – Absence of Activation in Remote Areas

As shown in Figure 4.7, a lip-pursing task for a 41-year-old man with an astrocytoma involving the right insula resulted in a statistically reduced activation in the ipsilesional hemisphere. In contrast, the resting-state CVRe maps displayed a comparable presence of CVRe metric in both hemispheres (Fig. 4.7, second row). A review of the patient's clinical data did not reveal any gross motor deficits or poor lip-pursing task performance, suggesting that the reduced fMRI activation could not be a consequence of neural damage. Notably, lack of activation was observed in areas distant from the tumor, which would certainly not be a site of surgical treatment

(orange arrows). Indeed, while the both task-fMRI and BOLD-CVR activation were bilaterally preserved within the areas proximal to the tumor, the increased contralesional activation in terms of magnitude and extent might be pathology-induced pseudo dominance. Another explanation could be that the task-fMRI activation in the right vs. leftt hemisphere might not be perfectly symmetric due to local folding of the sulci. The absence of BOLD response could also be explained by the effect of edema on the neuro-vascular coupling in areas distant from the tumor as the tumorous cells travel along the microvasculature. While the occurrence of NVU in such a scenario would be more likely to be due to the disruption of vascular function, the CVR was preserved in this case. Eventually, the lack of activation in remote areas was less likely to imply neuronal damage or be indicative of NVU. We characterized this case as "NO-NVU (viable tissue)".

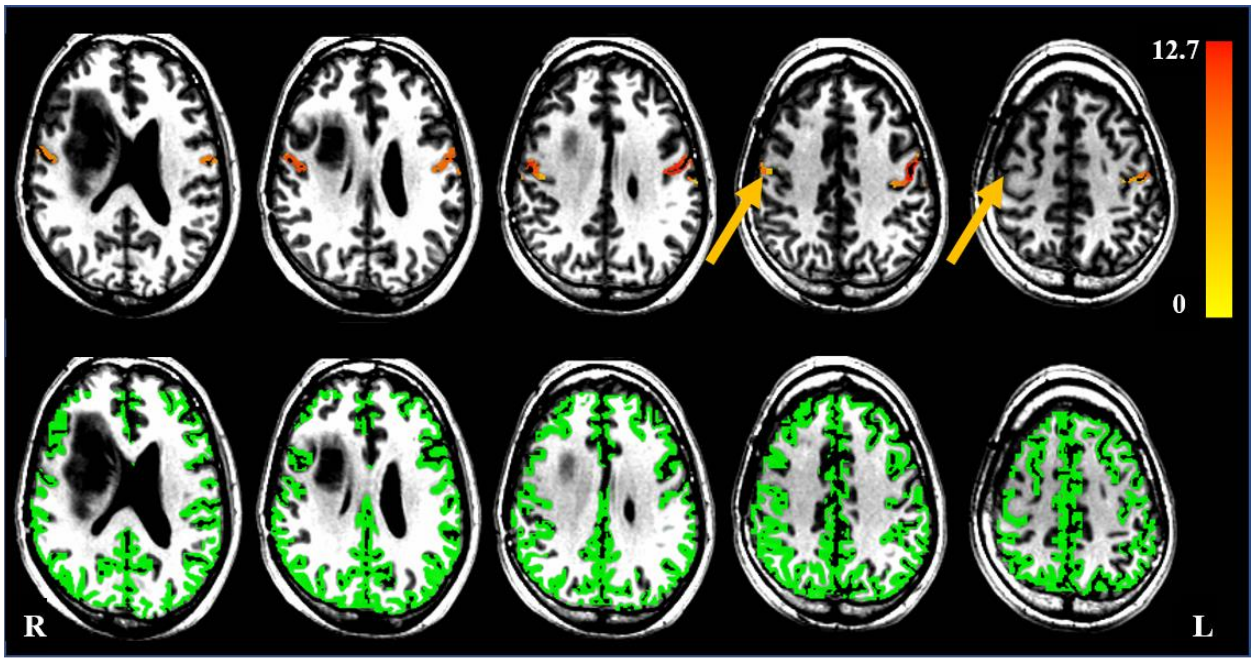

Figure 4.7. NO-NVU (Viable Tissue) – Absence of Activation in Remote Areas. **Top:** Axial representation of task-fMRI activation in motor areas, and **Bottom:** resting-state CVRe (green) throughout the cortical gray matter volume. Orange arrows present reduced fMRI activation in distant areas from the tumor. **R:** right, **L:** left.

Discussion

In this work, we studied the retrospective data from a sample of patients with brain tumors to investigate whether or not CVR mapping using the resting-state metric of ALFF would enable the detection of NVU-induced false negatives on task-fMRI activation maps. This was accomplished by first inspecting the patients' task-fMRI brain maps to determine whether the activation patterns were impaired in areas adjacent to a brain tumor. We then explored patients' resting-state ALFF maps for clear indications of CVR holes corresponding to the ipsilesional task-activation impairment. To ascertain whether or not the compromised regions were functionally intact, each patient's clinical data were then reviewed for evidence of a functional deficit and/or difficulties in task performance experienced by the patient. Of the 13 patients with brain tumors, we identified a total number of five patients (i.e. over 38% of all patients) with falsely impaired task-fMRI activation due to NVU, from which the four revealed a comparable compromised region on both resting-state and task-fMRI brain maps (i.e. nearly 31% of all patients).

This project provided strong evidence that the resting-state CVRe maps can facilitate the detection of eloquent areas at risk for false-negative task-fMRI activation and thereby reduce the potential for unintentional surgical damage. Indeed, we learned that the peritumoral regions with an absence of resting-state ALFF metrics had spatial conformity with erroneous task-fMRI activation dropouts. However, the reverse was not always true; that is, the ipsilesional abnormal task-fMRI activation in an assumingly unaffected brain region would not necessarily come with a spatially analogous impairment of CVR. From the standpoint of clinical utility, a likely implication would then be that the use of ALFF maps for characterizing the false-negative task-fMRI activation blobs is only effective in situations in which the compromised BOLD signals are

associated with the tumor-induced functional failures of the microvasculature. We referred to such a situation as “Late-stage NVU” because the affected point – i.e. microvasculature – is the last component of neuro-vascular coupling cascade (Fig. 4.1).

The primary focus of this project was on evaluating the consistency between the results of resting-state CVRe and task-based fMRI brain mapping in surgically-sensitive areas against the problem of NVU. In general, the results of this study fulfilled the prediction that holes on resting-state CVRe maps spatially correspond to holes on task-based fMRI activation maps, where underlying neurons are functionally intact (verified by behavioral data). This was consistent with prior evidence-based clinical studies demonstrating a significant reduction of both resting-state ALFF and motor-task activation within ipsilesional areas compared with that of analogous contralesional control areas, though using pre-identified patients with NVU and at a group level of analysis (Agarwal, 2017; Agarwal, 2019). Our prediction was based on the premise that NVU is only present in areas in which CVR is impaired. This scenario was mostly followed by our observations of NVU-related compromised task-activation in regions where the CVR metric was also absent. However, data from one patient also displayed a clearly contrary condition, suggesting that the spatial correspondence between NVU-related holes in task-fMRI activation and CVR holes does not occur in the situation we have coined ‘early-stage NVU’.

We noticed that in the setting of preserved CVR, an area may still experience NVU. Interestingly, the functional imaging data of a patient exhibited an impaired task-fMRI activation pattern in peritumoral areas in which the resting-state CVRe was robustly present (Fig. 4.4). On the one hand, the clinical data did not contain any report of obvious lip/facial weakness or poor task performance experienced by the patient, suggesting that the lack of activation was not likely to be due to neuronal damage but rather to NVU. On the other hand, the robust resting-state CVRe

activation throughout the brain regions implied that the compromised BOLD response was not a consequence of vascular inability to dilate. This condition was thus classified as "Early-stage NVU" to be distinguished from those in which the interruption of coupling cascade by a tumor would eventually impair vasoreactivity (i.e. "Late-stage NVU"). Such a possibility had previously been introduced by Ulmer et al. (2004). They reported a case with a tumor-based impaired pattern of fMRI activation within functionally viable areas and argued the potential for such a result due to the disconnection of viable neurons from astrocytes and microvasculature as a consequence of invasive tumor growth (Ulmer, 2004). Nevertheless, the reported case could not necessarily be a case of "Early-stage NVU", because despite a chance that the neuro-astrocyte uncoupling might also proceed to impair vascular function, the presence of regional vasoreactivity was not tested (Ulmer, 2004). Prior research using animal models also provided evidence that a brain tumor has the potential to disrupt the function or structure of any factors contributing to normal neuro-vascular coupling, thereby compromising the task-induced BOLD signals (Farin, 2006; Watkins, 2014). However, to our best knowledge, no study to date has shown that clinical NVU may occur in an area while leaving the regional vasoreactivity intact. Therefore, the current study was the first that demonstrated the possibility for such a scenario.

Due to a lack of systematic investigation of NVU in addition to the absence of data from other modalities and the unavailability of histopathological data, the exact causes of impaired task-fMRI activation in the setting of preserved vasoreactivity remain unknown; however, in light of accumulated evidence from the literature, several pathophysiological factors can potentially be attributed to the occurrence of "Early-stage NVU". One potential reason is that the structural integrity of microvasculature is likely to be preserved even after encasing the perivascular space by glioma cells (Pacioni, 2020). Indeed, interrupting the astrocyte-vascular interaction due to end-

feet displacement by glioma cells may not always be accompanied by the degradation of vascular integrity (Chow, 2016). Such a condition may arise before vascular co-option by infiltrative glioma cells, wherein the control of neurovascular coupling on vasculature is reduced. In this situation, preventing vasoactive agents released from astrocytes from reaching adjacent blood vessels would result in a compromised hemodynamic responses to changes in neural activity. Yet, the vasoreactivity to respiratory-induced variations in blood CO_2 remain intact as endothelial and smooth muscle cells are triggered independently and not through the neuro-vascular coupling cascade (J. J. Chen, 2018). Additionally, through interacting with neighboring brain cells, secreted factors from tumor cells can potentially alter the inhibitory-excitatory balance of peritumoral areas while leaving the nearby neurons and vascular cells functionally intact (Gao, 2020).

In contrast to "Early-stage NVU", the incidence of "Late-stage NVU" can be better understood. A likely explanation is vascular dysregulation due to brain blood barrier (BBB) dysfunction and endothelial damage caused by infiltrative glioma cells. In a such situation, tumorous cells aggressively invade into perivascular space whereas viable neurons are left in the tumor territory (Watkins, 2014; Pacioni, 2020; Lee, 2009). Vascular dysfunction can be induced by the tumor through an abnormal production of ionic and metabolic factors, rather than due to structural damage (Ulmer, 2004; Bowden, 2018). An abnormally altered rate of cerebral blood flow may result from tumor-induced venous compression or neovascularity, causing abnormal BOLD signals (Holodny, 2000; Cho, 2018). Another possibility is related to blood oxygenation changes related to brain tumors. Brain tumors may cause atypical amounts of deoxygenated hemoglobin in the blood, resulting in a floor effect on the BOLD signal (Fujiwara, 2004). Lastly, brain tumor neovascularity, which is common in high-grade gliomas, can also lead to an

abnormally increased cerebral blood volume, which could then cause a ceiling effect on the BOLD signal (Hou, 2006).

Consistent with prior studies on the detection of NVU in task-fMRI activation maps, we performed our data analysis based on the assumption that the impact of pathology would be limited to the ipsilesional hemisphere. By comparing the activation pattern distributed in the ipsilesional hemisphere with that of analogous regions in the contralesional control hemisphere, altered activated areas were then attributed to pathology-induced NVU (Zaca, 2011; Zaca, 2012; Pillai, 2012; Pillai, 2014; Agarwal, 2017; Ulmer, 2004; Para, 2017; Pak, 2017). Nevertheless, of nine patients exhibiting atypical activation (i.e. nearly 70% of all patients), we only characterized five with NVU. Indeed, an asymmetrical activation pattern to a bilateral task in the presence of intact behavioral data could occur as a consequence of tumor-induced translocation of cortical tissue to perilesional areas (Zimmerman, 2019). The possibility of motor area translocation was supported by our results showing a superior-anterior shift of the activated area in a patient with GBM located at motor cortex (Fig. 4.6). It is also possible that an atypical activation pattern results from a reduction of brain cell density in infiltrating margins due to the tumor mass effect (Bowden, 2019). Importantly, our study also demonstrated a condition in which an asymmetrical task-fMRI activation pattern in terms of magnitude and extent was not characterized in peritumoral areas, but rather in areas distant from the tumor (Fig. 4.7). In such a case, the increased activation in the contralesional vs. ipsilesional hemisphere might be explained as an implied pseudo dominance induced by the tumor (Ulmer, 2004).

From the standpoint of clinical utility, it is important to note that when the task-fMRI activation is found to be abnormal, the examination of the resting-state CVR map would be helpful in understanding whether the CVR is also absent in the compromised task-fMRI activated area. A

lack of CVR in this situation would then suggest a potential for NVU. The behavioral and clinical data can potentially verify the occurrence of true NVU.

There were several limitations to this study. One limitation was the small size of the patient cohort, which caused low frequencies in each group of NVU classification. Follow-up studies would thus need a larger and more diverse patient population to further explore the sensitivity and specificity of resting-state CVRe maps as well as the potential impacts of tumor type and grade on incidences of NVU. Additionally, the current study utilized functional data from a bilateral lip-pursing task to determine the symmetry of intra-hemispheric activation within motor areas, but the representation of lip movement in motor cortex is relatively small. In the future, it would be favorable to employ a range of motor, language, and vision tasks to further study the potential ability of resting-state CVRe maps for detecting NVU in different brain areas. Another limitation was the lack of histopathological and post-surgical functional imaging data as well as detailed reports on patients' clinical examinations. Having these data would allow for a stronger claim about the potential NVU and, perhaps, contributing factors as well.

Conclusions

This study investigated the ability of resting-state CVRe metric of ALFF for detecting potential NVU in task-fMRI activation maps in patients with a brain tumor. While nearly 70% of patients exhibited atypical task-fMRI activation, only 38% of patients (i.e. five out of 13 patients) were identified with NVU. From these patients, the resting-state ALFF maps of four were able to detect false negatives due to impaired vascular function (i.e. "Late-stage NVU"). This accounts for nearly 31% of all patients. These results support the use of resting-state CVRe maps together

with presurgical task-fMRI brain mapping for image-guided neurosurgery, where caution must be taken for interpreting fMRI activation in peritumoral areas. More interestingly, this study provided evidence showing a potential for NVU in areas proximal to a tumor while the vascular ability to dilate remains intact (i.e. “Early-stage NVU)”. This highlights a need to set up appropriate behavioral tests to be used together with CVR mapping. Ultimately, more studies will need to be conducted to better understand NVU and to establish the sensitivity and specificity of resting-state CVRe maps in detecting clinical NVU.

V. Discussion

The Problem of NVU in Clinical Use of fMRI

The use of BOLD fMRI technique in image-guided neurosurgical planning has provided surgeons with new opportunities to reliably estimate the surgical proportions of affected tissue in the setting of various pathologic conditions such as tumors. However, as an indirect measure of neuronal activity, the BOLD effect makes the clinical task-fMRI activation maps vulnerable to false negatives due to NVU – i.e. a situation in which the neuro-vascular coupling mechanism is disturbed by focal pathology, but the local neurons remain intact. Such possibility precludes the reliable use of BOLD fMRI technique in isolation for neurosurgical planning because undetected NVU may be misinterpreted as non-functional tissue, leading to unintended surgical damage. Uncertainty about the interpretation of task-based activation maps poses a major impediment to successful integration of the BOLD fMRI technique into clinical practice. Therefore, to capitalize on the many advantages of using task-related fMRI in tumor resection planning, the widespread acceptance of this technique requires reliable detection of NVU.

Since 2014, BOLD-based CVR mapping through a breath-hold challenge has been nominally accepted as a method for detecting potential NVU. This method uses BOLD signal changes during breath holding vs. normal respiration to test the capacity of cerebral vessels to control the CBF as triggered by the breath-hold-induced elevation of blood CO_2. An identified region with vasoreactivity dysfunction can potentially be a site of NVU. This technique, however, has some drawbacks that impede its clinical use. Therefore, recent efforts have been made to map CVR in a passive fashion based on resting-state fMRI data. In this approach, presumably, the

BOLD signal fluctuations are induced by vasoreactivity to natural blood CO_2 variations during free breathing. Clinically, the use of resting-state BOLD fMRI signals is then of immense significance as the data are practically achievable for a broader range of patients. Yet, except for a few proof-of-principle studies, the effectiveness of resting-state-based technique for detecting potential NVU still needs to be validated.

Our Contributions to Existing Knowledge

This project was set up to establish the potential of the resting-state CVR metric as an imaging biomarker for detecting possible NVU. We pursued this goal by exploring the characteristics of resting-state CVR maps in terms of labeling and continuity to ascertain the extent to which they are similar to those of widely-accepted breath-hold CVR maps. We performed comparisons through a comprehensive treatment of thresholding and at a voxel level of resolution appropriate for presurgical brain mapping. We then chose an existing database of patients with a variety of brain tumors to evaluate the capability of resting-state CVR maps in identifying the NVU-related false negatives on task-fMRI activation maps as proof of concept.

The first phase of our project was to determine whether the newer estimate of CVR based on resting-state voxelwise data performs systematically in a manner similar to the more widely-accepted breath-hold CVR metric performs. We found an average accuracy of cross-metric correspondence of 73.6% after adjusting the threshold criteria for an optimally unbiased match. Consistent with discrepancies between the spatial patterns of two metrics observed on a voxel-wise basis, better coverage and segregation to gray matter tissue were found for the resting-state CVR maps in healthy individuals. Conversely, the breath-hold CVR maps revealed more

artifactual labeling of the white matter tissue. Of the spatial variations between the two CVR metrics, a percentage may be explained by the contributions of other physiological and/or neuronal factors that are not yet well known (Golestani, 2016; leopard, 2012; Tsvetanov, 2020). The relatively good cross-metric correspondence can perhaps be due to the same degree of influence from all these factors together and not necessarily due to CVR-related physiological components alone. While such a claim warrants further research, random noise is more likely to be a major contributor to variations in CVR patterns and the apparent dissimilarity between the two maps. The important role of random noise in CVR variants can also be inferred from our findings from the self-metric comparisons. The maximum obtainable self-concordance was relatively moderate for both metrics, with a significantly lower quantity for the breath-hold vs. resting-state metric. The breath-hold data are subject to contamination of motion artifacts that typically accompany an active task, which may account for its lower self-correspondence and the higher dispersion of its spatial pattern.

A key aspect of this study was the evaluation of thresholding effects on spatial characteristics of CVR maps. The cross-metric correspondence and their association with cortical gray matter were found to be strongly reliant on thresholding. Such a finding stresses the paramount importance of thresholding for an accurate interpretation of CVR maps. Indeed, our data demonstrated that the optimization of thresholding should not only maximize sensitivity for detecting true positives (i.e. CVR-present voxels in gray matter) but also decrease the concurrent effect of false negatives. Hence, particularly in the clinical setting, care should be taken in the adjustment of thresholds when using CVR maps, because a failure to balance the spread of true positives and false positives may obscure areas with compromised CVR.

Besides emphasizing the importance of thresholding, our thresholding approach, by itself, is of particular importance in the respect that it allowed us to compare CVR metrics with different units. Interestingly, our study showed that the optimized thresholds for an unbiased comparison of the two CVR patterns with each other closely corresponds to the two thresholds that optimally segregate the two CVR spatial patterns to gray vs. white matter. A likely explanation would then be that, perhaps, maximizing the spatial overlap of CVR vs. gray matter may optimize the CVR patterns to reflect the spatial distribution of vessels that give rise to valid CVR BOLD signals.

After investigating how well the two CVR metrics agreed in the labeling of the brain matter, it was then essential to determine the spatial characteristics of resting-state vs. breath-hold CVR maps in terms of continuity and uniformity. The basis of this study was established when the CVR maps optimized to gray matter tissue were shown to contain 'holes' in healthy individuals. Therefore, the capacity of resting-state vs. breath-hold CVR maps for revealing the foci of impaired CVR was determined in the second phase of this project. By exploring how unlikely it would be for different sizes of CVR hole to exist by chance, a trade-off basis was obtained for NVU-related decision making based on the possibility of a CVR hole being caused by random signal loss, but not NVU. The performance of such analyses to assess the spatial sampling statistics of CVR holes in healthy individuals becomes extremely important due to lack of information on the minimum size and the incidence chance of clinical NVU. In our five patient cases with suspected NVU, the size ranged 0.32 – 0.69 cm^3. While this is a small sample, it begins to show that the threshold of hole size based on random variation is less than observed suspected NVU in these cases.

The results from the resting-state vs. breath-hold CVR-hole analysis on healthy subjects brought out unexpected findings: the spatial sampling statistics of CVR holes were comparable

between the two metrics. In particular, the minimum CVR hole size with a maximum incidence risk of 5% identified as random signal loss was found identical and equal to 0.3 cm^3 for both metrics. Importantly, not only the probability distribution of CVR holes was found to be comparable between the two metrics of resting-state and breath-hold for a sample of individuals, but also between the resting-state CVR metric of two independent samples of individuals (our sample vs. Epilepsy Connectome Project's sample). Our findings suggest that perhaps the BOLD fluctuations during free breathing at rest reflect the CVR variations across the brain in a similar manner to those of induced through an active hypercapnic challenge. Accordingly, the resting-state CVR maps may have the same potential to interrogate the intactness of vasoreactivity as breath-hold CVR maps. Nevertheless, two important considerations should also be taken into account when interpreting these findings. First, although CVR maps are typically optimized for maximum coverage of gray matter areas, the gray matter optimization may not necessarily reveal CVR to its full potential. It is now well known that the distribution of vessels in gray matter is about 75% more than its adjacent white matter. Thus, it is likely that CVR not be entirely confined to gray matter. Second, in our CVR-holes analysis, the defined parameters for clustering and the estimations employed in the volume-surface mapping have potential to group the small-size holes together and artificially create relatively larger holes. Such possibility may somewhat hinder the differences between the two metrics in regard with the spatial sampling statistics of small-size holes, but also suggests that the minimum hole size with the maximum risk of 5% could be even less than 0.3 cm^3.

Our conclusion from the first two phases of this study is that the resting-state and breath-hold CVR metrics differ in the spatial pattern of holes' distribution (i.e. systematic manner) but coincide closely in regard to the extent to which the holes are likely to occur by chance (i.e.

statistical point). A plausible explanation which would cover both of these findings could be that both metrics arise from fluctuations in blood CO_2 levels, but the physiological vasodilatory mechanism contributing to each metric may be slightly different. For example, the temporal differences in blood CO_2 fluctuations induced actively by a breath-hold challenge vs. passively by free breathing at rest may cause each metric to reflect a different phase of cerebrovascular dynamics. Presumably, a longer time lag from the onset of breath-holding-induced changes in blood CO_2 could give sufficient time for extravascular CO_2 in the white matter tissue to build up and thereby to reach equilibrium with blood CO_2 in the microvasculature (Thomas, 2014). The optimization of overlapping between the breath-hold CVR metric and gray matter is thereby expected to come with more labeling of the white matter, when compared with the resting-state CVR metric that probably reflects the vasoreactivity to changes in blood CO_2 over considerably shorter time periods.

The first two phases of this project featured key findings on the spatial characteristics of CVR patterns. The next step was to validate the use of resting-state CVR maps for assessing the integrity of clinical fMRI activation in dealing with the problem of NVU. Therefore, a random cohort of patients with various types of brain tumors were put through a verification procedure in which the use of resting-state CVR maps was tested for detecting NVU in motor task-fMRI brain maps. We found that the absence of resting-state CVR metric was in spatial agreement with impaired BOLD activation within functionally-intact brain areas. This finding verified the effectiveness of resting-state CVR maps for detecting NVU-related fMRI signal dropouts in presurgical scenarios, suggesting that the intrinsic blood CO_2 fluctuations may be sufficient to act as a potent vasoactive agent and the resulting CVR is large enough for detecting tumor-induced vascular dysfunction.

Interestingly, we noticed that a brain area may still be susceptible to NVU, even in the setting of preserved CVR. Such a finding was not reported in any other study, and we did not have the expectation that the presence of a tumor causes NVU, but not have an impact on the regional CVR. We stress that CVR mapping only tests the intactness of vasoreactivity that is the last stage in the complex cascade of neuro-vascular coupling. However, if a tumor disrupts the coupling cascade at an earlier stage, such disruption may result in a situation in which the neurons in one end and the vessels in the other end remain functionally intact. To differentiate this scenario from the former, we used the terms "Early-stage NVU" vs. "Late-stage NVU." Although further studies are needed to assert this claim more robustly, "Early-stage NVU" can potentially be explained by neuro-astrocyte uncoupling due to tumor growth (Ulmer, 2004). Gliomas are also likely to interrupt the neuro-vascular coupling, as glioma cells have the potential to displace the astrocyte endfeet from the vasculature (Chow, 2016). Another possible explanation could be that the secreted factors of a tumor may change the inhibitory-excitatory balance of a brain region, thereby disturbing the coupling mechanisms while the neuro-vascular coupling components such as neurons and microvasculature remain functional (Gao, 2020).

Significance and Implications

In this study, we established the normative characteristics of resting-state CVR maps compared with those of breath-hold CVR maps at a voxel level of resolution similar to the level used for clinical brain mapping. Our methodological strategy was established to highlight the aspects of CVR mapping in current clinical practice that can be optimized and need to be fully appreciated by practitioners. As such, we developed a novel approach to address the ongoing, but often overlooked, issue of thresholding. We demonstrated that an arbitrary or poorly justified

threshold setting could result in a biased CVR map which may not accurately reveal the areas with compromised CVR.

Through three phases of this project, we investigated the suitability of resting-state CVR maps as an alternative to breath-hold CVR maps for detecting NVU-related task-fMRI signal dropouts. Our investigation was conducted from three different aspects: (1) spatial labeling of the brain, (2) continuity and uniformity, and (3) reliability of clinical use. The significantly more specific labeling of cortical gray matter by the resting-state CVR metric has a major implication that the resting-state technique may provide a comparative advantage over the breath-hold CVR metric for testing the integrity of task-fMRI activation maps. For the standpoint of clinical utility, a comparable capacity of the two CVR metrics to statistically allocate a hole to a site of potential NVU may also offer the use of resting-state due to its advantages in terms of the ease of use and computation. This study is the first that statistically outlines the degree of sensitivity of CVR maps in detecting potential NVU. From a clinical standpoint, due to uncertainty about the smallest possible size of clinical NVU, it becomes important to give each CVR hole size a statistical weight of occurrence in healthy subjects, thereby marking a margin where a hole could be less possible to be due to random noise and more likely to be potential NVU. Finally, this study presents evidence in support of the reliability of resting-state CVR maps to reveal foci of NVU in clinical task-based fMRI brain maps. To our knowledge, this is the first study that indicates a possible occurrence of NVU with no apparent effects on vascular function.

In sum, the findings of this study provide a strong base for the development of a population-wide applicable imaging marker to detect clinical fMRI signal dropouts caused by NVU. This will be a step towards the possibility of using of resting-state fMRI data to map both brain function and CVR, which is a fervent desire in the clinical setting.

Limitations and Future Research

There were several limitations to this study. An important limitation was lack of a through systematic investigation into the mechanisms that control CO_2-induced vasoreactivity within gray and white matter for the resting-state and breath-holding conditions. Such an investigation could play an important role in resolving ambiguity in observed discrepancies between the spatial labeling patterns of the two metrics. We also feel that a follow-up study considering other neuronal and/or vascular factors that may contribute to either metric may give us a detailed understanding of the origins of both metrics, in particular, the resting-state ALFF. Further research would then need to be carried out to investigate whether the CVR-related components of ALFF are independently affected by focal pathology.

A secondary important limitation of this study was that the cohort of patients used in this project lacked breath-hold task-related data. This would therefore leave to further investigation if the effects of brain tumors on resting-state CVR maps are similar to those of breath-hold CVR maps. Moreover, the data available for patients were only adequate to validate the effectiveness of resting-state CVR maps in the detection of NVU, not to develop a deep understanding of NVU. Thus, further meticulous research involving the systematic investigation of NVU as well as the study of pathology-induced changes in tissue based on the patients' histopathological data may help us to better understand the notion of NVU and thus clearly explain the association between the CVR and NVU.

Although the patient database used in this study covered a variety of NVU-related scenarios, the frequency of observed data was low for some categories in the patient classification

in respect of NVU. A relatively small number of patients with limited types of brain tumors in the current project clearly demonstrates the need for exploring the sensitivity and specificity of resting-state CVR maps on a larger and more diverse patient population. Additionally, despite having data from the hand-, foot-, and lip-movement tasks, our functional data analysis was limited to data from lip movements due to its bilateral hemispheric representation. Future studies should employ different tasks with appropriate behavioral and clinical tests to firmly establish the use of resting-state CVR maps for detecting NVU.

While many of the issues discussed above demand further detailed research, the recent interests in the translation of resting-state functional connectivity MRI into clinical care also characterizes an important area of investigation. That is to examine whether the resting-state CVR maps are able to reveal NVU in resting-state functional connectivity MRI maps. Such a study would then give us a more global perspective on the application of resting-state ALFF metrics for the detection of NVU.

Key Clinical Takeaways

Our results suggest that resting-state ALFF maps could be an alternative to breath-hold CVR maps for testing the integrity of task-fMRI brain activation in surgical planning, where caution must be taken for interpretating the data due to potential NVU. CVR mapping based on the resting-state data can circumvent the limitations of the breath-hold challenge, thereby giving clinicians the opportunity to assess the quality of brain maps with respect to NVU in a wider population of patients. In such a scenario, when a patient's task-fMRI activation map was not normal, a lack of resting-state ALFF in the suspected areas, which could not be random, would be

a warning to clinicians about the possibility for NVU. The use of resting-state CVR mapping for detecting NVU thus offers tremendous promise for accelerating the integration of fMRI into the clinical realm. Yet, more studies should be done to firmly establish the sensitivity and specificity, and thus, the clinical utility, of resting-state CVR maps in detecting NVU. Our study also highlighted the importance of thresholding in clinical use of CVR maps. Clinicians must be aware of the effects of arbitrary thresholding. An improper threshold setting may produce statistically biased CVR maps. For example, adjusting the threshold by increasing the sensitivity only to cortical gray matter may obscure the areas with compromised CVR. However, adjusting the threshold setting by maximizing the labeling of cortical gray matter vs. white matter may possibly provide a practical approach to reliably characterize the CVR activation patterns in clinical application.

VI. References

Agarwal, S., Airan, R., Gujar, S. K., Sair, H. I., & Pillai, J. J. (2015). *Calibration of BOLD fMRI motor activation maps using BOLD breath hold cerebrovascular reactivity mapping for effective compensation of brain tumor-related neurovascular uncoupling*.

Agarwal, S., Lu, H., & Pillai, J. J. (2017). Value of Frequency Domain Resting-State Functional Magnetic Resonance Imaging Metrics Amplitude of Low-Frequency Fluctuation and Fractional Amplitude of Low-Frequency Fluctuation in the Assessment of Brain Tumor-Induced Neurovascular Uncoupling. *Brain Connect, 7*(6), 382-389. doi:10.1089/brain.2016.0480

Agarwal, S., Sair, H. I., Airan, R., Hua, J., Jones, C. K., Heo, H. Y., . . . Pillai, J. J. (2016). Demonstration of Brain Tumor-Induced Neurovascular Uncoupling in Resting-State fMRI at Ultrahigh Field. *Brain Connect, 6*(4), 267-272.

Agarwal, S., Sair, H. I., Gujar, S., Hua, J., Lu, H., & Pillai, J. J. (2019). Functional Magnetic Resonance Imaging Activation Optimization in the Setting of Brain Tumor-Induced Neurovascular Uncoupling Using Resting-State Blood Oxygen Level-Dependent Amplitude of Low Frequency Fluctuations. *Brain Connect, 9*(3), 241-250. doi:10.1089/brain.2017.0562

Agarwal, S., Sair, H. I., Gujar, S. K., Hua, J., Lu, H., & Pillai, J. J. (2018). fMRI activation optimization in the setting of brain tumor-induced neurovascular uncoupling using resting state BOLD ALFF. *Brain Connect*. doi:10.1089/brain.2017.0562

Agarwal, S., Sair, H. I., & Pillai, J. J. (2017). Limitations of Resting-State Functional MR Imaging in the Setting of Focal Brain Lesions. *Neuroimaging Clinics of North America, 27*(4), 645-661.

Agarwal, S., Sair, H. I., & Pillai, J. J. (2021). The Problem of Neurovascular Uncoupling. *Neuroimaging Clin N Am, 31*(1), 53-67. doi:10.1016/j.nic.2020.09.003

Agarwal, S., Sair, H. I., Yahyavi-Firouz-Abadi, N., Airan, R., & Pillai, J. J. (2015). Neurovascular uncoupling in resting state fMRI demonstrated in patients with primary brain gliomas. *J Magn Reson Imaging*. doi:10.1002/jmri.25012

Amemiya, S., Kunimatsu, A., Saito, N., & Ohtomo, K. (2014). Cerebral hemodynamic impairment: assessment with resting-state functional MR imaging. *Radiology, 270*(2), 548-555. doi:10.1148/radiol.13130982

Aso, T., Jiang, G., Urayama, S.-I., & Fukuyama, H. (2017). A Resilient, Non-neuronal Source of the Spatiotemporal Lag Structure Detected by BOLD Signal-Based Blood Flow Tracking. *Front Neurosci, 11*, 256-256. doi:10.3389/fnins.2017.00256

Atlas, S. W., Howard, R. S., II, Maldjian, J., Alsop, D., Detre, J. A., Listerud, J., . . . Stecker, M. (1996). Functional Magnetic Resonance Imaging of Regional Brain Activity in Patients with Intracerebral Gliomas: Findings and Implications for Clinical Management. *Neurosurgery, 38*(2), 329-338. doi:10.1097/00006123-199602000-00019

Attwell, D., Buchan, A. M., Charpak, S., Lauritzen, M., Macvicar, B. A., & Newman, E. A. (2010). Glial and neuronal control of brain blood flow. *Nature, 468*(7321), 232-243. doi:10.1038/nature09613

Baig, M. A., Klein, J. P., & Mechtler, L. L. (2016). Imaging of Brain Tumors. *Continuum (Minneap Minn), 22*(5, Neuroimaging), 1529-1552. doi:10.1212/con.0000000000000388

Balthazar, M. L., Pereira, F. R., Lopes, T. M., da Silva, E. L., Coan, A. C., Campos, B. M., . . . Cendes, F. (2014). Neuropsychiatric symptoms in Alzheimer's disease are related to functional connectivity alterations in the salience network. *Hum Brain Mapp, 35*(4), 1237-1246. doi:10.1002/hbm.22248

Bandettini, P. A., & Wong, E. C. (1997). A hypercapnia-based normalization method for improved spatial localization of human brain activation with fMRI. *NMR in Biomedicine, 10*(4-5), 197-203. doi:10.1002/(sici)1099-1492(199706/08)10:4/5<197::aid-nbm466>3.0.co;2-s

Barone, D. G., Lawrie, T. A., & Hart, M. G. (2014). Image guided surgery for the resection of brain tumours. *The Cochrane database of systematic reviews, 2014*(1), CD009685-CD009685. doi:10.1002/14651858.CD009685.pub2

Biesecker, K. R., Srienc, A. I., Shimoda, A. M., Agarwal, A., Bergles, D. E., Kofuji, P., & Newman, E. A. (2016). Glial Cell Calcium Signaling Mediates Capillary Regulation of Blood Flow in the Retina. *J Neurosci, 36*(36), 9435-9445. doi:10.1523/jneurosci.1782-16.2016

Birn, R. M., Diamond, J. B., Smith, M. A., & Bandettini, P. A. (2006). Separating respiratory-variation-related fluctuations from neuronal-activity-related fluctuations in fMRI. *Neuroimage, 31*(4), 1536-1548.

Birn, R. M., Smith, M. A., Jones, T. B., & Bandettini, P. A. (2008). The respiration response function: the temporal dynamics of fMRI signal fluctuations related to changes in respiration. *Neuroimage, 40*(2), 644-654. doi:10.1016/j.neuroimage.2007.11.059

Biswal, B., Hudetz, A. G., Yetkin, F. Z., Haughton, V. M., & Hyde, J. S. (1997). Hypercapnia Reversibly Suppresses Low-Frequency Fluctuations in the Human Motor Cortex during Rest Using Echo–Planar MRI. *Journal of Cerebral Blood Flow & Metabolism, 17*(3), 301-308. doi:10.1097/00004647-199703000-00007

Biswal, B. B., Kannurpatti, S. S., & Rypma, B. (2007). Hemodynamic scaling of fMRI-BOLD signal: validation of low-frequency spectral amplitude as a scalability factor. *Magn Reson Imaging, 25*(10), 1358-1369. doi:10.1016/j.mri.2007.03.022

Biswal, B. B., Van Kylen, J., & Hyde, J. S. (1997). Simultaneous assessment of flow and BOLD signals in resting-state functional connectivity maps. *NMR Biomed, 10*(4-5), 165-170.

Black, D. F., Little, J. T., & Johnson, D. R. (2019). Neuroanatomical Considerations in Preoperative Functional Brain Mapping. *Topics in Magnetic Resonance Imaging, 28*(4), 213-224. doi:10.1097/RMR.0000000000000213

Black, D. F., Vachha, B., Mian, A., Faro, S. H., Maheshwari, M., Sair, H. I., . . . Welker, K. (2017). American Society of Functional Neuroradiology-Recommended fMRI Paradigm Algorithms for Presurgical Language Assessment. *AJNR Am J Neuroradiol, 38*(10), E65-e73. doi:10.3174/ajnr.A5345

Bright, M. G., & Murphy, K. (2013). Reliable quantification of BOLD fMRI cerebrovascular reactivity despite poor breath-hold performance. *Neuroimage, 83*, 559-568. doi:10.1016/j.neuroimage.2013.07.007

Burke, M., & Buhrle, C. (2006). BOLD response during uncoupling of neuronal activity and CBF. *Neuroimage, 32*(1), 1-8. doi:10.1016/j.neuroimage.2006.03.035

Catchlove, S. J., Parrish, T. B., Chen, Y., Macpherson, H., Hughes, M. E., & Pipingas, A. (2018). Regional Cerebrovascular Reactivity and Cognitive Performance in Healthy Aging. *Journal of experimental neuroscience, 12*, 1179069518785151-1179069518785151. doi:10.1177/1179069518785151

Cauli, B., Tong, X. K., Rancillac, A., Serluca, N., Lambolez, B., Rossier, J., & Hamel, E. (2004). Cortical GABA interneurons in neurovascular coupling: relays for subcortical vasoactive pathways. *J Neurosci, 24*(41), 8940-8949. doi:10.1523/jneurosci.3065-04.2004

Chang, C., & Glover, G. H. (2009). Relationship between respiration, end-tidal CO2, and BOLD signals in resting-state fMRI. *Neuroimage, 47*(4), 1381-1393. doi:10.1016/j.neuroimage.2009.04.048

Chen, B. R., Kozberg, M. G., Bouchard, M. B., Shaik, M. A., & Hillman, E. M. (2014). A critical role for the vascular endothelium in functional neurovascular coupling in the brain. *J Am Heart Assoc, 3*(3), e000787. doi:10.1161/jaha.114.000787

Chen, J. J. (2018). Cerebrovascular-Reactivity Mapping Using MRI: Considerations for Alzheimer's Disease. *Frontiers in Aging Neuroscience, 10*(170). doi:10.3389/fnagi.2018.00170

Chen, J. J., & Gauthier, C. J. (2021). The Role of Cerebrovascular-Reactivity Mapping in Functional MRI: Calibrated fMRI and Resting-State fMRI. *Frontiers in Physiology, 12*(361). doi:10.3389/fphys.2021.657362

Chen, Q., & Anderson, D. R. (1997). Effect of CO2 on intracellular pH and contraction of retinal capillary pericytes. *Invest Ophthalmol Vis Sci, 38*(3), 643-651.

Christen, T., Jahanian, H., Ni, W. W., Qiu, D., Moseley, M. E., & Zaharchuk, G. (2015). Noncontrast mapping of arterial delay and functional connectivity using resting-state functional MRI: a study in Moyamoya patients. *Journal of magnetic resonance imaging : JMRI, 41*(2), 424-430. doi:10.1002/jmri.24558

Chu, P. P. W., Golestani, A. M., Kwinta, J. B., Khatamian, Y. B., & Chen, J. J. (2018). Characterizing the modulation of resting-state fMRI metrics by baseline physiology. *Neuroimage, 173*, 72-87. doi:10.1016/j.neuroimage.2018.02.004

Cohen, A. D., & Wang, Y. (2019). Improving the Assessment of Breath-Holding Induced Cerebral Vascular Reactivity Using a Multiband Multi-echo ASL/BOLD Sequence. *Sci Rep, 9*(1), 5079-5079. doi:10.1038/s41598-019-41199-w

Cox, R. W. (1996). AFNI: Software for analysis and visualization of functional magnetic resonance neuroimages. *Computers and Biomedical Research, 29*, 162-173.

De Vis, J. B., Bhogal, A. A., Hendrikse, J., Petersen, E. T., & Siero, J. C. W. (2018). Effect sizes of BOLD CVR, resting-state signal fluctuations and time delay measures for the assessment of hemodynamic impairment in carotid occlusion patients. *Neuroimage, 179*, 530-539. doi:10.1016/j.neuroimage.2018.06.017.

DeYoe, E. A., & Raut, R. V. (2014). Visual Mapping Using Blood Oxygen Level Dependent Functional Magnetic Resonance Imaging. *Neuroimaging Clin N Am, 24*(4), 573-584. doi:10.1016/j.nic.2014.08.001

DeYoe, E. A., & Ulmer, J. (2005).

DeYoe, E. A., Ulmer, J. L., Mathis, J. R., & Mueller, W. (2014). *Advanced Neuroimaging Tools for Planning/Guiding Occipital Lobe Surgery*. Paper presented at the ASNR, Montreal.

DeYoe, E. A., Ulmer, J. L., Mueller, W. M., Sabsevitz, D. S., Reitsma, D. C., & Pillai, J. J. (2015). Imaging of the Functional and Dysfunctional Visual System. *Semin Ultrasound CT MR, 36*(3), 234-248. doi:10.1053/j.sult.2015.05.015

Di, X., Kannurpatti, S. S., Rypma, B., & Biswal, B. B. (2013). Calibrating BOLD fMRI activations with neurovascular and anatomical constraints. *Cereb Cortex, 23*(2), 255-263. doi:10.1093/cercor/bhs001

Donahue, M. J., Stevens, R. D., de Boorder, M., Pekar, J. J., Hendrikse, J., & van Zijl, P. C. M. (2009). Hemodynamic Changes Following Visual Stimulation and Breath-holding Provide Evidence for an Uncoupling of Cerebral Blood Flow and Volume from Oxygen Metabolism. *Journal of cerebral blood flow and metabolism : official journal of the International Society of Cerebral Blood Flow and Metabolism, 29*(1), 176-185. doi:10.1038/jcbfm.2008.109

Duarte, J. V., Pereira, J. M. S., Quendera, B., Raimundo, M., Moreno, C., Gomes, L., . . . Castelo-Branco, M. (2015). Early disrupted neurovascular coupling and changed event level hemodynamic response function in type 2 diabetes: an fMRI study. *Journal of cerebral blood flow and metabolism : official journal of the International Society of Cerebral Blood Flow and Metabolism, 35*(10), 1671-1680. doi:10.1038/jcbfm.2015.106

Duvernoy, H. M., Delon, S., & Vannson, J. L. (1981). Cortical blood vessels of the human brain. *Brain Research Bulletin, 7*, 519-579.

El-Bouri, W. K., & Payne, S. J. (2016). A statistical model of the penetrating arterioles and venules in the human cerebral cortex. *Microcirculation, 23*(7), 580-590. doi:10.1111/micc.12318

Fierstra, J., Sobczyk, O., Battisti-Charbonney, A., Mandell, D. M., Poublanc, J., Crawley, A. P., . . . Fisher, J. A. (2013). Measuring cerebrovascular reactivity: what stimulus to use? *J Physiol, 591*(Pt 23), 5809-5821. doi:10.1113/jphysiol.2013.259150

Fierstra, J., van Niftrik, C., Warnock, G., Wegener, S., Piccirelli, M., Pangalu, A., . . . Regli, L. (2018). Staging Hemodynamic Failure With Blood Oxygen-Level-Dependent Functional Magnetic Resonance Imaging Cerebrovascular Reactivity: A Comparison Versus Gold Standard ((15)O-)H2O-Positron Emission Tomography. *Stroke, 49*(3), 621-629. doi:10.1161/strokeaha.117.020010

Fisher, J. A., & Mikulis, D. J. (2021). Cerebrovascular Reactivity: Purpose, Optimizing Methods, and Limitations to Interpretation – A Personal 20-Year Odyssey of (Re)searching. *Frontiers in Physiology, 12*(420). doi:10.3389/fphys.2021.629651

Fisher, J. A., Venkatraghavan, L., & Mikulis, D. J. (2018). Magnetic Resonance Imaging-Based Cerebrovascular Reactivity and Hemodynamic Reserve: A Review of Method Optimization and Data Interpretation. *Stroke*. doi:10.1161/strokeaha.118.021012

Fujiwara, N., Sakatani, K., Katayama, Y., Murata, Y., Hoshino, T., Fukaya, C., & Yamamoto, T. (2004). Evoked-cerebral blood oxygenation changes in false-negative activations in BOLD contrast functional MRI of patients with brain tumors. *Neuroimage, 21*(4), 1464-1471.

Genetti, M., Grouiller, F., Vulliemoz, S., Spinelli, L., Seeck, M., Michel, C. M., & Schaller, K. (2013). Noninvasive language mapping in patients with epilepsy or brain tumors. *Neurosurgery, 72*(4), 555-565. doi:10.1227/NEU.0b013e318282cdad

Girouard, H., & Iadecola, C. (2006). Neurovascular coupling in the normal brain and in hypertension, stroke, and Alzheimer disease. *J Appl Physiol, 100*(1), 328-335.

Glover, G. H. (2011). Overview of functional magnetic resonance imaging. *Neurosurgery clinics of North America, 22*(2), 133-vii. doi:10.1016/j.nec.2010.11.001

Golestani, A. M., Chang, C., Kwinta, J. B., Khatamian, Y. B., & Chen, J. J. (2015). Mapping the end-tidal CO2 response function in the resting-state BOLD fMRI signal: spatial specificity, test-retest reliability and effect of fMRI sampling rate. *Neuroimage, 104*, 266-277. doi:10.1016/j.neuroimage.2014.10.031

Golestani, A. M., Kwinta, J. B., Khatamian, Y. B., & Chen, J. J. (2017). The Effect of Low-Frequency Physiological Correction on the Reproducibility and Specificity of Resting-State fMRI Metrics: Functional Connectivity, ALFF, and ReHo. *Front Neurosci, 11*, 546. doi:10.3389/fnins.2017.00546

Golestani, A. M., Kwinta, J. B., Strother, S. C., Khatamian, Y. B., & Chen, J. J. (2016). The association between cerebrovascular reactivity and resting-state fMRI functional connectivity in healthy adults: The influence of basal carbon dioxide. *Neuroimage, 132*, 301-313. doi:10.1016/j.neuroimage.2016.02.051

Golestani, A. M., Wei, L. L., & Chen, J. J. (2016). Quantitative Mapping of Cerebrovascular Reactivity using Resting-state BOLD fMRI: Validation in Healthy Adults. *Neuroimage, 138*, 147-163. doi:10.1016/j.neuroimage.2016.05.025

Gorgolewski, K. J., Storkey, A., Bastin, M. E., Whittle, I. R., Wardlaw, J. M., & Pernet, C. R. (2013). A test-retest fMRI dataset for motor, language and spatial attention functions. *GigaScience, 2*(1). doi:10.1186/2047-217x-2-6

Gorgolewski, K. J., Storkey, A. J., Bastin, M. E., & Pernet, C. R. (2012). Adaptive thresholding for reliable topological inference in single subject fMRI analysis. *Front Hum Neurosci, 6*, 245. doi:10.3389/fnhum.2012.00245

Gorgolewski, K. J., Storkey, A. J., Bastin, M. E., Whittle, I., & Pernet, C. (2013). Single subject fMRI test–retest reliability metrics and confounding factors. *Neuroimage, 69*, 231-243. doi:https://doi.org/10.1016/j.neuroimage.2012.10.085

Gorman, J. M., Kent, J., Martinez, J., Browne, S., Coplan, J., & Papp, L. A. (2001). Physiological Changes During Carbon Dioxide Inhalation in Patients With Panic Disorder, Major Depression, and Premenstrual Dysphoric Disorder: Evidence for a Central Fear Mechanism. *JAMA Psychiatry, 58*(2), 125-131. doi:10.1001/archpsyc.58.2.125

Gould, I. G., Tsai, P., Kleinfeld, D., & Linninger, A. (2017). The capillary bed offers the largest hemodynamic resistance to the cortical blood supply. *Journal of Cerebral Blood Flow & Metabolism, 37*(1), 52-68. doi:10.1177/0271678x16671146

Guerra, G., Lucariello, A., Perna, A., Botta, L., De Luca, A., & Moccia, F. (2018). The Role of Endothelial Ca(2+) Signaling in Neurovascular Coupling: A View from the Lumen. *International journal of molecular sciences, 19*(4), 938. doi:10.3390/ijms19040938

Hall, C. N., Howarth, C., Kurth-Nelson, Z., & Mishra, A. (2016). Interpreting BOLD: towards a dialogue between cognitive and cellular neuroscience. *Philosophical Transactions of the Royal Society B: Biological Sciences, 371*(1705), 20150348. doi:10.1098/rstb.2015.0348

Hall, C. N., Reynell, C., Gesslein, B., Hamilton, N. B., Mishra, A., Sutherland, B. A., . . . Attwell, D. (2014). Capillary pericytes regulate cerebral blood flow in health and disease. *Nature, 508*(7494), 55-60. doi:10.1038/nature13165

Hamilton, N. B., Attwell, D., & Hall, C. N. (2010). Pericyte-mediated regulation of capillary diameter: a component of neurovascular coupling in health and disease. *Front Neuroenergetics, 2*. doi:10.3389/fnene.2010.00005

Hart, J., Jr., Rao, S. M., & Nuwer, M. (2007). Clinical functional magnetic resonance imaging. *Cogn Behav Neurol, 20*(3), 141-144. doi:10.1097/WNN.0b013e31812570e2

Hillman, E. M. (2014). Coupling Mechanism and Significance of the BOLD Signal: A Status Report. *Annu Rev Neurosci, 37*, 161-181. doi:10.1146/annurev-neuro-071013-014111

Hirsch, J., Ruge, M. I., Kim, K. H., Correa, D. D., Victor, J. D., Relkin, N. R., . . . Gutin, P. H. (2000). An integrated functional magnetic resonance imaging procedure for preoperative mapping of cortical areas associated with tactile, motor, language, and visual functions. *Neurosurgery, 47*(3), 711-721; discussion 721-712. doi:10.1097/00006123-200009000-00037

Holmes, C. J., Hoge, R., Collins, L., Woods, R., Toga, A. W., & Evans, A. C. (1998). Enhancement of MR images using registration for signal averaging. *J Comput Assist Tomogr, 22*(2), 324-333. doi:10.1097/00004728-199803000-00032

Holodny, A. I., Schulder, M., Liu, W. C., Wolko, J., Maldjian, J. A., & Kalnin, A. J. (2000). The effect of brain tumors on BOLD functional MR imaging activation in the adjacent motor cortex: implications for image-guided neurosurgery. *AJNR Am J Neuroradiol, 21*(8), 1415-1422.

Hou, B. L., Bradbury, M., Peck, K. K., Petrovich, N. M., Gutin, P. H., & Holodny, A. I. (2006). Effect of brain tumor neovasculature defined by rCBV on BOLD fMRI activation volume in the primary motor cortex. *Neuroimage, 32*(2), 489-497. doi:10.1016/j.neuroimage.2006.04.188

Hsu, Y. Y., Chang, C. N., Jung, S. M., Lim, K. E., Huang, J. C., Fang, S. Y., & Liu, H. L. (2004). Blood oxygenation level-dependent MRI of cerebral gliomas during breath holding. *J Magn Reson Imaging, 19*(2), 160-167.

Huneau, C., Benali, H., & Chabriat, H. (2015). Investigating Human Neurovascular Coupling Using Functional Neuroimaging: A Critical Review of Dynamic Models. *Front Neurosci, 9*(467).

Iranmahboob, A., Peck, K. K., Brennan, N. P., Karimi, S., Fisicaro, R., Hou, B., & Holodny, A. I. (2016). Vascular Reactivity Maps in Patients with Gliomas Using Breath-Holding BOLD fMRI. *J Neuroimaging, 26*(2), 232-239. doi:10.1111/jon.12278

Jahanian, H., Christen, T., Moseley, M. E., Pajewski, N. M., Wright, C. B., Tamura, M. K., & Zaharchuk, G. (2017). Measuring vascular reactivity with resting-state blood oxygenation level-dependent (BOLD) signal fluctuations: A potential alternative to the breath-holding challenge? *J Cereb Blood Flow Metab, 37*(7), 2526-2538. doi:10.1177/0271678X16670921

Jahanian, H., Christen, T., Moseley, M. E., & Zaharchuk, G. (2018). Erroneous Resting-State fMRI Connectivity Maps Due to Prolonged Arterial Arrival Time and How to Fix Them. *Brain Connectivity, 8*(6), 362-370. doi:10.1089/brain.2018.0610

Jahanian, H., Ni, W. W., Christen, T., Moseley, M. E., Kurella Tamura, M., & Zaharchuk, G. (2014). Spontaneous BOLD signal fluctuations in young healthy subjects and elderly patients with chronic kidney disease. *PLoS ONE, 9*(3), e92539. doi:10.1371/journal.pone.0092539

Janecek, J. K., Swanson, S. J., Sabsevitz, D. S., Hammeke, T. A., Raghavan, M., M, E. R., & Binder, J. R. (2013). Language lateralization by fMRI and Wada testing in 229 patients with epilepsy: rates and predictors of discordance. *Epilepsia, 54*(2), 314-322. doi:10.1111/epi.12068

Jenkinson, M. D., Barone, D., Bryant, A., Vale, L., Bulbeck, H., Lawrie, T. A., . . . Watts, C. (2018). Intraoperative imaging technology to maximise extent of resection for glioma. *Cochrane Database of Systematic Reviews*(1). doi:10.1002/14651858.CD012788.pub2

Jiang, Z., Krainik, A., David, O., Salon, C., Troprès, I., Hoffmann, D., . . . Le Bas, J. F. (2010). Impaired fMRI activation in patients with primary brain tumors. *Neuroimage, 52*(2), 538-548. doi:10.1016/j.neuroimage.2010.04.194

Kalcher, K., Boubela, R. N., Huf, W., Biswal, B. B., Baldinger, P., Sailer, U., . . . Windischberger, C. (2013). RESCALE: Voxel-specific task-fMRI scaling using resting state fluctuation amplitude. *Neuroimage, 70*, 80-88. doi:https://doi.org/10.1016/j.neuroimage.2012.12.019

Kannurpatti, S. S., & Biswal, B. B. (2008). Detection and scaling of task-induced fMRI-BOLD response using resting state fluctuations. *Neuroimage, 40*(4), 1567-1574. doi:10.1016/j.neuroimage.2007.09.040

Kannurpatti, S. S., Motes, M. A., Biswal, B. B., & Rypma, B. (2014). Assessment of unconstrained cerebrovascular reactivity marker for large age-range FMRI studies. *PLoS ONE, 9*(2), e88751. doi:10.1371/journal.pone.0088751

Kannurpatti, S. S., Motes, M. A., Rypma, B., & Biswal, B. B. (2010). Neural and vascular variability and the fMRI-BOLD response in normal aging. *Magn Reson Imaging, 28*(4), 466-476. doi:10.1016/j.mri.2009.12.007

Kannurpatti, S. S., Motes, M. A., Rypma, B., & Biswal, B. B. (2011). Increasing measurement accuracy of age-related BOLD signal change: minimizing vascular contributions by resting-state-fluctuation-of-amplitude scaling. *Hum Brain Mapp, 32*(7), 1125-1140. doi:10.1002/hbm.21097

Kastrup, A., Kruger, G., Glover, G. H., & Moseley, M. E. (1999). Assessment of cerebral oxidative metabolism with breath holding and fMRI. *Magn Reson Med, 42*(3), 608-611.

Kastrup, A., Kruger, G., Neumann-Haefelin, T., & Moseley, M. E. (2001). Assessment of cerebrovascular reactivity with functional magnetic resonance imaging: comparison of CO(2) and breath holding. *Magn Reson Imaging, 19*(1), 13-20.

Kastrup, A., Li, T. Q., Glover, G. H., & Moseley, M. E. (1999). Cerebral blood flow-related signal changes during breath-holding. *AJNR Am J Neuroradiol, 20*(7), 1233-1238.

Khalil, A. A., Ostwaldt, A.-C., Nierhaus, T., Ganeshan, R., Audebert, H. J., Villringer, K., . . . Fiebach, J. B. (2017). Relationship Between Changes in the Temporal Dynamics of the Blood-Oxygen-Level-Dependent Signal and Hypoperfusion in Acute Ischemic Stroke. *Stroke, 48*(4), 925-931. doi:doi:10.1161/STROKEAHA.116.015566

Kisler, K., Nelson, A. R., Rege, S. V., Ramanathan, A., Wang, Y., Ahuja, A., . . . Zlokovic, B. V. (2017). Pericyte degeneration leads to neurovascular uncoupling and limits oxygen supply to brain. *Nature Neuroscience, 20*, 406. doi:10.1038/nn.4489

https://www.nature.com/articles/nn.4489#supplementary-information

Kumar, V. A., Heiba, I. M., Prabhu, S. S., Chen, M. M., Colen, R. R., Young, A. L., . . . Liu, H.-L. (2020). The role of resting-state functional MRI for clinical preoperative language mapping. *Cancer Imaging, 20*(1), 47. doi:10.1186/s40644-020-00327-w

Kwong, K. K., Belliveau, J., W., Stern, C. E., Chesler, D. A., Goldberg, I. E., Poncelet, B. P., . . . Rosen, B. R. (1992). Functional MR imaging of primary visual and motor cortex. *Journal of Magnetic Resonance Imaging, 2P*, 76.

Laine, J. F., Slama, M., Petitpretz, P., Girard, P., & Motte, G. (1986). Danger of vasodilator therapy for pulmonary hypertension in patent foramen ovale. *Chest, 89*(6), 894-895. doi:10.1378/chest.89.6.894

Laurent, D., Freedman, R., Cope, L., Sacks, P., Abbatematteo, J., Kubilis, P., . . . Rahman, M. (2019). Impact of Extent of Resection on Incidence of Postoperative Complications in Patients With Glioblastoma. *Neurosurgery*. doi:10.1093/neuros/nyz313

Lee, J., Lund-Smith, C., Borboa, A., Gonzalez, A. M., Baird, A., & Eliceiri, B. P. (2009). Glioma-induced remodeling of the neurovascular unit. *Brain Res, 1288*, 125-134. doi:10.1016/j.brainres.2009.06.095

Leung, J., Duffin, J., Fisher, J. A., & Kassner, A. (2016). MRI-based cerebrovascular reactivity using transfer function analysis reveals temporal group differences between patients with sickle cell disease and healthy controls. *Neuroimage Clin, 12*, 624-630. doi:10.1016/j.nicl.2016.09.009

Li, T. Q., Kastrup, A., Takahashi, A. M., & Moseley, M. E. (1999). Functional MRI of human brain during breath holding by BOLD and FAIR techniques. *Neuroimage, 9*(2), 243-249. doi:10.1006/nimg.1998.0399

Lipp, I., Murphy, K., Caseras, X., & Wise, R. G. (2015). Agreement and repeatability of vascular reactivity estimates based on a breath-hold task and a resting state scan. *Neuroimage, 113*, 387-396. doi:10.1016/j.neuroimage.2015.03.004

Liu, P., De Vis, J. B., & Lu, H. (2019). Cerebrovascular reactivity (CVR) MRI with CO2 challenge: A technical review. *Neuroimage, 187*, 104-115. doi:10.1016/j.neuroimage.2018.03.047

Liu, P., Li, Y., Pinho, M., Park, D. C., Welch, B. G., & Lu, H. (2017). Cerebrovascular reactivity mapping without gas challenges. *Neuroimage, 146*(Supplement C), 320-326. doi:10.1016/j.neuroimage.2016.11.054

Liu, P., Liu, G., Pinho, M. C., Lin, Z., Thomas, B. P., Rundle, M., . . . Lu, H. (2021). Cerebrovascular Reactivity Mapping Using Resting-State BOLD Functional MRI in Healthy Adults and Patients with Moyamoya Disease. *Radiology, 0*(0), 203568. doi:10.1148/radiol.2021203568

Liu, P., Xu, C., Lin, Z., Sur, S., Li, Y., Yasar, S., . . . Lu, H. (2020). Cerebrovascular reactivity mapping using intermittent breath modulation. *Neuroimage, 215*, 116787. doi:https://doi.org/10.1016/j.neuroimage.2020.116787

Lu, H., Law, M., Johnson, G., Ge, Y., van Zijl, P. C., & Helpern, J. A. (2005). Novel approach to the measurement of absolute cerebral blood volume using vascular-space-occupancy magnetic resonance imaging. *Magn Reson Med, 54*(6), 1403-1411. doi:10.1002/mrm.20705

Lu, H., Liu, P., Yezhuvath, U., Cheng, Y., Marshall, O., & Ge, Y. (2014). MRI mapping of cerebrovascular reactivity via gas inhalation challenges. *J Vis Exp*(94), 52306. doi:10.3791/52306

Lythgoe, D. J., Williams, S. C. R., Cullinane, M., & Markus, H. S. (1999). Mapping of cerebrovascular reactivity using bold magnetic resonance imaging. *Magnetic Resonance Imaging, 17*(4), 495-502. doi:https://doi.org/10.1016/S0730-725X(98)00211-2

Madden, J. A. (1993). The effect of carbon dioxide on cerebral arteries. *Pharmacol Ther, 59*(2), 229-250.

Makedonov, I., Black, S. E., & Macintosh, B. J. (2013). BOLD fMRI in the white matter as a marker of aging and small vessel disease. *PLoS ONE, 8*(7), e67652-e67652. doi:10.1371/journal.pone.0067652

Mandell, D. M., Han, J. S., Poublanc, J., Crawley, A. P., Stainsby, J. A., Fisher, J. A., & Mikulis, D. J. (2008). Mapping cerebrovascular reactivity using blood oxygen level-dependent MRI in Patients with arterial steno-occlusive disease: comparison with arterial spin labeling MRI. *Stroke, 39*(7), 2021-2028.

Mazerolle, E. L., Ma, Y., Sinclair, D., & Pike, G. B. (2018). Impact of abnormal cerebrovascular reactivity on BOLD fMRI: a preliminary investigation of moyamoya disease. *Clin Physiol Funct Imaging, 38*(1), 87-92. doi:10.1111/cpf.12387

Mazziotta, J. C., Toga, A. W., Evans, A., Fox, P., & Lancaster, J. (1995). A probabilistic atlas of the human brain: theory and rationale for its development. The International Consortium for Brain Mapping (ICBM). *Neuroimage, 2*(2), 89-101.

McGirt, M. J., Mukherjee, D., Chaichana, K. L., Than, K. D., Weingart, J. D., & Quinones-Hinojosa, A. (2009). ASSOCIATION OF SURGICALLY ACQUIRED MOTOR AND LANGUAGE DEFICITS ON OVERALL SURVIVAL AFTER RESECTION OF GLIOBLASTOMA MULTIFORME. *Neurosurgery, 65*(3), 463-470. doi:10.1227/01.neu.0000349763.42238.e9

Mikulis, D. J. (2013). Chronic Neurovascular Uncoupling Syndrome. *Stroke, 44*(6_suppl_1), S55-S57. doi:10.1161/STROKEAHA.113.001081

Miller, K. B., Howery, A. J., Rivera-Rivera, L. A., Johnson, S. C., Rowley, H. A., Wieben, O., & Barnes, J. N. (2019). Age-Related Reductions in Cerebrovascular Reactivity Using 4D Flow MRI. *Frontiers in Aging Neuroscience, 11*, 281-281. doi:10.3389/fnagi.2019.00281

Moreton, F. C., Dani, K. A., Goutcher, C., O'Hare, K., & Muir, K. W. (2016). Respiratory challenge MRI: Practical aspects. *Neuroimage: Clinical, 11*, 667-677. doi:https://doi.org/10.1016/j.nicl.2016.05.003

Murphy, K., Harris, A. D., & Wise, R. G. (2011). Robustly measuring vascular reactivity differences with breath-hold: normalising stimulus-evoked and resting state BOLD fMRI data. *Neuroimage, 54*(1), 369-379. doi:10.1016/j.neuroimage.2010.07.059

Ni, L., Li, J., Li, W., Zhou, F., Wang, F., Schwarz, C. G., . . . Xu, Y. (2017). The value of resting-state functional MRI in subacute ischemic stroke: comparison with dynamic susceptibility contrast-enhanced perfusion MRI. *Sci Rep, 7*, 41586. doi:10.1038/srep41586

Nippert, A. R., Biesecker, K. R., & Newman, E. A. (2018). Mechanisms Mediating Functional Hyperemia in the Brain. *The Neuroscientist : a review journal bringing neurobiology, neurology and psychiatry, 24*(1), 73-83. doi:10.1177/1073858417703033

Nishida, S., Aso, T., Takaya, S., Takahashi, Y., Kikuchi, T., Funaki, T., . . . Miyamoto, S. (2018). Resting-state Functional Magnetic Resonance Imaging Identifies Cerebrovascular Reactivity Impairment in Patients With Arterial Occlusive Diseases: A Pilot Study. *Neurosurgery*. doi:10.1093/neuros/nyy434

Ogawa, S., Lee, T. M., Kay, A. R., & Tank, D. W. (1990). Brain magnetic resonance imaging with contrast dependent on blood oxygenation. *Proceedings of the National Academy of Sciences of the United States of America, 87*(24), 9868-9872.

Ogawa, S., Lee, T. M., Kay, A. R., & Tank, D. W. (1990). Brain magnetic resonance imaging with contrast dependent on blood oxygenation. *Proceedings of the National Academy of Sciences USA, 87*, 9868-9872.

Ojemann, G. A. (1993). Functional mapping of cortical language areas in adults. Intraoperative approaches. *Advances in neurology, 63*, 155-163.

Orringer, D. A., Vago, D. R., & Golby, A. J. (2012). Clinical applications and future directions of functional MRI. *Seminars in Neurology, 32*(4), 466-475. doi:10.1055/s-0032-1331816

Ostrom, Q. T., Patil, N., Cioffi, G., Waite, K., Kruchko, C., & Barnholtz-Sloan, J. S. (2020). CBTRUS Statistical Report: Primary Brain and Other Central Nervous System Tumors Diagnosed in the United States in 2013-2017. *Neuro Oncol, 22*(12 Suppl 2), iv1-iv96. doi:10.1093/neuonc/noaa200

Pak, R. W., Hadjiabadi, D. H., Senarathna, J., Agarwal, S., Thakor, N. V., Pillai, J. J., & Pathak, A. P. (2017). Implications of neurovascular uncoupling in functional magnetic resonance imaging (fMRI) of brain tumors. *J Cereb Blood Flow Metab, 37*(11), 3475-3487. doi:10.1177/0271678x17707398

Para, A. E., Sam, K., Poublanc, J., Fisher, J. A., Crawley, A. P., & Mikulis, D. J. (2017). Invalidation of fMRI experiments secondary to neurovascular uncoupling in patients with cerebrovascular disease. *Journal of Magnetic Resonance Imaging, 46*(5), 1448-1455. doi:10.1002/jmri.25639

Peacock, J., Black, D., DeLone, D., & Welker, K. (2016). Use of a Simple Breath-Holding Task for Cerebrovascular Reactivity Scans in Clinical Functional MR Imaging. *Neurographics, 6*, 213-218. doi:10.3174/ng.4160161

Pernet, C. R., Gorgolewski, K. J., Job, D., Rodriguez, D., Whittle, I., & Wardlaw, J. (2016). A structural and functional magnetic resonance imaging dataset of brain tumour patients. *Scientific Data, 3*(1), 160003. doi:10.1038/sdata.2016.3

Petrella, J. R., Shah, L. M., Harris, K. M., Friedman, A. H., George, T. M., Sampson, J. H., . . . Voyvodic, J. T. (2006). Preoperative functional MR imaging localization of language and motor areas: effect on therapeutic decision making in patients with potentially resectable brain tumors. *Radiology, 240*(3), 793-802. doi:10.1148/radiol.2403051153

Pillai, J. J. (2010). The evolution of clinical functional imaging during the past 2 decades and its current impact on neurosurgical planning. *AJNR Am J Neuroradiol, 31*(2), 219-225. doi:10.3174/ajnr.A1845

Pillai, J. J., & Mikulis, D. J. (2014). Cerebrovascular Reactivity Mapping: An Evolving Standard for Clinical Functional Imaging. *AJNR Am J Neuroradiol*. doi:10.3174/ajnr.A3941

Pillai, J. J., & Zaca, D. (2011). Clinical utility of cerebrovascular reactivity mapping in patients with low grade gliomas. *World J Clin Oncol, 2*(12), 397-403. doi:10.5306/wjco.v2.i12.397.

Pillai, J. J., & Zaca, D. (2012). Comparison of BOLD Cerebrovascular Reactivity Mapping and DSC MR Perfusion Imaging for Prediction of Neurovascular Uncoupling Potential in Brain Tumors. *Technol Cancer Res Treat*.

Pineiro, R., Pendlebury, S., Johansen-Berg, H., & Matthews, P. M. (2002). Altered hemodynamic responses in patients after subcortical stroke measured by functional MRI. *Stroke, 33*(1), 103-109.

Pinto, J., Bright, M. G., Bulte, D. P., & Figueiredo, P. (2021). Cerebrovascular Reactivity Mapping Without Gas Challenges: A Methodological Guide. *Frontiers in Physiology, 11*(1711). doi:10.3389/fphys.2020.608475

Pinto, J., Jorge, J., Sousa, I., Vilela, P., & Figueiredo, P. (2016). Fourier modeling of the BOLD response to a breath-hold task: Optimization and reproducibility. *Neuroimage, 135*, 223-231. doi:10.1016/j.neuroimage.2016.02.037

Rahman, M., Abbatematteo, J., De Leo, E. K., Kubilis, P. S., Vaziri, S., Bova, F., . . . Quinones-Hinojosa, A. (2016). The effects of new or worsened postoperative neurological deficits on survival of patients with glioblastoma. *127*(1), 123. doi:10.3171/2016.7.jns16396

Sanai, N., Polley, M. Y., McDermott, M. W., Parsa, A. T., & Berger, M. S. (2011). An extent of resection threshold for newly diagnosed glioblastomas. *J Neurosurg, 115*(1), 3-8. doi:10.3171/2011.2.jns10998

Scouten, A., & Schwarzbauer, C. (2008). Paced respiration with end-expiration technique offers superior BOLD signal repeatability for breath-hold studies. *Neuroimage, 43*(2), 250-257. doi:https://doi.org/10.1016/j.neuroimage.2008.03.052

Siegel, R. L., Miller, K. D., & Jemal, A. (2019). Cancer statistics, 2019. *CA: A Cancer Journal for Clinicians, 69*(1), 7-34. doi:doi:10.3322/caac.21551

Silva, M. A., See, A. P., Essayed, W. I., Golby, A. J., & Tie, Y. (2018). Challenges and techniques for presurgical brain mapping with functional MRI. *Neuroimage Clin, 17*, 794-803. doi:10.1016/j.nicl.2017.12.008

Spano, V. R., Mandell, D. M., Poublanc, J., Sam, K., Battisti-Charbonney, A., Pucci, O., . . . Mikulis, D. J. (2013). CO2 blood oxygen level-dependent MR mapping of cerebrovascular reserve in a clinical

population: safety, tolerability, and technical feasibility. *Radiology, 266*(2), 592-598. doi:10.1148/radiol.12112795

Stanimirovic, D. B., & Friedman, A. (2012). Pathophysiology of the neurovascular unit: disease cause or consequence? *J Cereb Blood Flow Metab, 32*(7), 1207-1221. doi:10.1038/jcbfm.2012.25

Stock, M., Kontrisova, K., Dieckmann, K., Bogner, J., Poetter, R., & Georg, D. (2006). Development and application of a real-time monitoring and feedback system for deep inspiration breath hold based on external marker tracking. *Med Phys, 33*(8), 2868-2877. doi:10.1118/1.2219775

Stummer, W., Reulen, H. J., Meinel, T., Pichlmeier, U., Schumacher, W., Tonn, J. C., . . . Pietsch, T. (2008). Extent of resection and survival in glioblastoma multiforme: identification of and adjustment for bias. *Neurosurgery, 62*(3), 564-576; discussion 564-576. doi:10.1227/01.neu.0000317304.31579.17

Szaflarski, J. P., Gloss, D., Binder, J. R., Gaillard, W. D., Golby, A. J., Holland, S. K., . . . Theodore, W. H. (2017). Practice guideline summary: Use of fMRI in the presurgical evaluation of patients with epilepsy. *Report of the Guideline Development, Dissemination, and Implementation Subcommittee of the American Academy of Neurology, 88*(4), 395-402. doi:10.1212/wnl.0000000000003532

Tancredi, F. B., & Hoge, R. D. (2013). Comparison of cerebral vascular reactivity measures obtained using breath-holding and CO2 inhalation. *J Cereb Blood Flow Metab, 33*(7), 1066-1074. doi:10.1038/jcbfm.2013.48

Taneja, K., Lu, H., Welch, B. G., Thomas, B. P., Pinho, M., Lin, D., . . . Liu, P. (2019). Evaluation of cerebrovascular reserve in patients with cerebrovascular diseases using resting-state MRI: A feasibility study. *Magnetic Resonance Imaging, 59*, 46-52. doi:https://doi.org/10.1016/j.mri.2019.03.003

Thomas, B. P., Liu, P., Park, D. C., van Osch, M. J. P., & Lu, H. (2014a). Cerebrovascular reactivity in the brain white matter: magnitude, temporal characteristics, and age effects. *Journal of Cerebral Blood Flow & Metabolism, 34*(2), 242-247. doi:10.1038/jcbfm.2013.194

Thomas, B. P., Liu, P., Park, D. C., van Osch, M. J. P., & Lu, H. (2014b). Cerebrovascular reactivity in the brain white matter: magnitude, temporal characteristics, and age effects. *Journal of cerebral blood flow and metabolism : official journal of the International Society of Cerebral Blood Flow and Metabolism, 34*(2), 242-247. doi:10.1038/jcbfm.2013.194

Thomason, M. E., Burrows, B. E., Gabrieli, J. D., & Glover, G. H. (2005). Breath holding reveals differences in fMRI BOLD signal in children and adults. *Neuroimage, 25*(3), 824-837. doi:10.1016/j.neuroimage.2004.12.026

Thomason, M. E., Foland, L. C., & Glover, G. H. (2007). Calibration of BOLD fMRI using breath holding reduces group variance during a cognitive task. *Hum Brain Mapp, 28*(1), 59-68.

Thomason ME, G. G. (2008). Controlled inspiration depth reduces variance in breath-holding-induced BOLD signal. . *Neuroimage, 39*, 206-214. doi:doi: 10.1016/j.neuroimage.2007.08.014

Tong, Y., Hocke, L. M., & Frederick, B. B. (2019). Low Frequency Systemic Hemodynamic "Noise" in Resting State BOLD fMRI: Characteristics, Causes, Implications, Mitigation Strategies, and Applications. *Front Neurosci, 13*(787). doi:10.3389/fnins.2019.00787

Tong, Y., Lindsey, K. P., Hocke, L. M., Vitaliano, G., Mintzopoulos, D., & Frederick, B. D. (2017). Perfusion information extracted from resting state functional magnetic resonance imaging. *J Cereb Blood Flow Metab, 37*(2), 564-576. doi:10.1177/0271678x16631755

Tsvetanov, K. A., Henson, R. N., Tyler, L. K., Davis, S. W., Shafto, M. A., Taylor, J. R., . . . Rowe, J. B. (2015). The effect of ageing on fMRI: Correction for the confounding effects of vascular reactivity evaluated by joint fMRI and MEG in 335 adults. *Hum Brain Mapp, 36*(6), 2248-2269. doi:10.1002/hbm.22768

Tsvetanov, K. A., Henson, R. N. A., Jones, P. S., Mutsaerts, H., Fuhrmann, D., Tyler, L. K., . . . Rowe, J. B. (2020). The effects of age on resting-state BOLD signal variability is explained by cardiovascular and cerebrovascular factors. *Psychophysiology, n/a*(n/a), e13714. doi:https://doi.org/10.1111/psyp.13714

Ulmer, J. L., Hacein-Bey, L., Mathews, V. P., Mueller, W. M., DeYoe, E. A., Prost, R. W., . . . Schmainda, K. M. (2004). Lesion-induced pseudo-dominance at functional magnetic resonance imaging: implications for preoperative assessments. *Neurosurgery, 55*(3), 569-579; discussion 580-561.

Ulmer, J. L., Krouwer, H. G., Mueller, W. M., Ugurel, M. S., Kocak, M., & Mark, L. P. (2003). Pseudo-reorganization of language cortical function at fMR imaging: a consequence of tumor-induced neurovascular uncoupling. *AJNR Am J Neuroradiol, 24*(2), 213-217.

Ulmer, J. L., Salvan, C. V., Mueller, W. M., Krouwer, H. G., Stroe, G. O., Aralasmak, A., & Prost, R. W. (2004). The role of diffusion tensor imaging in establishing the proximity of tumor borders to functional brain systems: implications for preoperative risk assessments and postoperative outcomes. *Technol Cancer Res Treat, 3*(6), 567-576.

Urback, A. L., MacIntosh, B. J., & Goldstein, B. I. (2017). Cerebrovascular reactivity measured by functional magnetic resonance imaging during breath-hold challenge: A systematic review. *Neuroscience & Biobehavioral Reviews, 79*(Supplement C), 27-47. doi:https://doi.org/10.1016/j.neubiorev.2017.05.003

Vakamudi, K., Posse, S., Jung, R., Cushnyr, B., & Chohan, M. O. (2020). Real-time presurgical resting-state fMRI in patients with brain tumors: Quality control and comparison with task-fMRI and intraoperative mapping. *Human Brain Mapping, 41*(3), 797-814. doi:https://doi.org/10.1002/hbm.24840

van Gelderen, P., de Zwart, J. A., & Duyn, J. H. (2008). Pittfalls of MRI measurement of white matter perfusion based on arterial spin labeling. *Magn Reson Med, 59*(4), 788-795. doi:10.1002/mrm.21515

van Niftrik, C. H. B., Piccirelli, M., Bozinov, O., Pangalu, A., Valavanis, A., Regli, L., & Fierstra, J. (2016). Fine tuning breath-hold-based cerebrovascular reactivity analysis models. *Brain and Behavior, 6*(2), e00426. doi:10.1002/brb3.426

van Niftrik, C. H. B., Piccirelli, M., Muscas, G., Sebok, M., Fisher, J. A., Bozinov, O., . . . Fierstra, J. (2019). The voxel-wise analysis of false negative fMRI activation in regions of provoked impaired cerebrovascular reactivity. *PLoS ONE, 14*(5), e0215294. doi:10.1371/journal.pone.0215294

Voss, H. U., Peck, K. K., Petrovich Brennan, N. M., Pogosbekyan, E. L., Zakharova, N. E., Batalov, A. I., . . . Holodny, A. I. (2019). A vascular-task response dependency and its application in functional imaging of brain tumors. *Journal of Neuroscience Methods, 322*, 10-22. doi:10.1016/j.jneumeth.2019.04.004

Vysotski, S., Madura, C., Swan, B., Holdsworth, R., Lin, Y., Munoz Del Rio, A., . . . Kuo, J. S. (2018). Preoperative FMRI associated with decreased mortality and morbidity in brain tumor patients. *Interdisciplinary Neurosurgery: Advanced Techniques and Case Management, 13*, 40-45. doi:10.1016/j.inat.2018.02.001

Watkins, S., Robel, S., Kimbrough, I. F., Robert, S. M., Ellis-Davies, G., & Sontheimer, H. (2014). Disruption of astrocyte-vascular coupling and the blood-brain barrier by invading glioma cells. *Nat Commun, 5*, 4196. doi:10.1038/ncomms5196

Wengenroth, M., Blatow, M., Guenther, J., Akbar, M., Tronnier, V. M., & Stippich, C. (2011). Diagnostic benefits of presurgical fMRI in patients with brain tumours in the primary sensorimotor cortex. *European radiology, 21*(7), 1517-1525. doi:10.1007/s00330-011-2067-9

White, L. E., Andrews, T. J., Hulette, C., Richards, A., Groelle, M., Paydarfar, J., & Purves, D. (1997). Structure of the human sensorimotor system. II: Lateral symmetry. *Cereb Cortex, 7*(1), 31-47. doi:10.1093/cercor/7.1.31

Wise, R. G., Ide, K., Poulin, M. J., & Tracey, I. (2004). Resting fluctuations in arterial carbon dioxide induce significant low frequency variations in BOLD signal. *Neuroimage, 21*(4), 1652-1664. doi:10.1016/j.neuroimage.2003.11.025

Wu, P., Bandettini, P. A., Harper, R. M., & Handwerker, D. A. (2015). Effects of Thoracic Pressure Changes on MRI Signals in the Brain. *Journal of Cerebral Blood Flow & Metabolism, 35*(6), 1024-1032. doi:10.1038/jcbfm.2015.20

Yang, H., Long, X.-Y., Yang, Y., Yan, H., Zhu, C.-Z., Zhou, X.-P., . . . Gong, Q.-Y. (2007). Amplitude of low frequency fluctuation within visual areas revealed by resting-state functional MRI. *Neuroimage, 36*(1), 144-152. doi:10.1016/j.neuroimage.2007.01.054

Yang, J., Gohel, S., Zhang, Z., Hatzoglou, V., Holodny, A. I., & Vachha, B. A. (2020). Glioma-Induced Disruption of Resting-State Functional Connectivity and Amplitude of Low-Frequency Fluctuations in the Salience Network. *American Journal of Neuroradiology*. doi:10.3174/ajnr.A6929

Zaca, D., Hua, J., & Pillai, J. J. (2011). Cerebrovascular reactivity mapping for brain tumor presurgical planning. *World J Clin Oncol, 2*(7), 289-298. doi:10.5306/wjco.v2.i7.289

Zaca, D., Jovicich, J., Nadar, S. R., Voyvodic, J. T., & Pillai, J. J. (2014). Cerebrovascular reactivity mapping in patients with low grade gliomas undergoing presurgical sensorimotor mapping with BOLD fMRI. *J Magn Reson Imaging, 40*(2), 383-390. doi:10.1002/jmri.24406

Zaca, D., & Pillai, J. J. (2012). *Cerebrovascular reactivity (CVR) mapping in patients with low grade gliomas undergoing presurgical mapping with BOLD fMRI*. Paper presented at the International Society for Magnetic Resonance in Medicine (ISMRM), Melbourne, Australia.

Zang, Y. F., He, Y., Zhu, C. Z., Cao, Q. J., Sui, M. Q., Liang, M., . . . Wang, Y. F. (2007). Altered baseline brain activity in children with ADHD revealed by resting-state functional MRI. *Brain Dev, 29*(2), 83-91. doi:10.1016/j.braindev.2006.07.002

Zhang, A. S., Ostrom, Q. T., Kruchko, C., Rogers, L., Peereboom, D. M., & Barnholtz-Sloan, J. S. (2017). Complete prevalence of malignant primary brain tumors registry data in the United States compared with other common cancers, 2010. *Neuro Oncol, 19*(5), 726-735. doi:10.1093/neuonc/now252

Zhang, Y., Brady, M., & Smith, S. (2001). Segmentation of brain MR images through a hidden Markov random field model and the expectation-maximization algorithm. *IEEE Trans Med Imaging, 20*(1), 45-57. doi:10.1109/42.906424

Zonta, M., Angulo, M. C., Gobbo, S., Rosengarten, B., Hossmann, K.-A., Pozzan, T., & Carmignoto, G. (2003). Neuron-to-astrocyte signaling is central to the dynamic control of brain microcirculation. *Nature Neuroscience, 6*(1), 43-50. doi:10.1038/nn980

VII. Appendices

Appendix A: Two by Two Contingency Tables

The figure below shows two-by-two contingency tables for (A): breath-hold or resting-state CVR vs. gray matter comparisons and (B): breath-hold vs. resting-state CVR comparisons. TP: true positive, TN: true negative, FP: false positive, FN: false negative. Colors in B correspond to voxel colors in Figure 2.3B.

A.

		Gray Matter	Non-gray Matter
CVR Metric	Present	**TP**	**FP**
	Absent	**FN**	**TN**

B.

		Breath-hold CVR	
		Present	Absent
Resting-state CVR	Present	TP	**FP**
	Absent	**FN**	TN

Appendix B: Cerebrovascular Reactivity Metric Self-Comparison Control

For 5 subjects, we compared two independent samples of breath-hold cerebrovascular reactivity (CVR) data to each other and did the same for two samples of resting-state CVR data. These data were subjected to the same predictive value analysis described in the main text. Supplemental Tables B1 and B2 provide an abbreviated listing of just the Accuracy and Dice coefficients for comparison with the results from the cross-metric analysis. For our sample of 5 subjects, the mean cross-metric correspondence accuracy was 71.4%.

Table B1. Voxel-Wise Correspondence of Two Independent Breath-hold CVR Patterns. Accuracy and Dice coefficient were computed using equations #3 and # 4.

Voxel-Wise Correspondence of Two Independent Breath-hold CVR Patterns

Subject	Acc	Dice
#1	65	66
#2	63	64
#3	61	61
#4	66	68
#5	63	64
Avg ± SD	**63.6 ± 1.9**	**64.6 ± 2.6**

Table B2. Voxel-Wise Correspondence of Two Independent Breath-hold CVR Patterns. Accuracy and Dice coefficient were computed using equations 1.3 and 1.4.

Voxel-Wise Correspondence of Two Independent Resting-state CVR Patterns

Subject	Acc	Dice
#1	89	90
#2	77	79
#3	80	86
#4	80	85
#5	76	76
Avg ± SD	**80.4 ± 5.1**	**83.2 ± 5.6**

Appendix C: Schematic of Methodology in Chapter II

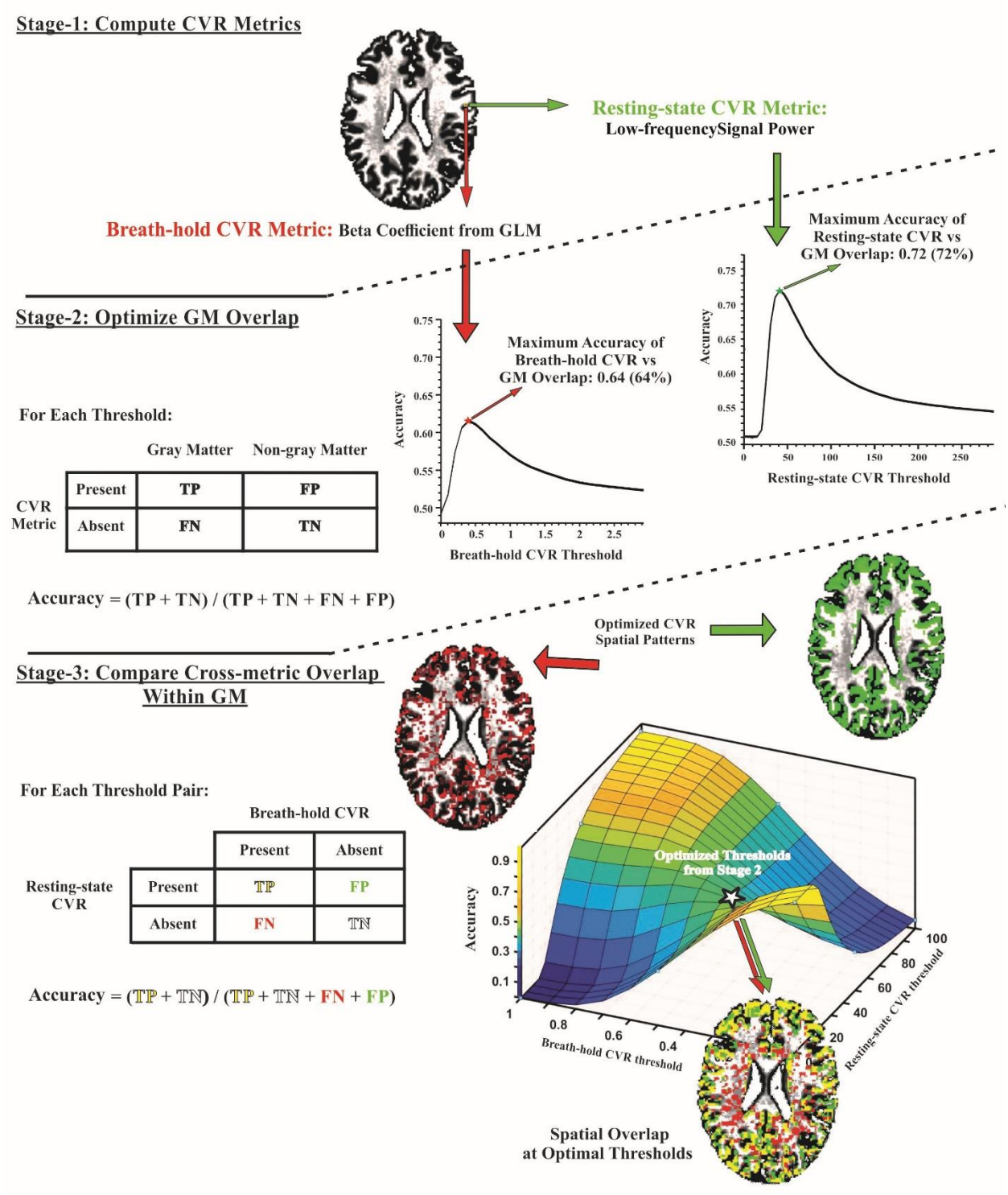

Figure C. Schematic of Methodology. CVR: cerebrovascular reactivity; **GM:** gray matter**; GLM:** general linear

model; **TP:** true positive; **TN:** true negative; **FP:** false positive; **FN:** false negative. Responsive voxels to the resting-state, the breath-hold, and both metrics are shown in green, red, and yellow, respectively.

VIII. CURRICULUM VITAE

Nooshin Jafari Fesharaki

Education and Qualification

- University of Wisconsin-Milwaukee, WI
  Ph.D. in Health Sciences (continued), Kinesiology Department 2017 – 2021
  Ph.D. in Health Sciences, Health Informatics and Administrations Department 2015 – 2016
  Dissertation" "Resting-state vs. Breath-hold for Testing FMRI Integrity in Pre-surgical Planning".

- Azad University, Iran 2009 – 2012
  M.Sc. in Electrical Engineering, Electrical Engineering Department
  Thesis: "Medical X-ray Image Classification Based on Content-based Feature Extraction and Selection".

- Azad University, Iran 2004 – 2008
  B.Sc. in Electrical Engineering, Electrical Engineering Department
  Thesis: "Optical Networks".

Experiences

Teaching Experiences:

- College of Health Sciences, UWM, WI – Teaching Assistant 2017 – 2019
  Graduate Instructor for the course "Statistics in the Health Sciences: Theory and Practice"

- Safahan Institute of Higher Education, Isfahan, Iran – Instructor 2011
  Designing and teaching the course "Introduction to Telecommunication Systems"

- International Nabius Spadana Institue, Isfahan, Iran – Instructor 2010
  Designing and teaching the course "Introduction to Telecommunication Systems"

Research Experiences:

- Center for Imaging Research, DeYoe Lab, MCW, WI – Research Technologist I/Volunteer Researcher 2017 – 2021
  Investigating the capability of CVR metrics to detect NVU-related false negatives in fMRI activation maps of patients with brain tumors.

- Cardiovascular Center, Gutterman Lab, MCW, WI – Research Technologist I 2016
  Organizing data from twenty years (1995 – 2016) of experimental studies on blood vessels into a comprehensive minable database.

- BioDLP Center, UWM, WI – Project Assistant/Volunteer Researcher 2016 – 2017

Developing a knowledge model from medical imaging notes using NLP and semantic network analysis techniques.

- College of Engineering and Applied Science, Ranji Lab, UWM, WI – Volunteer Researcher 2014 – 2015
  Investigating metabolic changes in animal models of ischemic injury and other lesions using fluorescence cryo-imaging and time-lapse fluorescence microscopy of live cells.

- College of Electrical Engineering, Azad University, Iran – Volunteer Researcher 2010 – 2012
  Using image processing approaches to classify medical images for developing CBIR systems.

- Ariya-Sepehre-Bahar Company, Isfahan, Iran – Internship 2008
  Designing electrical installations for residential and commercial buildings

University Services

- College of Health Sciences, UWM, WI – Coordinator for Big Data Workshop 2016

- Azad University, Iran – Volunteer Coordinator for Electrical Engineering National Conference 2007

Publications

Journals:

- **N. J. Fesharaki,** A. B. Mathew, J. Mathis, W. Huddleston, J. L. Reuss, J. J. Pillai, and E. A. DeYoe, "Effects of Thresholding on Voxel-wise Correspondence of Breath-hold and Resting-state Maps of Cerebrovascular Reactivity", J Frontiers in Neuroscience, 2021

- Y. Zhao, **N. J. Fesharaki**, H. Liu, and J. Luo, "Using data-driven sublanguage pattern mining to induce knowledge models: application in medical image reports knowledge representation", J BMC Medical Informatics and Decision Making, 2018; 18(1):61:1 – 61:13.

- Y. Zhao, **N. J. Fesharaki**, X. Li, T. B. Patrick, and J. Luo, "Semantic-enhanced query expansion system for retrieving medical image notes", J Medical Systems, 2018; 42(6): 105:1 – 105:11.

- **N. J. Fesharaki,** and H. Pourghassem, "Medical X-ray Image Classification Using a Merging and Splitting Scheme in Feature Space", J Medical Signals and Sensors, 2013; 3(3).

- **N. J. Fesharaki**, and H. Pourghassem, "Medical X-ray Image Clustering Using a New Gabor Function-based Image Representation", International Review on Computers and Software, 2012; 7(3)

Conference Papers and Posters:

- **N. J. Fesharaki,** W. Huddleston, J. L. Reuss, J. J. Pillai, and E. A. DeYoe, "Comparison of Low-frequency Resting-state fMRI and Breath-hold Metrics of Cerebrovascular Reactivity", Society for Neuroscience, 2019. **[Poster]**

- **N. J. Fesharaki,** W. Huddleston, and E. A. DeYoe, "A Comparison of Two fMRI-based Metrics of Cerebrovascular Reactivity", the UWM Health Research Symposium 2019. **[Poster]**

- **N. J. Fesharaki,** J. L. Reuss, J. J. Pillai, and E. A. DeYoe, "Quantitative Comparison of Breath-hold and Resting-state fMRI Metrics of Cerebrovascular Reactivity", American Society of Functional Neuroradiology, 2018. **[Oral Presentation]**

- Y. Zhao, **N. J. Fesharaki**, T. Patrick, and J. Luo, "Inducing a Knowledge Model from Medical Imaging Notes Using Network Analysis to Support Knowledge Representation", 2nd Annual Third Coast Biomedical and Health Informatics Consortium Conference, 2016**.**

- H. Pourghassem, **N. J. Fesharaki**, and A. Tahmasebi, "Material Detection Based on GMM-based Power Density Function Estimation and Fused Image in Dual-Energy X-ray Images", Proc. IEEE Conf. on Computational Intelligence and Communication Networks (CICN), 2012.

- **N. J. Fesharaki**, H. Pourghassem, "Medical X-ray Image Classification Based on Shape Features and Bayesian Rules", Proc IEEE Conf. on Computational Intelligence and Communication Networks (CICN), 2012. **[Oral Presentation]**

- **N. J. Fesharaki,** H. Pourghassem, and M. Noormohamadi, "Using Structural and Color Features of Streptomyces Clavuligerus Bacteria in Approximating of Production Level of Clavulanic Acid", Proc. IEEE Conf. ICCSN, 2011. **[Poster]**

- **N. J. Fesharaki,** H. Pourghassem, and M. Noormohamadi, "Production Estimate of Clavulanic Acid by Using Structural and Color Features", Proc of the 17th Iranian Conf. of Biomedical Engineering (ICBME), 2010. [**Poster**]